

Triaxial Weave Fabric Composites

A. Kueh and S. Pellegrino
CUED/D-STRUCT/TR223
Department of Engineering
University of Cambridge

European Space Agency Contractor Report

The work presented in this report was partially supported by an ESA contract.

Responsibility for its contents resides with the authors.

Technical monitor: Jo Wilson, RJTC.

Date: 30 June 2007.

Summary

This report investigates single-ply triaxial weave fabric (TWF) composites. It is shown that their behaviour differs in many important respects from standard laminated composites and hence appropriate models are required to predict their stiffness and strength. It is shown that the linear-elastic response of single-ply triaxial weave fabric composites can be accurately modelled in terms of a homogenized Kirchhoff plate. The ABD matrix for this plate is computed from an assembly of transversely isotropic three-dimensional beams whose unit cell is analysed using standard finite-element analysis, assuming periodic boundary conditions. It is also shown that the thermal deformation of TWF composites consists of two separate effects, namely a biaxial linear expansion which is characterized by the coefficient of linear expansion, plus the development of a thermally induced twist which is characterized by the coefficient of thermal twist. The value of these two coefficients is estimated with good accuracy by analytical and /or numerical models.

Contents

1	Introduction	1
1.1	Background	1
1.2	Present Approach	2
1.3	Layout of this Report	3
2	Materials, Production Methods, Tow Properties	5
2.1	Materials	5
2.2	Production	7
2.3	Cured Composite	9
2.4	Geometry of Tows	9
2.5	Thermo-Mechanical Properties of Tows	12
3	Derivation of Homogenized Elastic Properties from Finite Elements	15
3.1	Homogenized Plate Model	15
3.2	Unit Cell of TWF Composite	16
3.3	Periodic Boundary Conditions	17
3.4	Virtual Deformation Modes	20
3.5	PBC Setup in ABAQUS	20
3.6	Virtual Work Computation of ABD Matrix	22
4	Thermo-Mechanical Modelling	26
4.1	Background	26
4.2	Analytical Prediction of CTE	26
4.2.1	CTE Values	27
4.3	Finite Element Model	28
4.4	Thermo-Mechanical Behaviour	29
5	Test Methods	34
5.1	Measurement of Tension Properties	34
5.1.1	Coupons for Tension Tests	34
5.1.2	Apparatus	34
5.1.3	Testing Procedure	34
5.2	Measurement of Compression Properties	35

5.2.1	Coupons for Compression Tests	35
5.2.2	Apparatus	37
5.2.3	Testing Procedure	37
5.3	Measurement of in-plane Shear Properties	37
5.3.1	Photogrammetry Method	38
5.3.2	Clip Gauges Method	39
5.3.3	Coupons for in-plane Shear Tests	40
5.3.4	Specimen Preparation	41
5.3.5	Apparatus	42
5.3.6	Testing Procedure	42
5.3.7	Analysis of Measured Data	42
5.4	Measurement of Bending Properties	42
5.4.1	Bending Modulus Measurement	44
5.4.2	Coupons for Bending Modulus Tests	44
5.4.3	Apparatus	44
5.4.4	Testing Procedure	45
5.4.5	Analysis of Measured Data	45
5.5	Measurement of Failure Curvature	46
5.5.1	Coupons for Squash-Bend Tests	46
5.5.2	Apparatus	46
5.5.3	Testing Procedure	46
5.6	Measurement of Linear Coefficient of Thermal Expansion	47
5.6.1	Coupons for CTE Tests	47
5.6.2	Apparatus	48
5.6.3	Testing Procedure	48
5.7	Measurement of Thermal Twist	48
5.7.1	Coupons for Thermal Twist Tests	49
5.7.2	Apparatus	51
5.7.3	Testing Procedure	51
6	Test Results	52
6.1	Results of Tension Tests	52
6.2	Results of Compression Tests	53
6.3	Results of Shear Tests	56
6.4	Results of Bending Tests	56
6.4.1	Four-Point Bending Tests	56
6.4.2	Squashing Tests	59
6.5	Results of CTE Tests	60
6.6	Results of CTT Tests	61

7	Comparison of Experiments and Predictions	66
7.1	Stiffness Properties	66
7.1.1	Axial Stiffness	66
7.1.2	Shear Stiffness	67
7.1.3	Bending Stiffness	68
7.1.4	Alternative Estimates of ABD Matrix	68
7.2	Strength Properties	71
7.2.1	Tensile Strength	71
7.2.2	Compressive Strength	71
7.2.3	Shear Strength	72
7.2.4	Minimum Bend Radius	72
7.3	Thermo-Mechanical properties	72
7.3.1	CTE	72
7.3.2	CTT	73
8	Conclusion	77

Chapter 1

Introduction

1.1 Background

Triaxial weave fabric (TWF) composites are of interest for future lightweight structures, both rigid and deployable. The fabric is made up of continuous, interlaced strips of composite material with longitudinal fibres (tows) in three directions, at 0 degrees and ± 60 degrees; it is impregnated with resin and cured in an autoclave, like a standard composite. A particular attraction of this material is that it is mechanically quasi-isotropic, on a macroscopic scale, and hence can be used to construct single-ply structural elements of very low areal mass. Figure 1.1 shows a photograph of two spacecraft reflectors made from TWF. One can “see through” these structures, due to the high degree of porosity of the material.



Figure 1.1: Spring back reflectors (one folded and one deployed) on MSAT-2 spacecraft. Courtesy of Canadian Space Agency.

The behaviour of this material is more subtle than standard laminated composites, as in single-ply woven fabrics many of the three-dimensional degrees of freedom remain unconstrained.

This results in some important differences between the behaviour of single-ply TWF composites and standard composites, which include:

- Three-dimensional behaviour, leading to coupling between in-plane and out-of-plane effects; the outcome is that modelling TWF as a continuum gives poor results (Soykasap, 2006).
- Geometrically non-linear variation of in-plane stiffnesses, as the TWF becomes stiffer at larger strains, due to the straightening of the tows.
- Variation of the Poisson's ratio.
- Free edge effects, leading to reduced in-plane stiffness of strips of material that are not aligned with one of the tows. Edge effects are best described by the plot shown in Figure 1.2. These effects have been recently investigated (Aoki and Yoshida, 2006; Kueh,

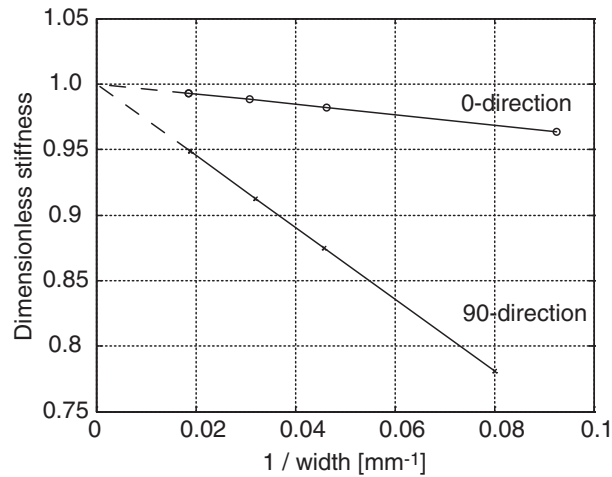


Figure 1.2: Ratio between in-plane axial stiffness of finite-sized and infinite TWF specimens.

Soykasap and Pellegrino, 2005; Kueh and Pellegrino, 2006) but there are still a number of open issues, both in terms of modelling techniques and the experimental verification of the numerical models.

- Thermally-induced twist.

1.2 Present Approach

A full characterization of TWF requires some key features of its three-dimensional microstructure to be considered but, as a fully-detailed analysis is impractical in engineering applications, it will be shown in this report that good predictions of stiffness can be made using a suitably defined, two-dimensional homogenized continuum.

The proposed approach is as follows.

- Measurement and analytical prediction of stiffness:

- At the macroscopic scale, TWF will be modelled by a homogenized continuum whose constitutive relationship is represented by a 6 by 6 ABD stiffness matrix. This matrix relates suitably defined in-plane and out-of-plane mean strains and curvatures to corresponding force and moment stress resultants per unit length.
 - Neglecting the geometric non-linearities mentioned above, the ABD matrix is constant.
 - We assume that, neglecting free edge effects, the behaviour of TWF is translationally symmetric in two perpendicular directions. Hence, we can assume that it is sufficient to analyse the deformation of a unit cell subject to periodic boundary conditions.
 - We derive the full ABD stiffness matrix from a finite-element analysis of a representative unit cell. Here each tow is modelled as a three-dimensional beam, whose geometry is obtained from direct measurement of the tows and whose material properties are based on the elastic properties of the fibres and the matrix, and their volume fractions.
 - The ABD matrix can be used to model the material for structural analysis; this leads to estimates of the generalized stresses and strains in the structure, which can be compared with experimentally obtained failure parameters.
- Experimental validation of a subset of the coefficients of the ABD matrix obtained from a finite-element analysis, against directly measured stiffness parameters.
 - Measurement and analytical prediction of failure parameters:
 - Maximum force per unit width, under in-plane compression.
 - Maximum force per unit width, under in-plane tension.
 - Maximum shear force per unit width.
 - Maximum bending moment per unit width and maximum curvature.
 - Measurement and analytical prediction of thermo-mechanical behaviour:
 - Linear coefficient of thermal expansion.
 - Coefficient of thermal twist.

1.3 Layout of this Report

This report is arranged as follows. In Chapter 2 we describe the particular carbon fibre TWF composite that we have studied and obtain estimates for the mechanical and thermo-mechanical properties of a single tow. In Chapter 3 we introduce a finite-element modelling technique to compute the ABD stiffness matrix of a homogenized plate model of TWF; we present in detail the implementation of the calculations with the finite-element package ABAQUS. In Chapter 4 we present a simple analytical model for the linear thermal expansion of TWF. We also introduce a detailed finite-element model to simulate the thermally induced deformation of TWF, which

captures the twisting induced by uniform temperature changes. Chapter 5 describes the test methods that were used to measure the behaviour of TWF composites. Seven different tests were carried out, several of which required novel specimen configurations or test layouts. The results of these tests are presented in Chapter 6. Chapter 7 presents comparisons between the experimental and analytical/computational predictions. Chapter 8 concludes the report.

Chapter 2

Materials, Production Methods, Tow Properties

2.1 Materials

The particular TWF composite that is studied in this report is based on the basic weave, shown in Figure 2.1. This is a very open and yet stable weave with fill yarns perpendicular to the direction of weaving plus warp yarns at $+60^\circ$ and -60° to the fill yarns. Figure 2.2 shows schematically a roll of this fabric, highlighting the directions of the weave.

The SK-802 carbon-fibre fabric produced by Sakase-Adtech Ltd., Japan, is used. The yarns of this fabric consist of 1000 filaments of T300 carbon fibre, produced by Toray Industries Inc., Japan. In the basic weave pattern the hexagonal holes cover about half of the area. SK-802 has a dry mass of 75 g/m^2 and a thickness of about 0.15 mm. The repeating unit cell of the fabric is defined in Figure 2.3. For the matrix, we use the space qualified resin Hexcel 8552, from Hexcel Composites, UK.

The properties of the two constituents, provided by the suppliers (Hexcel, 2007; Bowles, 1990; Toray, 2007), are listed in Table 2.1.

We define the volume fractions of fibres and resin in the composite *with respect to the total*

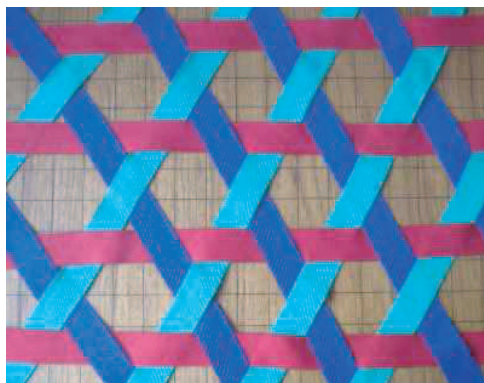


Figure 2.1: TWF basic weave.

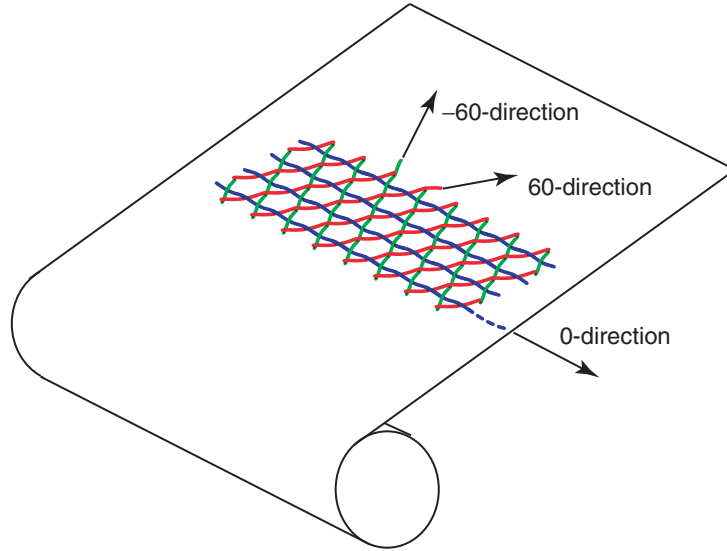


Figure 2.2: Schematic view of roll of dry fabric, showing the three directions of the weave.

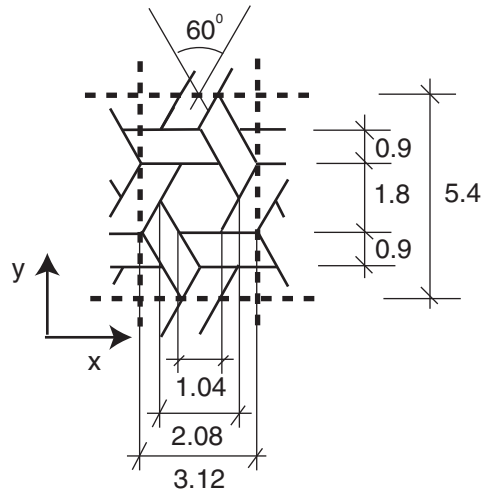


Figure 2.3: Dimensions of SK-802 fabric unit cell, in mm, and definition of coordinate system.

Table 2.1: Fibre and matrix properties

Properties	T300 fibre	Hexcel 8552 matrix
Density, ρ [kg/m ³]	1,760	1,301
Longitudinal stiffness, E_1 [N/mm ²]	233,000	4,670
Transverse stiffness, E_2 [N/mm ²]	23,100	4,670
Shear stiffness, G_{12} [N/mm ²]	8,963	1,704
Poisson's ratio, ν_{12}	0.2	0.37
Longitudinal CTE, α_1 [°C ⁻¹]	-0.54×10^{-6}	65.0×10^{-6}
Transverse CTE, α_2 [°C ⁻¹]	10.08×10^{-6}	65.0×10^{-6}
Maximum strain, ε_{max} [%]	1.5	1.7

volume of composite material, excluding the voids in the weave. In particular, the volume fraction of fibres, V_f , is defined as

$$V_f = \frac{\text{Vol. fibres}}{\text{Vol. fibres} + \text{Vol. matrix}} \quad (2.1)$$

which can be computed from

$$V_f = \frac{\rho_m W_f}{\rho_m W_f + \rho_f W_m} \quad (2.2)$$

where

- W_m = weight per unit area of resin film
- W_f = weight per unit area of dry fabric
- ρ_m = density of resin
- ρ_f = density of dry fibres

Then the volume fraction of matrix, V_m , can be computed from

$$V_m = 1 - V_f \quad (2.3)$$

2.2 Production

In the present work, we aim to achieve a fibre volume fraction of about 0.65, hence the required weight of resin per unit area is around 30 g/m².

We use the vacuum bagging method to lay-up the TWF composite before curing. The composite lay-up is shown in Figure 2.4. The lay-up and curing procedures are as follows:

1. “Iron-in” one layer of 30 g/m² film of Hexcel 8552 on one side of the dry fabric.
2. Lay the Tygafflor release fabric on top of a steel plate; the impregnated side being placed on the top.
3. Seal in a bag using Aerovac A500RP3 perforated release film, breather blanket and Capran bag, on the top, as shown in Figure 2.4.
4. Place the lay-up in an autoclave. Increase the temperature to 110°C, at a heating rate of 2°C/min, and pressurize to 6 bar. Hold the temperature for 1 hour.
5. Increase temperature to 180°C, at a heating rate of 2°C/min, and hold for 2 hours.
6. Depressurize and let the lay-up cool down. Ideally, the cooling rate should be 3 or 4°C/min.

Note that the two-step cure cycle described above differs from the standard cure cycle for Hexcel 8552 resin. In the standard cycle the lay-up is heated to 180°C and then cured, in a single step. The dwell at 110°C ensures that the resin has enough time to melt and seep through the fabric, before it begins to harden.

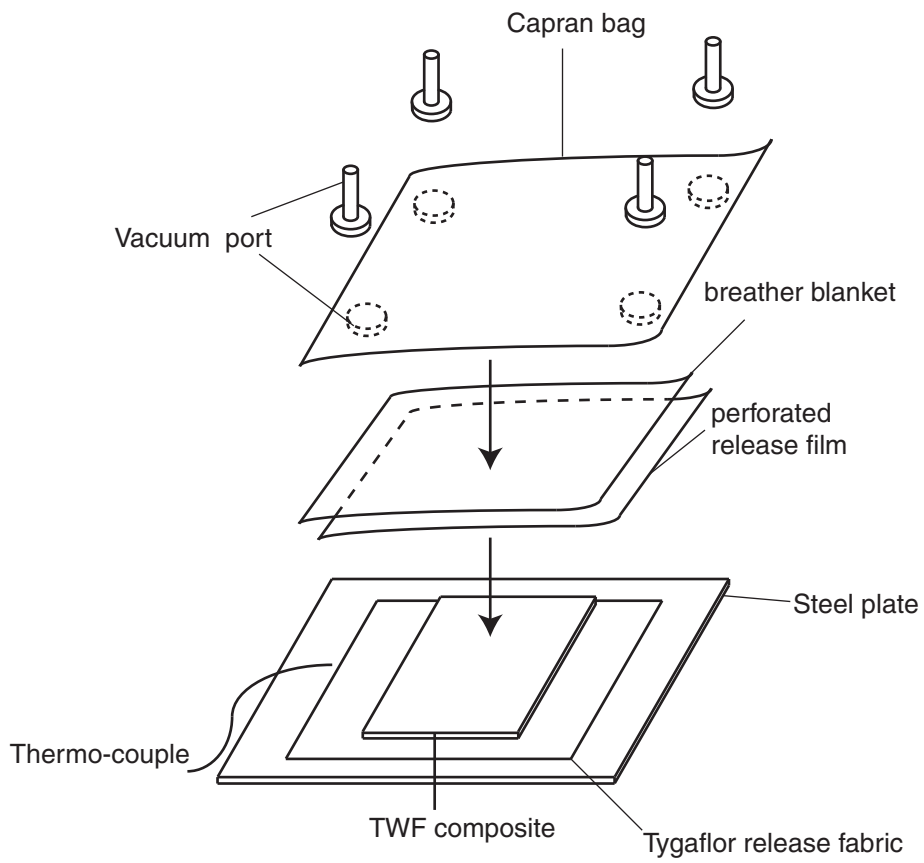


Figure 2.4: Lay-up for curing.

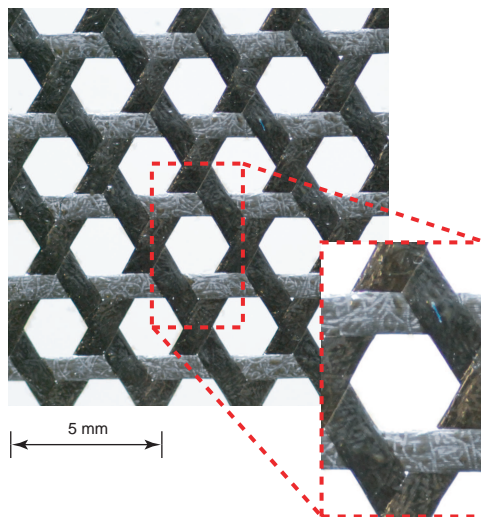


Figure 2.5: Small piece of single-ply TWF composite.

Table 2.2: Weight per unit area of cured samples (set 1)

specimen	W_c [g/m ²]
1	104.62
2	112.35
3	112.31
4	114.20
5	115.08
Average	111.71
Std. dev.	4.143
Variation [%]	3.71

2.3 Cured Composite

Figure 2.5 shows a photograph of the cured single-ply composite, and highlights the unit cell—now cured—defined before.

Five 50 mm × 50 mm pieces of single-ply TWF composite were weighed and their weights per unit area are listed in Table 2.2. The average value measured was $W'_c = 111.7$ g/m²; the corresponding average weight per unit area of the resin is

$$W'_m = W'_c - W_f = 111.7 - 75 = 36.7 \text{ g/m}^2 \quad (2.4)$$

Since this value is larger than the weight of resin film that had been used, five larger samples were weighed and a new set of weights per unit area were obtained. Their values are listed in Table 2.3. The average weight per unit area for the new set was $W''_c = 97.4$ g/m².

The overall average weight per unit area, considering both sets of samples, is $W_c = 104.5$ g/m², corresponding to a weight per unit area of resin of $W_m = 29.5$ g/m². This value is plausible as it is less than the weight of resin film used.

The fibre volume fraction for the tows is obtained by substituting W_r and the standard values of W_f, ρ_f, ρ_m into Equation 2.2. This gives

$$V_f = \frac{1301 \times 0.075}{1301 \times 0.075 + 1760 \times 0.0295} = 0.65 \quad (2.5)$$

2.4 Geometry of Tows

The micrograph in Figure 2.6 shows a section along the 0-direction tows. This section also cuts across two tows in the +60-direction (labelled as A and C) and one in the −60-direction (labelled B). Note that the sections of the tows are not perpendicular to their axes, and hence appear elongated by a factor of $1/\cos 30^\circ$. Also note that the top and bottom profiles of the tows sections are generally curved, apart from the profiles lying on the bottom edge of the sample, which is flat as it was pushed against a flat plate during the curing process.

Table 2.3: Weight per unit area of cured samples (set 2)

specimen	weight/area [g/m ²]
1	98.13
2	99.73
3	97.79
4	95.05
5	96.10
Average	97.36
Std. dev.	1.82
Variation [%]	1.87

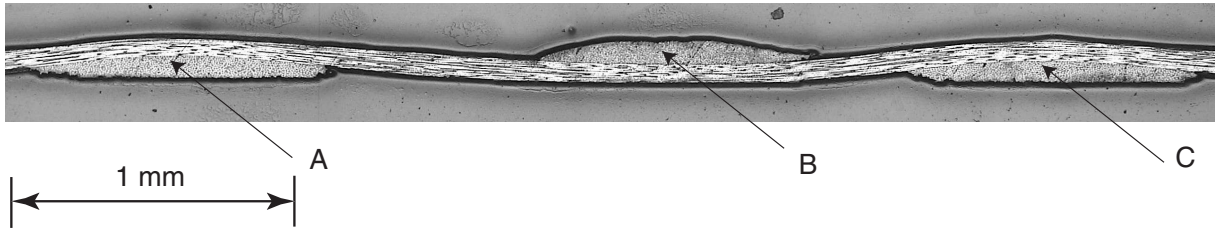


Figure 2.6: Micrograph showing a section through a piece of cured TWF composite.

To determine the cross sectional area of a tow, the outline of the tows in this and similar micrographs were traced using the package Illustrator (Adobe Systems, 2001). Each section trace was then converted into a region using Autocad (2002), and the enclosed area was then determined with Autocad, using the mass property function. This analysis was carried out on the sections of six different tows in the $\pm 60^\circ$ direction. Finally, the tows' cross sectional areas, A_t , were determined from

$$A_t = A \cos 30 \quad (2.6)$$

where A is the area computed with Autocad. Table 2.4 lists the cross sectional areas that were obtained in this way.

An alternative and more direct way of determining the cross sectional area of the tows is to sum the cross-sectional areas of the fibres and of the matrix in a tow. This is done as follows.

The total cross sectional area of the fibres within a tow, A_f , satisfies the following mass relationship

$$L\rho_f A_f = W_f A_{cell} \quad (2.7)$$

where

L = total length of tow centre line lying in the unit cell

A_{cell} = area of unit cell

Hence, solving for A_f

$$A_f = \frac{W_f A_{cell}}{L\rho_f} \quad (2.8)$$

Table 2.4: Tow cross-sectional areas

specimen	A_t [mm ²]
1	0.0612
2	0.0607
3	0.0618
4	0.0608
5	0.0670
6	0.0640
Average	0.0626
Std. dev.	0.002
Variation [%]	3.97

Substituting $A_{cell} = 0.0312 \times 0.054 \text{ mm}^2 = 16.86 \times 10^{-6} \text{ m}^2$, see Figure 2.3, and $L = 18.72 \times 10^{-3} \text{ m}$, which assumes the tow centre lines to be all coplanar, into Equation 2.8 gives

$$A_f = \frac{0.075 \times 16.86 \times 10^{-6}}{18.72 \times 10^{-3} \times 1760} = 3.839 \times 10^{-8} \text{ m}^2 = 3.839 \times 10^{-2} \text{ mm}^2 \quad (2.9)$$

The next step is to determine the cross sectional area of the matrix, A_r , embedding the fibres in a tow. Now, the key relationship is

$$L(\rho_f A_f + \rho_m A_m) = W_{com} A_{cell} \quad (2.10)$$

Solving for A_m and substituting all known terms

$$A_m = \frac{W_{com} A_{cell} / L - \rho_f A_f}{\rho_m} = \quad (2.11)$$

$$= \frac{\frac{104.53 \times 16.86 \times 10^{-9}}{18.72 \times 10^{-3}} - 1760 \times 3.839 \times 10^{-8}}{1301} = 2.041 \times 10^{-2} \text{ mm}^2 \quad (2.12)$$

Finally, we can compute the tow cross sectional area from

$$A_t = A_f + A_m = 5.88 \times 10^{-2} \text{ mm}^2 \quad (2.13)$$

which is 6% smaller than the average cross sectional area measured from the micrographs.

The thickness of the cured composite is defined as the *maximum thickness* that is measured from the micrographs. Six measurements were taken and their values are listed in Table 2.5. The average value is 0.156 mm.

In the analytical models presented in the next chapter the tows will be represented with beams of uniform rectangular cross section. The height of these rectangles will be set equal to half the measured thickness of the cured specimens; the width will be obtained from the condition that the rectangle should be equal to the cross-sectional area of the tow.

Therefore, the rectangle height is half the average thickness in Table 2.5, i.e. 0.078 mm. Taking the average tow area from Table 2.4, $A_t = 0.0626 \text{ mm}^2$, the rectangle width is 0.803 mm.

Table 2.5: Measured sample thickness

specimen	thickness [mm]
1	0.157
2	0.154
3	0.156
4	0.167
5	0.152
6	0.152
Average	0.156
Std. dev.	0.006
Variation [%]	3.59

2.5 Thermo-Mechanical Properties of Tows

In order to analyse the behaviour of a TWF composite we need to begin from the thermo-mechanical behaviour of the tows. Each tow is modelled as a three-dimensional continuum having transversely isotropic properties. The modulus in the fibre direction is higher than the two transverse directions, where the modulus is assumed to remain constant. The number of independent elastic constants needed to model a transversely isotropic solid is five (Daniel and Ishai, 2006): the longitudinal stiffness, E_1 , the transverse stiffness, E_2 , the longitudinal Poisson's ratio, ν_{12} , and the shear moduli, G_{12} and G_{23} . The thermal properties of the tow are also assumed to be transversely isotropic.

The independent engineering constants are determined as follows (Daniel and Ishai, 2006). The longitudinal extensional modulus, E_1 , is obtained from the rule of mixtures

$$E_1 = E_{1f}V_f + E_m(1 - V_f) \quad (2.14)$$

The Poisson's ratio is also found from the rule of mixtures

$$\nu_{12} = \nu_{13} = \nu_{12f}V_f + \nu_m(1 - V_f) \quad (2.15)$$

The transverse extensional modulus is found from the Halpin-Tsai semi-empirical relation

$$E_2 = E_3 = E_m \frac{1 + \xi\eta V_f}{1 - \eta V_f} \quad (2.16)$$

where

$$\eta = \frac{E_{2f} - E_m}{E_{2f} + \xi E_m} \quad (2.17)$$

and the parameter ξ is a measure of reinforcement of the composite that depends on the fibre geometry, packing geometry, and loading conditions. It has been set equal to 2.0 (Daniel and Ishai, 2006).

The shear modulus $G_{12} = G_{13}$ is found from the Halpin-Tsai semi-empirical relation (Daniel and Ishai, 2006)

$$G_{12} = G_{13} = G_m \frac{(G_{12f} + G_m) + V_f(G_{12f} - G_m)}{(G_{12f} + G_m) - V_f(G_{12f} - G_m)} \quad (2.18)$$

The in-plane shear modulus, G_{23} , is obtained by solving the following quadratic equation (Quek et al., 2003):

$$\left(\frac{G_{23}}{G_m}\right)^2 A + \left(\frac{G_{23}}{G_m}\right) B + C = 0 \quad (2.19)$$

where

$$\begin{aligned} A = & 3V_f(1 - V_f)^2 \left(\frac{G_{12f}}{G_m} - 1\right) \left(\frac{G_{12f}}{G_m} + \zeta_f\right) \\ & + \left[\left(\frac{G_{12f}}{G_m}\right) \zeta_m + \zeta_m \zeta_f - \left(\left(\frac{G_{12f}}{G_m}\right) \zeta_m - \zeta_f\right) (V_f)^3 \right] \\ & \times \left[\zeta_m V_f \left(\frac{G_{12f}}{G_m} - 1\right) - \left(\left(\frac{G_{12f}}{G_m}\right) \zeta_m + 1\right) \right] \end{aligned} \quad (2.20)$$

$$\begin{aligned} B = & -6V_f(1 - V_f)^2 \left(\frac{G_{12f}}{G_m} - 1\right) \left(\frac{G_{12f}}{G_m} + \zeta_f\right) \\ & + \left[\left(\frac{G_{12f}}{G_m}\right) \zeta_m + \left(\frac{G_{12f}}{G_m} - 1\right) V_f + 1 \right] \\ & \times \left[(\zeta_m - 1) \left(\frac{G_{12f}}{G_m} + \zeta_f\right) - 2(V_f)^3 \left(\left(\frac{G_{12f}}{G_m}\right) \zeta_m - \zeta_f\right) \right] \\ & + (\zeta_m + 1)V_f \left(\frac{G_{12f}}{G_m} - 1\right) \left[\frac{G_{12f}}{G_m} + \zeta_f + \left(\left(\frac{G_{12f}}{G_m}\right) \zeta_m - \zeta_f\right) (V_f)^3 \right] \end{aligned}$$

$$\begin{aligned} C = & 3V_f(1 - V_f)^2 \left(\frac{G_{12f}}{G_m} - 1\right) \left(\frac{G_{12f}}{G_m} + \zeta_f\right) \\ & + \left[\left(\frac{G_{12f}}{G_m}\right) \zeta_m + \left(\frac{G_{12f}}{G_m} - 1\right) V_f + 1 \right] \\ & \times \left[\frac{G_{12f}}{G_m} + \zeta_f + \left(\left(\frac{G_{12f}}{G_m}\right) \zeta_m - \zeta_f\right) (V_f)^3 \right] \end{aligned} \quad (2.21)$$

and

$$\zeta_m = 3 - 4\nu_m \quad (2.22)$$

$$\zeta_f = 3 - 4\nu_{12f} \quad (2.23)$$

Finally, ν_{23} is computed from

$$G_{23} = \frac{E_2}{2(1 + \nu_{23})} \quad (2.24)$$

The longitudinal thermal expansion coefficient is derived from Tsai and Hahn (1980)

$$\alpha_1 = \frac{E_{1f}\alpha_{1f}V_f + E_m\alpha_mV_m}{E_{1f}V_f + E_mV_m} \quad (2.25)$$

and the transverse thermal expansion coefficient from Tsai and Hahn (1980)

$$\alpha_2 = \alpha_3 = V_f\alpha_{2f} \left(1 + \nu_{12f}\frac{\alpha_{1f}}{\alpha_{2f}}\right) + V_m\alpha_m(1 + \nu_m) - (\nu_{12f}V_f + \nu_mV_m)\alpha_1 \quad (2.26)$$

Using the measured volume fraction, $V_f = 0.65$, the material properties of a tow made of T300/Hexcel 8552 have been computed using the equations presented above. The values obtained from these calculations are listed in Table 2.6.

Table 2.6: Tow material properties

Material Properties	Value
Longitudinal stiffness, E_1 [N/mm ²]	153,085
Transverse stiffness, $E_2 = E_3$ [N/mm ²]	12,873
Shear stiffness, $G_{12} = G_{13}$ [N/mm ²]	4,408
In-plane shear stiffness, G_{23} [N/mm ²]	4,384
Poisson's ratio, $\nu_{12} = \nu_{13}$	0.260
Longitudinal CTE, α_1 [/ ^o C]	0.16×10^{-6}
Transverse CTE, α_2 [/ ^o C]	37.61×10^{-6}

Chapter 3

Derivation of Homogenized Elastic Properties from Finite Elements

3.1 Homogenized Plate Model

An analytical model for the linear-elastic behaviour of single-ply TWF composites will be introduced. This model is set up by carrying out a detailed finite-element analysis of a repeating unit cell.

The kinematic description that is adopted is a standard, Kirchhoff thin plate, where the deformation of the plate is fully described by the deformation of its mid-surface. Hence the kinematic variables for the plate are the mid-plane strains

$$\varepsilon_x = \frac{\partial u}{\partial x} \quad (3.1)$$

$$\varepsilon_y = \frac{\partial v}{\partial y} \quad (3.2)$$

$$\varepsilon_{xy} = \frac{\partial u}{\partial y} + \frac{\partial v}{\partial x} \quad (3.3)$$

where it should be noted that the *engineering shear strain* is used, and the mid-plane curvatures

$$\kappa_x = -\frac{\partial^2 w}{\partial x^2} \quad (3.4)$$

$$\kappa_y = -\frac{\partial^2 w}{\partial y^2} \quad (3.5)$$

$$\kappa_{xy} = -2\frac{\partial^2 w}{\partial x \partial y} \quad (3.6)$$

where it should be noted that *twice the surface twist* is used. This is the standard variable used to define the twisting curvature in the theory of laminated plates (Daniel and Ishai, 2006).

The corresponding static variables are the mid-plane forces and moments per unit length N_x , N_y , N_{xy} and M_x , M_y , M_{xy} .

In analogy with classical composite laminate theory we write the 6×6 matrix relating these

two sets of variables as an ABD stiffness matrix, as follows:

$$\begin{pmatrix} N_x \\ N_y \\ N_{xy} \\ \text{---} \\ M_x \\ M_y \\ M_{xy} \end{pmatrix} = \begin{bmatrix} A_{11} & A_{12} & A_{16} & | & B_{11} & B_{12} & B_{16} \\ A_{21} & A_{22} & A_{26} & | & B_{21} & B_{22} & B_{26} \\ A_{61} & A_{62} & A_{66} & | & B_{61} & B_{62} & B_{66} \\ \text{---} & \text{---} & \text{---} & \text{---} & \text{---} & \text{---} & \text{---} \\ B_{11} & B_{21} & B_{61} & | & D_{11} & D_{12} & D_{16} \\ B_{12} & B_{22} & B_{62} & | & D_{21} & D_{22} & D_{26} \\ B_{16} & B_{26} & B_{66} & | & D_{61} & D_{62} & D_{66} \end{bmatrix} \begin{pmatrix} \varepsilon_x \\ \varepsilon_y \\ \varepsilon_{xy} \\ \text{---} \\ \kappa_x \\ \kappa_y \\ \kappa_{xy} \end{pmatrix} \quad (3.7)$$

where A_{ij} , B_{ij} , and D_{ij} represent the in-plane (*stretching* and *shearing*), coupling, and out-of-plane (*bending* and *twisting*) stiffness of the material, respectively.

This matrix is symmetric, and so the 3×3 submatrices A and D along the main diagonal are symmetric ($A_{ij} = A_{ji}$ and $D_{ij} = D_{ji}$), however (unlike the B matrix of a laminated plate) the B matrix is not guaranteed to be symmetric.

The inverse of the ABD stiffness matrix, which is useful when making comparison to measured stiffness values, is denoted as

$$\begin{pmatrix} \varepsilon_x \\ \varepsilon_y \\ \varepsilon_{xy} \\ \text{---} \\ \kappa_x \\ \kappa_y \\ \kappa_{xy} \end{pmatrix} = \begin{bmatrix} a_{11} & a_{12} & a_{16} & | & b_{11} & b_{12} & b_{16} \\ a_{21} & a_{22} & a_{26} & | & b_{21} & b_{22} & b_{26} \\ a_{61} & a_{62} & a_{66} & | & b_{61} & b_{62} & b_{66} \\ \text{---} & \text{---} & \text{---} & \text{---} & \text{---} & \text{---} & \text{---} \\ b_{11} & b_{21} & b_{61} & | & d_{11} & d_{12} & d_{16} \\ b_{12} & b_{22} & b_{62} & | & d_{21} & d_{22} & d_{26} \\ b_{16} & b_{26} & b_{66} & | & d_{61} & d_{62} & d_{66} \end{bmatrix} \begin{pmatrix} N_x \\ N_y \\ N_{xy} \\ \text{---} \\ M_x \\ M_y \\ M_{xy} \end{pmatrix} \quad (3.8)$$

3.2 Unit Cell of TWF Composite

The tows of TWF are modelled in ABAQUS (ABAQUS, 2001) using 3-node, quadratic beam elements (element B32). These elements are based on Timoshenko beam theory, which allows for transverse shear deformation. The beams are isotropic in the transverse direction; their properties are defined in Table 2.6.

The unit cell is shown in Figure 3.1. Note that the global z -axis is perpendicular to the mid plane of the unit cell. The edges of the unit cell are parallel to the axes and have dimensions (based on Figure 2.3) $\Delta l_x = 3.12$ mm and $\Delta l_y = 5.4$ mm.

The beam cross section is rectangular, with uniform width of 0.803 mm and uniform height of 0.078 mm, see Section 2.4. The centroidal axis of each beam undulates in the z -direction; the undulation has a piece-wise linear profile with amplitude Δl_z . This value is set equal to

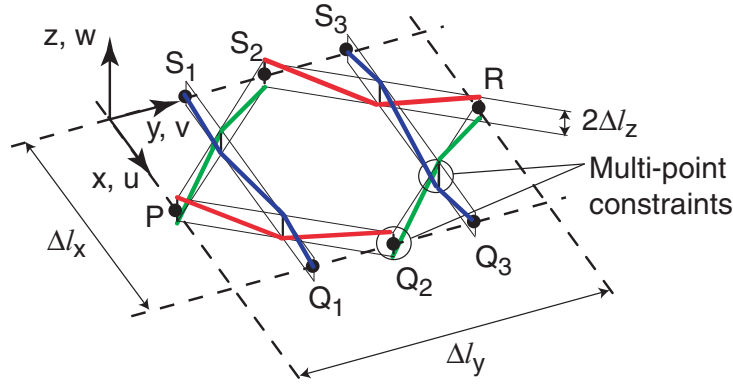


Figure 3.1: Perspective view of TWF unit cell.

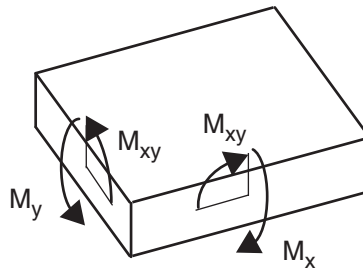


Figure 3.2: Moments sign convention for plate.

one quarter the thickness of the cured composite, see Section 2.4, and hence $\Delta l_z = 0.156/4 = 0.039$ mm.

At the cross-over points the beams are connected with rigid elements parallel to the z -direction. These connections are set up using multi-point constraints, in ABAQUS, i.e. with the command `*MPC` of type `*BEAM`. Note that the `*BEAM` constraint defines a rigid beam between the connected points, and so constrains both displacements and rotations at one node to those at the other node.

The whole TWF unit cell model consisted of 494 nodes and 248 elements.

3.3 Periodic Boundary Conditions

Periodic boundary conditions are a standard tool in the computation of homogenized models for composites and so there is an extensive literature on this topic. A recent paper by Tang and Whitcomb (2003) explains the key ideas involved in this approach, in the context of semi-analytical solutions based on assumed displacement fields within the unit cell. Of particular relevance to the present study is the direct micro-mechanics method introduced by Karkainen and Sankar (2006) for plain weave textile composites. The approach presented here is essentially that of this reference, but (i) extended to a triaxial weave and (ii) discretizing the TWF into a mesh of beam elements, instead of solid elements.

The idea is to assume that the average deformation of a TWF composite should match that

of a plate, over a length scale defined on the basis of the weave geometry. The stiffness properties of the homogenized plate are defined such that this match is achieved. More precisely, we will impose that any changes in deformation between corresponding points on opposite boundaries of the TWF unit cell match the deformation of the plate over the same length. These conditions of geometric compatibility are known as *periodic boundary conditions* (PBC), and will be imposed on the four pairs of nodes lying on the edges of the unit cell.

The more intuitive case is that of the mid-plane strains only, hence this case will be explained first. The in-plane stretching and shearing of the mid plane are described by the functions $u(x, y)$ and $v(x, y)$, where the origin of the coordinate system is in a corner of the unit cell, as shown in Figure 3.1. Expanding each of these functions into a Taylor series

$$u = u_0 + \left(\frac{\partial u}{\partial x}\right)_0 x + \left(\frac{\partial u}{\partial y}\right)_0 y \quad (3.9)$$

$$v = v_0 + \left(\frac{\partial v}{\partial x}\right)_0 x + \left(\frac{\partial v}{\partial y}\right)_0 y \quad (3.10)$$

where the subscript 0 denotes the origin of the coordinate system.

The derivatives $\partial u/\partial x$ and $\partial v/\partial y$ are equal to the normal strain components ε_x and ε_y , respectively, see Equations 3.1 and 3.2. Regarding the derivatives $\partial u/\partial y$ and $\partial v/\partial x$, we set each one equal to half the shear strain ε_{xy} , in order to satisfy Equation 3.3. Hence Equations 3.9-3.10 become

$$u = u_0 + \varepsilon_x x + \frac{1}{2}\varepsilon_{xy}y \quad (3.11)$$

$$v = v_0 + \frac{1}{2}\varepsilon_{xy}x + \varepsilon_y y \quad (3.12)$$

Consider a general pair of nodes lying on boundaries of the TWF unit cell. The change in in-plane displacement between these two nodes is set equal to the deformation of two corresponding points on the homogenized plate.

In the present case, because the boundaries are parallel to the x and y -directions, the pairs of nodes that we are interested in coupling have either the same x or the same y -coordinate and so the compatibility equations are specialised to

$$u^{Q_i} - u^{S_i} = \varepsilon_x \Delta l_x \quad (3.13)$$

$$v^{Q_i} - v^{S_i} = \frac{1}{2}\varepsilon_{xy}\Delta l_x \quad (3.14)$$

for $i = 1, 2, 3$ and

$$u^R - u^P = \frac{1}{2}\varepsilon_{xy}\Delta l_y \quad (3.15)$$

$$v^R - v^P = \varepsilon_y \Delta l_y \quad (3.16)$$

Next we will consider the effects of out-of-plane bending and twisting of the mid-plane. The (small) out-of-plane deflection of the mid-plane is described by the function $w(x, y)$. A Taylor series expansion, up to the second order, gives

$$w = w_0 + \left(\frac{\partial w}{\partial x}\right)_0 x + \left(\frac{\partial w}{\partial y}\right)_0 y + \frac{1}{2}\left(\frac{\partial^2 w}{\partial x^2}\right)_0 x^2 + \left(\frac{\partial^2 w}{\partial x \partial y}\right)_0 xy + \frac{1}{2}\left(\frac{\partial^2 w}{\partial y^2}\right)_0 y^2 \quad (3.17)$$

where the subscript 0 denotes the origin of the coordinate system.

Noting that the deflection at the origin, w_0 , can be made equal to zero by a rigid-body translation, defining the slopes at the origin, $\theta_{x0} = (\partial w / \partial y)_0$ and $\theta_{y0} = -(\partial w / \partial x)_0$, and substituting Equations 3.4-3.6, Equation 3.17 becomes

$$w = -\theta_{y0}x + \theta_{x0}y - \frac{1}{2}\kappa_x x^2 - \frac{1}{2}\kappa_{xy}xy - \frac{1}{2}\kappa_y y^2 \quad (3.18)$$

Hence, the slopes are

$$\theta_x = \frac{\partial w}{\partial y} = \theta_{x0} - \frac{1}{2}\kappa_{xy}x - \kappa_y y \quad (3.19)$$

$$\theta_y = -\frac{\partial w}{\partial x} = \theta_{y0} + \kappa_x x + \frac{1}{2}\kappa_{xy}y \quad (3.20)$$

We will now consider three separate deformation modes, pure bending—in both x and y directions—and pure twisting, as shown in Figure 3.3. The bending mode in the x -direction has $\kappa_x \neq 0, \kappa_y = 0, \kappa_{xy} = 0$; for simplicity the slope θ_{y0} is chosen such that $w = 0$ on two opposite edges, see Figure 3.3(a). Similarly, the bending mode in the y -direction has $\kappa_x = 0, \kappa_y \neq 0, \kappa_{xy} = 0$ and the slope θ_{x0} is chosen such that $w = 0$ on two opposite edges, see Figure 3.3(b).

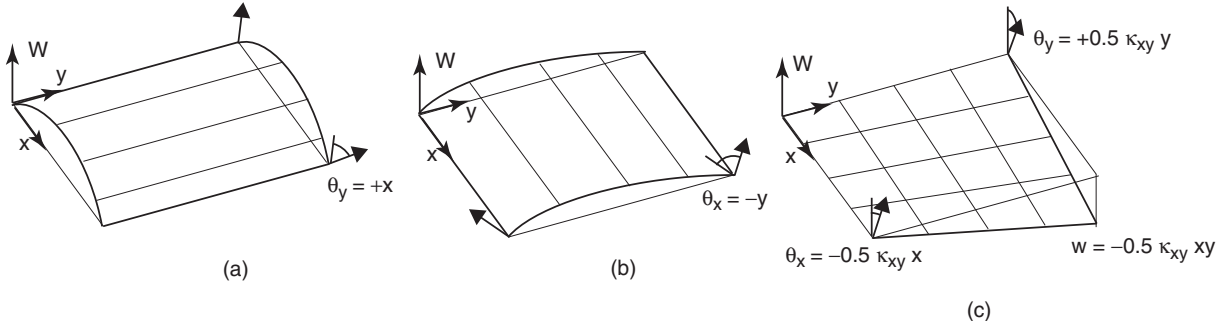


Figure 3.3: Three uniform deformation modes and associated rotations of normal vectors: (a) $\kappa_x = 1$; (b) $\kappa_y = 1$; (c) $\kappa_{xy} = 1$.

It is clear from the figure that the bending deformation modes do not result in a change in w for points on opposite boundaries, only the twisting mode does. It is also clear that bending in the x -direction will result in a rotation of the normal between points lying on boundaries parallel to the y -axis, but no rotation of the normal between points lying on boundaries parallel to the x -axis. Similarly, bending in the y -direction will result in a rotation of the normal between points lying on boundaries parallel to the x -axis, but no rotation of the normal between points lying on boundaries parallel to the y -axis. On the other hand, twisting will result in a rotation of the normal between any pair of points lying on opposite boundaries.

Therefore, the equation of compatibility between the change in out-of-plane displacement, Δw , between two corresponding points on opposite boundaries of the TWF composite and the deformation of a plate subject to uniform bending and twisting is

$$\Delta w = -\frac{1}{2}\kappa_{xy}\Delta x\Delta y \quad (3.21)$$

and the equations of compatibility for the rotation components are

$$\Delta\theta_x = -\kappa_y\Delta y - \frac{1}{2}\kappa_{xy}\Delta x \quad (3.22)$$

$$\Delta\theta_y = \kappa_x\Delta x + \frac{1}{2}\kappa_{xy}\Delta y \quad (3.23)$$

Substituting the coordinates of the relevant pairs of boundary nodes these equations can be specialised to

$$w^{Q_i} - w^{S_i} = -\frac{1}{2}\kappa_{xy}y_i\Delta l_x \quad (3.24)$$

$$w^R - w^P = -\frac{1}{2}\kappa_{xy}\frac{\Delta l_x}{2}\Delta l_y \quad (3.25)$$

and

$$\theta_x^{Q_i} - \theta_x^{S_i} = -\frac{1}{2}\kappa_{xy}\Delta l_x \quad (3.26)$$

$$\theta_y^{Q_i} - \theta_y^{S_i} = \kappa_x\Delta l_x \quad (3.27)$$

$$\theta_x^R - \theta_x^P = -\kappa_y\Delta l_y \quad (3.28)$$

$$\theta_y^R - \theta_y^P = \frac{1}{2}\kappa_{xy}\Delta l_y \quad (3.29)$$

In addition to the above conditions, we prevent all relative in-plane rotations between opposite nodes by setting

$$\theta_z^R - \theta_z^P = 0 \quad (3.30)$$

and

$$\theta_z^{Q_i} - \theta_z^{S_i} = 0 \quad (3.31)$$

for $i = 1, 2, 3$.

3.4 Virtual Deformation Modes

To derive the ABD matrix six unit deformations are imposed on the unit cell, in six separate ABAQUS analyses. In each case we set one average strain/curvature equal to one and all others equal to zero. For instance, in the first analysis, $\varepsilon_x = 1$ while $\varepsilon_y = \varepsilon_{xy} = 0$ and $\kappa_x = \kappa_y = \kappa_{xy} = 0$. In the five subsequent analyses ε_y , ε_{xy} , κ_x , κ_y , and κ_{xy} are set equal to 1, one at a time, while the other deformations are set equal to zero.

From each of the six analyses we obtain one set of deformations, including displacement and rotation components at the 8 boundary nodes, and one set of corresponding constraint forces and moments.

3.5 PBC Setup in ABAQUS

The ABAQUS commands for the definition of the periodic boundary conditions are *EQUATION and *BOUNDARY. For example, to write the command lines for Equation 3.13 for the node pair Q_iS_i , we begin by moving all terms to the left hand side. Now, we have

$$u^{Q_i} - u^{S_i} - \varepsilon_x\Delta l_x = 0 \quad (3.32)$$

The *EQUATION command for Equation 3.32 is written as follows

***EQUATION**

3

$Q_i, 1, 1, S_i, 1, -1, \text{TranQS}_i, 1, -\Delta l_x$

The first line contains the command *EQUATION. The second line contains the number 3, which indicates that there are three sets of terms in the equation (each set consists of *node, degree-of-freedom, coefficient*). The third line begins with the first node name, Q_i , followed by the number 1 designating the first degree of freedom of node Q_i , and followed by the number 1 representing the coefficient of u^{Q_i} in Equation 3.32. Next, we define the second node, S_i , followed by the number 1 indicating the first degree of freedom, and followed by the coefficient is -1 representing the coefficient of u^{S_i} in Equation 3.32. Finally we define the third node. This is a dummy node named TranQS_i representing the term ε_x in Equation 3.32. The number 1 designates the first component of the dummy node and the coefficient is $-\Delta l_x$, i.e. -3.12 .

Similarly, the command lines for Equation 3.14 are

***EQUATION**

3

$Q_i, 2, 1, S_i, 2, -1, \text{TranQS}_i, 2, -\Delta l_x$

These command lines are equivalent to those for Equation 3.13, with the main difference that the number 1, corresponding to the first degree of freedom, has been changed to 2. Note that the factor 0.5 in the coefficient of the shear strain does not appear in the set of terms defining the dummy node as it will be provided later on, in the *BOUNDARY command.

Next, the command lines for Equation 3.24 are

***EQUATION**

3

$Q_i, 3, 1, S_i, 3, -1, \text{TranQS}_i, 3, (\Delta l_x \times y_i)$

Here, the number 3 after each node name denotes the third degree of freedom. Also, the coefficient of the dummy node is now $(\Delta l_x \times y_i)$; for instance, for the node pair Q_1S_1 the coefficient is $3.12 \times 1.351 = 4.215$. Hence the command lines for this node pair are

***EQUATION**

3

$Q_1, 3, 1, S_1, 3, -1, \text{TranQS}_1, 3, 4.215$

For the rotation components of the node pair Q_iS_i the command lines corresponding to Equations 3.26, 3.27, and 3.31 are respectively

***EQUATION**

3

$Q_i, 4, 1, S_i, 4, -1, \text{RotQS}_i, 1, 3.12$

(here it should be noted that the factor 0.5 will be applied later on, using the *BOUNDARY command)

***EQUATION**

3

 $Q_i, 5, 1, S_i, 5, -1, \text{RotQS}_i, 2, -3.12$ ***EQUATION**

3

 $Q_i, 6, 1, S_i, 6, -1, \text{RotQS}_i, 3, 0$

where the numbers denoting the degrees of freedom are 4, 5, and 6, respectively, and the dummy nodes RotQS_i represent the curvature components.

To apply a deformation mode, we use the command ***BOUNDARY**. For instance, the command lines that impose the first deformation mode, $\varepsilon_x = 1$, are as follows

***BOUNDARY**TranQS₁, 1, 1, 1TranQS₁, 2, 3, 0TranQS₂, 1, 1, 1TranQS₂, 2, 3, 0TranQS₃, 1, 1, 1TranQS₃, 2, 3, 0RotQS₃, 1, 3, 0RotQS₃, 1, 3, 0RotQS₃, 1, 3, 0

TranRP, 1, 3, 0

RotRP, 1, 3, 0

These command lines apply a deformation of 1 to the first component of the dummy nodes TranQS₁, TranQS₂, and TranQS₃, while the remaining components for these nodes and all components of all other dummy nodes are set to 0.

All dummy nodes are defined in Table 3.1. Again, $i = 1, 2, 3$ identifies the three nodes on the longer boundary. The last column contains the constraint forces/couples corresponding to each component of each dummy node. These forces and couples are obtained by dividing each ABAQUS dummy node reaction component by the corresponding coefficient in the ***EQUATION** command line; the sign of this particular component is *positive* if the coefficients for the node and dummy node have *opposite sign*. F and C denote the constraint forces and couples, respectively. For example, $F_{Q_{xi}}$ is the constraint force at node Q_i , in the x -direction.

3.6 Virtual Work Computation of ABD Matrix

Six unit deformations are imposed on the unit cell, in six separate ABAQUS analyses; these will be referred to as Case A, ..., Case F. In each case we set one average strain/curvature equal to one and all others equal to zero. For instance, in the first analysis, $\varepsilon_{xx} = 1$ while $\varepsilon_{yy} = \varepsilon_{xy} = 0$ and $\kappa_{xx} = \kappa_{yy} = \kappa_{xy} = 0$. From each of the six analyses we obtain one set of deformations, including displacement and rotation components at the 8 boundary nodes, and

Table 3.1: Dummy variables

Node	Component	Variables	Constraint Force/Couple
TranQS _i	1	ε_x	F_{Qxi}, F_{Sxi}
	2	ε_{xy}	F_{Qyi}, F_{Syi}
	3	κ_{xy}	F_{Qzi}, F_{Szi}
TranRP	1	ε_{xy}	F_{Rx}, F_{Px}
	2	ε_{yy}	F_{Ry}, F_{Py}
	3	κ_{xy}	F_{Rz}, F_{Pz}
RotQS _i	1	κ_{xy}	C_{Qxi}, C_{Sxi}
	2	κ_x	C_{Qyi}, C_{Syi}
	3	$\Delta\theta_{zQSi}$	C_{Qzi}, C_{Szi}
RotRP	1	κ_y	C_{Rx}, C_{Px}
	2	κ_{xy}	C_{Ry}, C_{Py}
	3	$\Delta\theta_{zRP}$	C_{Rz}, C_{Pz}

one set of corresponding constraint forces and moments.

Next, we use virtual work to compute the entries of the ABD matrix. For example, entry 1,1 is obtained by writing the equation of virtual work for Case A (i.e. $\varepsilon_{xx} = 1$) and the forces/moments also in the first mode. Hence the equation reads

$$N_{xx}\varepsilon_{xx}\Delta l_x\Delta l_y = \sum_{b.n.} (F_x u + F_y v + F_z w + M_x \theta_x + M_y \theta_y + M_z \theta_z) \quad (3.33)$$

where the summation is extended to the 8 boundary nodes (b.n.). Then, substituting $\varepsilon_{xx} = 1$ and comparing with Equation 3.7 we obtain

$$A_{11} = \frac{\sum_{b.n.} (F_x u + F_y v + F_z w + M_x \theta_x + M_y \theta_y + M_z \theta_z)}{\Delta l_x \Delta l_y} \quad (3.34)$$

The calculation of the whole ABD matrix is best done by setting up two matrices with 48 rows (i.e. 6 degrees of freedom per node times 8 boundary nodes) and 6 columns (i.e. the six deformation modes).

The first matrix, U , contains in each column the displacement and rotation components at all boundary nodes for each particular case

$$U = \begin{bmatrix} u_{PA} & u_{PB} & u_{PC} & u_{PD} & u_{PE} & u_{PF} \\ v_{PA} & v_{PB} & v_{PC} & v_{PD} & v_{PE} & v_{PF} \\ w_{PA} & w_{PB} & w_{PC} & w_{PD} & w_{PE} & w_{PF} \\ \theta_{PxA} & \theta_{PxB} & \theta_{PxC} & \theta_{PxD} & \theta_{Px E} & \theta_{Px F} \\ \theta_{PyA} & \theta_{PyB} & \theta_{PyC} & \theta_{PyD} & \theta_{Py E} & \theta_{Py F} \\ \theta_{PzA} & \theta_{PzB} & \theta_{PzC} & \theta_{PzD} & \theta_{Pz E} & \theta_{Pz F} \\ u_{Q_1A} & u_{Q_1B} & u_{Q_1C} & u_{Q_1D} & u_{Q_1E} & u_{Q_1F} \\ \dots & \dots & \dots & \dots & \dots & \dots \\ \theta_{S_{3z}A} & \theta_{S_{3z}B} & \theta_{S_{3z}C} & \theta_{S_{3z}D} & \theta_{S_{3z}E} & \theta_{S_{3z}F} \end{bmatrix} \quad (3.35)$$

The second matrix, F , contains in each column the forces and couples at all boundary nodes for each particular deformation case

$$F = \begin{bmatrix} F_{PxA} & F_{PxB} & F_{PxC} & F_{PxD} & F_{PxE} & F_{PxF} \\ F_{PyA} & F_{PyB} & F_{PyC} & F_{PyD} & F_{PyE} & F_{PyF} \\ F_{PzA} & F_{PzB} & F_{PzC} & F_{PzD} & F_{PzE} & F_{PzF} \\ C_{PxA} & C_{PxB} & C_{PxC} & C_{PxD} & C_{PxE} & C_{PxF} \\ C_{PyA} & C_{PyB} & C_{PyC} & C_{PyD} & C_{PyE} & C_{PyF} \\ C_{PzA} & C_{PzB} & C_{PzC} & C_{PzD} & C_{PzE} & C_{PzF} \\ F_{Q_1xA} & F_{Q_1xB} & F_{Q_1xC} & F_{Q_1xD} & F_{Q_1xE} & F_{Q_1xF} \\ \dots & \dots & \dots & \dots & \dots & \dots \\ C_{S_3zA} & C_{S_3zB} & C_{S_3zC} & C_{S_3zD} & C_{S_3zE} & C_{S_3zF} \end{bmatrix} \quad (3.36)$$

Equation 3.34 can then be extended to the following expression for the ABD matrix

$$ABD = \frac{U^T F}{\Delta l_x \cdot \Delta l_y} \quad (3.37)$$

and, substituting the expressions for U and F given in Appendix 8, we obtain

$$\begin{Bmatrix} N_x \\ N_y \\ N_{xy} \\ M_x \\ M_y \\ M_{xy} \end{Bmatrix} = \begin{bmatrix} 3312 & 1991 & 0 & | & 0.00 & 0.00 & -0.62 \\ 1991 & 3312 & 0 & | & 0.00 & 0.00 & 0.62 \\ 0 & 0 & 660 & | & 0.62 & -0.62 & 0.00 \\ \hline 0.00 & 0.00 & 0.62 & | & 2.11 & 0.59 & 0.00 \\ 0.00 & 0.00 & -0.62 & | & 0.59 & 2.11 & 0.00 \\ -0.62 & 0.62 & 0.00 & | & 0.00 & 0.00 & 0.76 \end{bmatrix} \begin{Bmatrix} \varepsilon_x \\ \varepsilon_y \\ \varepsilon_{xy} \\ \kappa_x \\ \kappa_y \\ \kappa_{xy} \end{Bmatrix} \quad (3.38)$$

where the units are N and mm.

This matrix has a number of symmetry properties. First the matrix itself is symmetrical. Second, the sub-matrices A and D are both symmetric. Third, B is antisymmetric (unlike the B matrix for a laminated plate).

Aoki and Yoshida (2006) have explained this result by noting that, because TWF composites are quasi-isotropic, both the A and D matrices have to satisfy the conditions met by an isotropic plate, namely $A_{11} = A_{22}$, $A_{66} = (A_{11} - A_{12})/2$ and $D_{11} = D_{22}$, $D_{66} = (D_{11} - D_{12})/2$. In more detail

$$\begin{bmatrix} a & b & 0 \\ b & a & 0 \\ 0 & 0 & \frac{a-b}{2} \end{bmatrix} \quad (3.39)$$

and

$$\begin{bmatrix} c & d & 0 \\ d & c & 0 \\ 0 & 0 & \frac{c-d}{2} \end{bmatrix} \quad (3.40)$$

Both of these properties are satisfied by the ABD matrix in Equation 3.38.

The inverse of the ABD matrix in Equation 3.38 is

$$\begin{Bmatrix} \varepsilon_x \\ \varepsilon_y \\ \varepsilon_{xy} \\ \kappa_x \\ \kappa_y \\ \kappa_{xy} \end{Bmatrix} = 10^{-6} \times \left[\begin{array}{ccc|ccc} 473 & -284 & 0 & 0 & 0 & 614 \\ -284 & 473 & 0 & 0 & 0 & -614 \\ 0 & 0 & 1515 & -614 & 614 & 0 \\ \hline 0 & 0 & -614 & 514086 & -143070 & 0 \\ 0 & 0 & 614 & -143070 & 514086 & 0 \\ 614 & -614 & 0 & 0 & 0 & 1314268 \end{array} \right] \begin{Bmatrix} N_x \\ N_y \\ N_{xy} \\ M_x \\ M_y \\ M_{xy} \end{Bmatrix} \quad (3.41)$$

Chapter 4

Thermo-Mechanical Modelling

4.1 Background

Single-ply TWF composites show counterintuitive behaviour when subjected to even the simplest kind of thermal loading. A first, purely numerical study was carried out by Zhao and Hoa (Zhao and Hoa, 2003), who observed that rectangular panels including different numbers of unit cells deform in bending and twisting by different amounts. No fully general relationship could be found, and no experimental validation of the results was obtained, but these authors proposed a series of approximate formulas for estimating average mid-plane thermal strains and curvatures.

Kueh and Pellegrino (2006) carried out a set of experiments and finite-element simulations aimed at establishing the key effects that had resulted in the complex behaviour reported by Zhao and Hoa. Tests on rectangular single-ply TWF panels hanging from a wire attached to a single point of the panel showed the panel bending into a cylindrical shape when its temperature was raised. It was conjectured that twisting had been prevented by geometrically non-linear effects and, to minimise this constraint, tests were conducted on narrow specimens, and thermally induced twisting was observed on these specimens. Time-dependent behaviour was also observed in these tests which resulted, prior to the present study, in additional work on resin selection, the curing process and moisture content of the specimen. As a result of this additional work, it is now believed that the time-dependent effects reported by Kueh and Pellegrino (2006) can be avoided by the use of a more stable resin system and by ensuring that it is fully cured.

A separate strand in Kueh and Pellegrino (2006) was a series of detailed finite-element simulations that linked the observed, thermally-induced twist to the out-of-plane deformation that develops at the interface between tows in different directions that are bonded in the cross-over region. This approach will be adopted and further developed, in the present chapter.

4.2 Analytical Prediction of CTE

This section presents a simple analytical model to predict the linear CTE of single-ply TWF composites. The idea is that the (small) CTE in the direction of a tow is increased by the (much larger) CTE of the tows bonded above and below this tow; of course, the longitudinal and transverse stiffness of these transverse tows needs to be included in the analysis.

Consider a straight tow with longitudinal CTE α_1 and stiffness $(EA)_1$, perfectly bonded to a series of tows that are perpendicular to it. Only those sections of these perpendicular tows that overlap the first tow will be considered; the rest of the material is neglected. Their CTE in the direction of the first tow is α_2 and their stiffness is $(EA)_2$. Poisson's ratio effects will be neglected.

It is assumed that bending effects, resulting from the eccentricity between the axis of the main tow and the perpendicular ones, can be neglected and so that the problem can be formulated in one dimension, as shown in Figure 4.1.

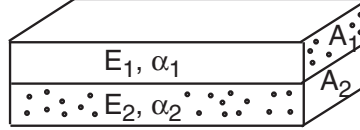


Figure 4.1: Schematic diagram of two-tow system for CTE analysis.

We are interested in the overall CTE of this two-tow system. Clearly, there will be a thermal strain mismatch when the system is subject to a uniform change of temperature, ΔT , resulting in equal and opposite axial forces, x , acting on the two separate tows. The resulting strains are

$$\varepsilon_1 = \alpha_1 \Delta T + \frac{x}{(EA)_1} \quad (4.1)$$

$$\varepsilon_2 = \alpha_2 \Delta T - \frac{x}{(EA)_2} \quad (4.2)$$

Setting $\varepsilon_1 = \varepsilon_2$ for compatibility and solving for x we obtain

$$x = (\alpha_2 - \alpha_1) \frac{(EA)_1 (EA)_2}{(EA)_1 + (EA)_2} \Delta T \quad (4.3)$$

and, substituting into Equation 4.1,

$$\varepsilon_1 = \left[\alpha_1 + \frac{(EA)_2 (\alpha_2 - \alpha_1)}{(EA)_1 + (EA)_2} \right] \Delta T \quad (4.4)$$

Dividing by ΔT we obtain the following expression for the CTE of the two-tow system

$$\alpha_c = \left[\alpha_1 + \frac{(EA)_2 (\alpha_2 - \alpha_1)}{(EA)_1 + (EA)_2} \right] \quad (4.5)$$

4.2.1 CTE Values

There are a number of effects that are not captured by this simple model; hence it would be rather pointless to trying to estimate its parameters with great accuracy. For example, what value of the CTE should be used for the cross tows, given that they are at $\pm 60^\circ$ and not at right angles? For simplicity we will assume that the effects of the change of angle are small and that the cross-sectional areas are equal, $A_1 = A_2$. Substituting the values in Table 2.6 into Equation 4.5 gives

$$\alpha_c = \left[0.16 + \frac{12,873(37.61 - 0.16)}{153,085 + 12,873} \right] \times 10^{-6} = 3.06 \times 10^{-6} \text{ } ^\circ\text{C}^{-1} \quad (4.6)$$

Then, assuming that only two-thirds of the main tow are covered by the cross tows the effective value of the CTE will be the average of α_1 and $2\alpha_c/3$. This gives

$$\bar{\alpha}_c = (0.16 + \frac{2}{3}3.06) \times 10^{-6} = 2.20 \times 10^{-6} \text{ }^\circ\text{C}^{-1} \quad (4.7)$$

4.3 Finite Element Model

We use solid-element models to simulate the thermo-mechanical behaviour of single-ply TWF composites, in order to capture the three-dimensional deformation of the tow cross-over regions. The model of the unit cell is shown in Figure 4.2. We model a single tow as a 3D continuum with the properties defined in Table 2.6. The thermo-mechanical properties of each tow are assumed to be transversely isotropic.

The unit cell comprises 2760 nodes and 2048 elements. The tows are modelled as having a uniform, rectangular cross-section, 0.803 mm wide and 0.078 mm high, with four elements through the thickness. The tow undulation is modelled in a piece-wise linear fashion; the tows cross-over regions are modelled as flat rhombuses, where it is assumed that the tows are fully joined together, connected by sloping regions that are straight in the longitudinal direction of the tow. Thus, the surface of each tow is continuous, but with localised slope changes when the tow meets a crossing tow. At this point there is a step change of thickness of the model.

Note that the presence of these step changes in the thickness of the model results in the important feature that each hexagon has six-fold rotational symmetry about an axis perpendicular to the mid plane of the unit and each triangle has three-fold rotational symmetry, however *the model is not symmetric about the mid-plane*.

An equal sided triangular gap with a 0.169 mm side length has been introduced, circled in Figure 4.2, to allow space for tow crossing.

A local Cartesian coordinate system is created for each piece of tow and the material properties of the tow are defined according to this local coordinate system. The coordinate system for a flat piece of tow has its 1-axis aligned with the fibre direction. The coordinate system for a sloping piece, joining two flat pieces, is such that the 3-axis is perpendicular to the surface of the sloping piece. The 1-axis is defined by joining corresponding points on the end cross-sections of the flat pieces. The material properties for the solid elements are defined based on this local coordinate system. We align the 1-axis to the direction of the fibres. After determining the local coordinate systems for a number of elements, due to symmetry, the remaining elements are defined, including their own coordinate systems, using the copy function and by rotation about the central point of the unit cell. The material properties of each element are then set equal to the values defined in Table 2.6.

An 8-node linear brick element with incompatible modes, C3D8I, is used to model the prismatic regions of the tows. The triangular regions are meshed with 6-node linear triangular prisms, C3D6. It has been found that the incompatible modes included in the formulation of this element lead to better performance in bending, and hence a lower mesh density is needed to achieve convergence compared to a standard 8-node linear brick element.

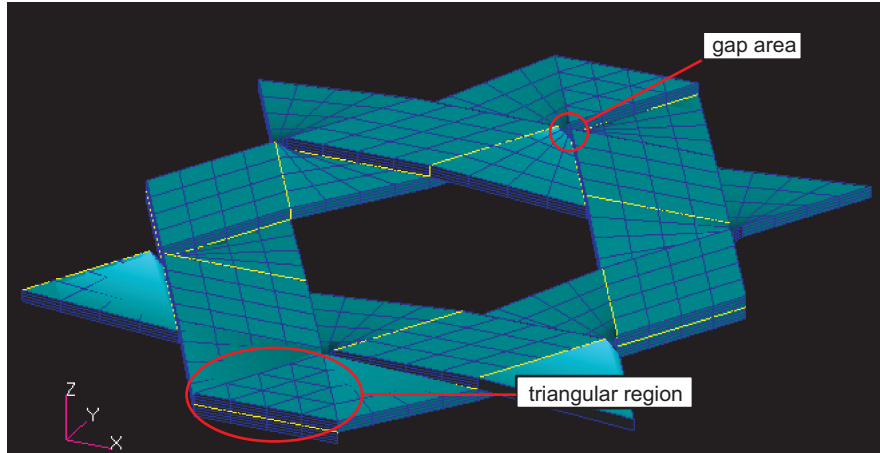


Figure 4.2: Solid element model of TWF unit cell.

4.4 Thermo-Mechanical Behaviour

Insight into the deformation of the tow contact region can be obtained by analysing the response to a uniform temperature increase of a simple model, consisting of two straight tows at right angles that are fully bonded across a square contact region, see Figure 4.3(a).

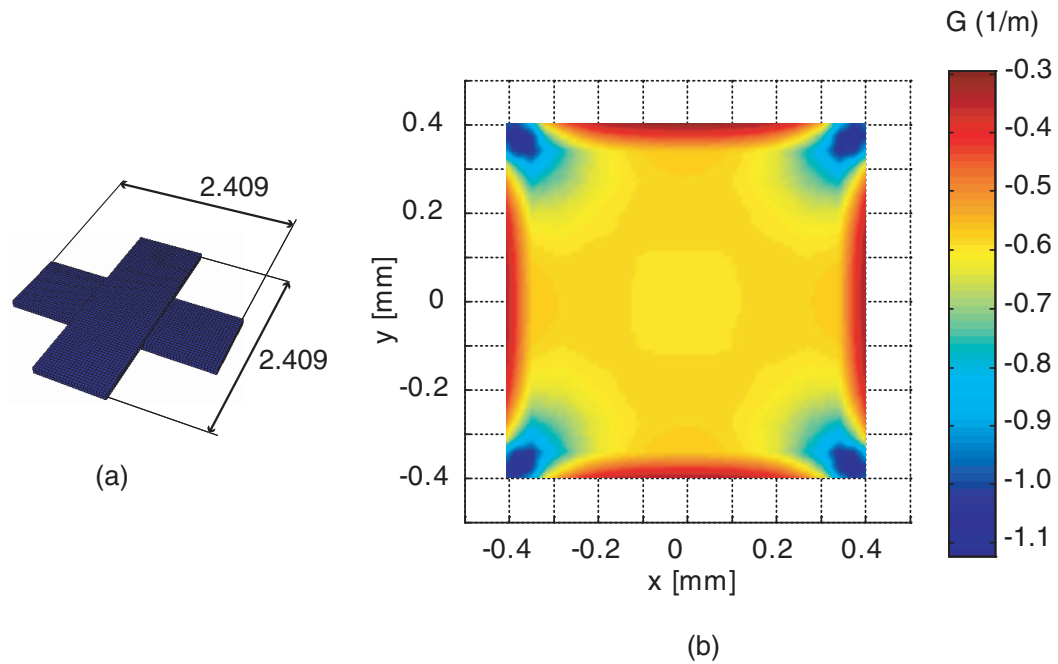


Figure 4.3: (a) Two-tow model (b) gaussian curvature of tow interface due to $\Delta T = 100^\circ\text{C}$.

This model shows that the initially flat region deforms into a saddle shape, as the gaussian curvature G is negative everywhere. The curvature is almost uniform across the interface, decreases near the edges of this region, and increases near the corners (where significant stress concentrations will occur). An important effect is that the deformation of the interface regions

forces the tows to become transversally curved.

Next, we consider two models that capture the twisting mode of deformation in TWF. Basically, a thermally-induced twist pattern develops in each of the triangular and hexagonal cells that make up the TWF, and we can see twist developing in either type of cell when a uniform temperature rise is applied. The deformations of the different cells are not fully compatible, however, and hence a state of self-stress develops in the interconnected structure. Therefore, the twist of the interconnected structure is smaller than that seen in the individual cells.

Figure 4.4 shows the two types of cells that will be analysed, with the boundary conditions used. Figure 4.5 shows contours of the deflection components in the direction perpendicular to the mid-plane of the TWF. Note that in Figure 4.5(a) the corners of each triangle move alternately one up and one down when the central node is held fixed. Also note that the edge of the hexagon deforms into an up-and-down mode. Both of these deformation patterns can be explained in terms of the basic deformation mode of the square cross, discussed above.

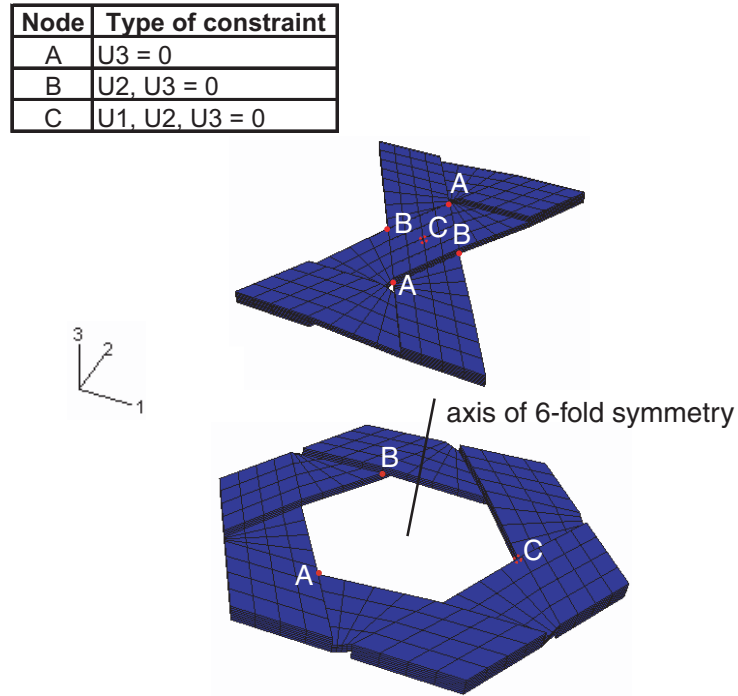


Figure 4.4: (i) Two triangular cells (ii) hexagonal cell.

A simple estimate of the twisting curvature can be made from these results, as follows. Consider in Figure 4.5(a) the out-of-plane displacement $\Delta w = 1.683 \times 10^{-2}$ mm of point P with respect to point O. The components of the distance PO are $\Delta x = 1.04$ mm and $\Delta y = 1.8$ mm. Hence the twist per unit temperature change can be calculated as

$$\frac{\kappa_{xy}}{\Delta T} \approx -2 \frac{\Delta w}{\Delta x \Delta y} \frac{1}{\Delta T} = -2 \frac{1.683 \times 10^{-2}}{1.04 \times 1.8} \frac{1}{100} = -1.80 \times 10^{-4} \text{ mm}^{-1} \text{ } ^\circ\text{C}^{-1} \quad (4.8)$$

A similar calculation can be used to estimate the twisting curvature of the hexagonal cell. Considering the points P and O marked in the figure, we have $\Delta w = 3.545 \times 10^{-3}$ mm, $\Delta x =$

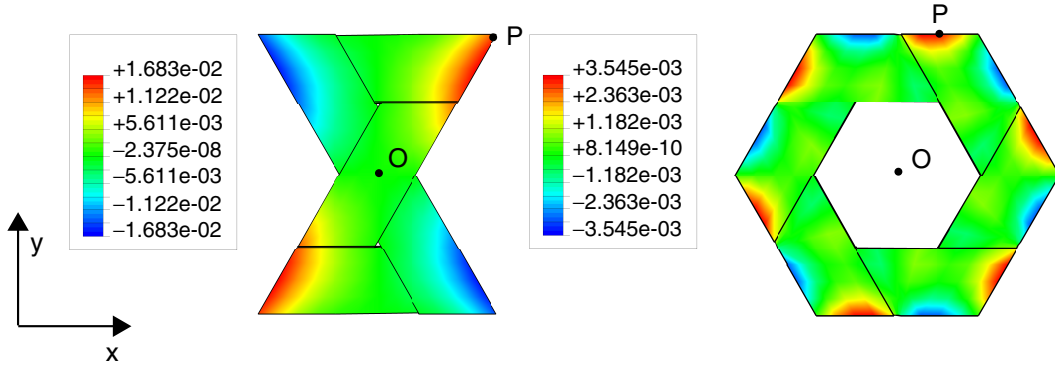


Figure 4.5: z -components of deflection, in mm, due to $\Delta T = 100^\circ\text{C}$.

0.58 mm and $\Delta y = 2.7$ mm. Hence the twist per unit temperature change can be calculated as

$$\frac{\kappa_{xy}}{\Delta T} \approx -2 \frac{\Delta w}{\Delta x \Delta y} \frac{1}{\Delta T} = -2 \frac{3.545 \times 10^{-3}}{0.58 \times 2.7} \frac{1}{100} = -4.53 \times 10^{-5} \text{ mm}^{-1} \text{ }^\circ\text{C}^{-1} \quad (4.9)$$

Figure 4.6 shows two one unit-wide strips of TWF composite. These two strips are obtained by cutting the TWF in (i) the direction of the 0-direction tows and (ii) in the direction perpendicular to the 0-direction tows.

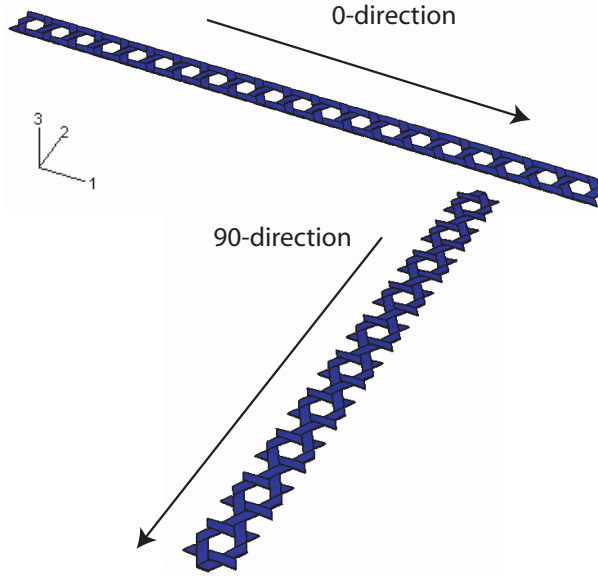


Figure 4.6: TWF strips in 0-direction and 90-direction.

We have analysed the behaviour of these two types of TWF strips when they are subjected to two different thermal loading cases. In the first case a uniform temperature increase of 100°C is applied; in the second case a thermal gradient of $\pm 2^\circ\text{C}$ is applied, in three uniform steps; the temperatures of the outer one-thirds of the thickness of the structure are subjected to $+2^\circ\text{C}$ and -2°C and the temperature of the central third is 0°C . The mechanical boundary conditions

are fully clamped at the left-hand side end of the strip. A linear elastic analysis is performed in all cases.

Figures 4.7 and 4.8 show that both strips bend when they are subjected to a thermal gradient, which is a standard result, however they twist when they are subject to a uniform temperature change. Note that the angle of twist is more than double in the case of the 90-direction strip.

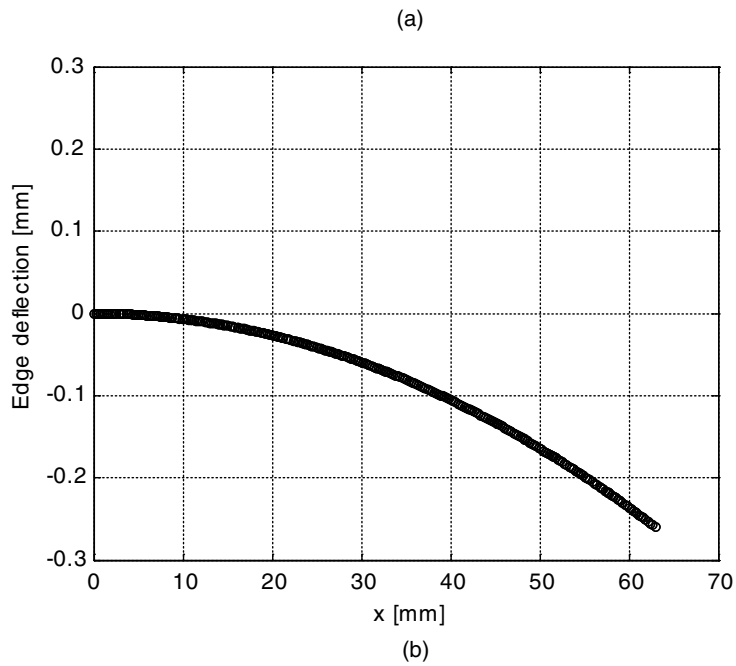
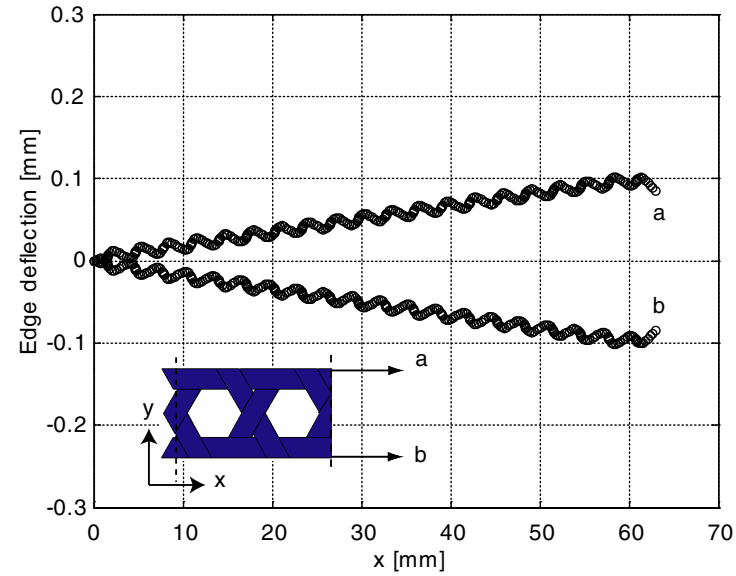


Figure 4.7: Deformation of 0-direction strip subject to (a) uniform temperature rise of 100°C and (b) thermal gradient of $\pm 2^\circ\text{C}$.

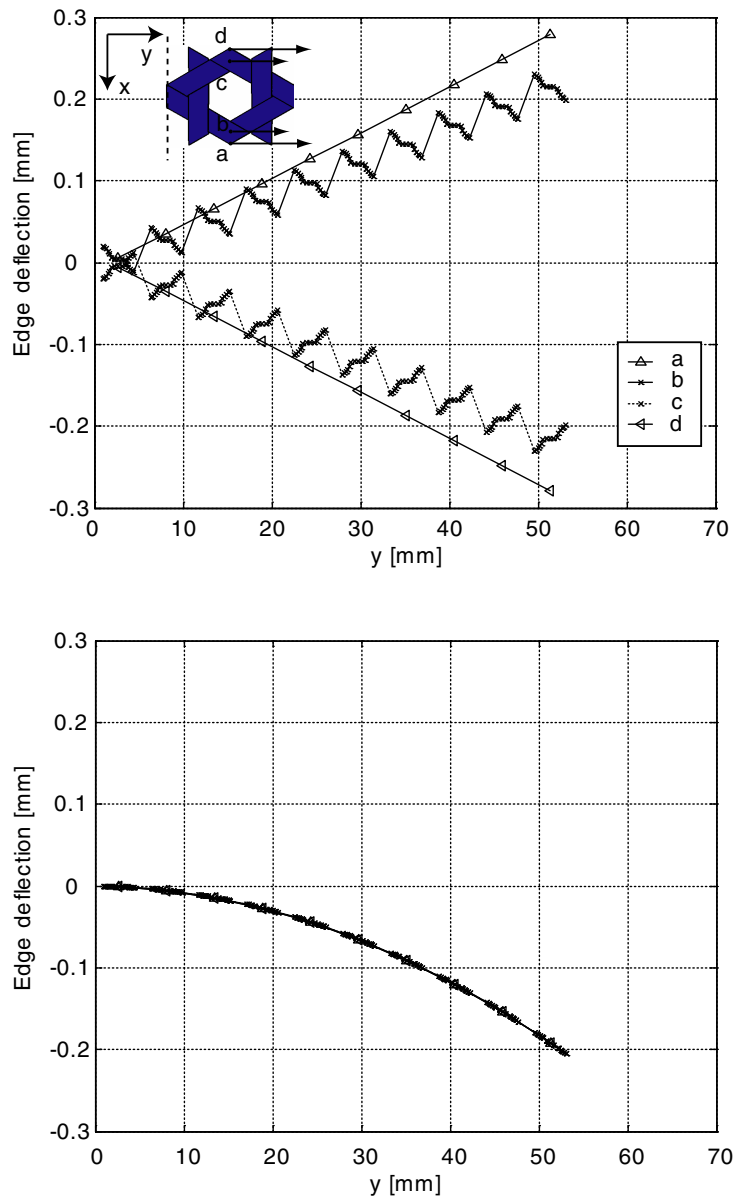


Figure 4.8: Deformation of 90-direction strip subject to (a) a uniform temperature rise of 100°C and (b) a thermal gradient of $\pm 2^\circ\text{C}$.

Chapter 5

Test Methods

This chapter describes the test methods that have been adopted for TWF composites. Some of these methods were developed specifically for the present research.

5.1 Measurement of Tension Properties

5.1.1 Coupons for Tension Tests

The coupon layout is shown in Figure 5.1. To minimize edge effects, an aspect ratio of 1:1 was adopted for the unreinforced area. Ten 90 mm wide \times 190 mm long (including tab lengths) specimens were constructed. Each specimen consisted of a sheet of single-ply TWF, with the 0-direction arranged in the main loading direction, sandwiched between rectangular aluminium tabs (90 mm long \times 50 mm wide and 1 mm thick) and additional 60 mm \times 90 mm sheets of single-ply TWF. These extra reinforcements, tabs and outer layers have the purpose of reducing Poisson's ratio mismatch effects that would lead to premature failure near the clamped area.

The extra layers of TWF were glued to the specimen with Araldite resin and hardener, mixed at a ratio of 1:1. The aluminum tabs were attached to the two ends of the specimen with an industrial superglue. Retro-reflective strips for the laser extensometers, to measure longitudinal and transverse strains, were attached in the central region about 50 mm apart.

5.1.2 Apparatus

The apparatus for this test consisted of an Instron 5578 testing machine, with a 30 KN load cell, an Epsilon LE-01 laser extensometer and an Epsilon LE-05 laser extensometer for measuring longitudinal and transverse strains.

5.1.3 Testing Procedure

The coupon was gripped between wedge clamping jaws and pulled at a rate of 1 mm/min while the deformation, both longitudinal and transverse, was measured by two laser extensometers. The test procedure followed ASTM (2000).

The first three specimens were tested to failure. The remaining specimens were loaded to 60 % of the average maximum tensile force, and then unloaded before being reloaded up to failure,

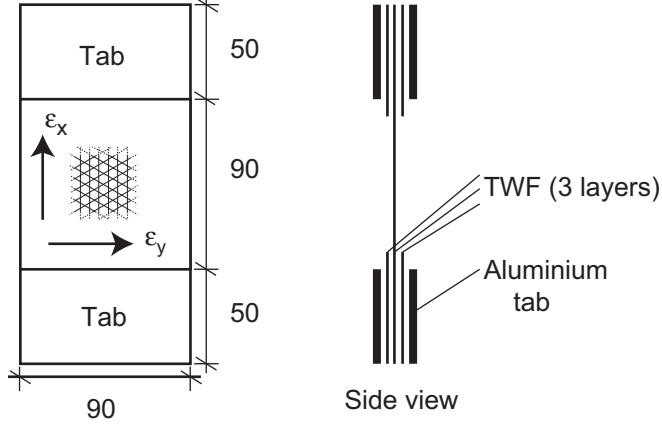


Figure 5.1: Coupon for tension test (dimensions in mm).

in order to investigate any hysteretic response.

5.2 Measurement of Compression Properties

Compression tests on thin composite plates are notoriously difficult, as the failure of interest is fibre microbuckling but other test-dependent failure modes tend to occur at lower loads. Following Fleck and Sridhar (2002), we carry out the compression tests on short sandwich columns, comprising two TWF face sheets bonded to a closed-cell PVC foam core, as shown in Figure 5.2. Fleck and Sridhar have shown that by suitable choice of the properties of the foam the lateral restraint provided by the core can be optimized to prevent failure by overall Euler buckling, core shear macrobuckling, and face wrinkling so that the specimen fails by fibre microbuckling. The particular foam that was used was a closed-cell Polyvinyl chloride (PVC) foam sandwich core (trade name: Divinycell, density 186 kg/m^3) with the following properties:

$$\begin{aligned} \text{Extensional modulus, } E_{core} &= 295 \text{ MPa} \\ \text{Shear modulus, } G_{Core} &= 110 \text{ MPa} \end{aligned}$$

5.2.1 Coupons for Compression Tests

The specimens were designed such that they would fail by fibre microbuckling. Four modes of compressive failure are possible for a sandwich specimen. Euler buckling, core shear buckling, microbuckling and face-sheet wrinkling.

For Euler buckling pinned end conditions are assumed. Hence, the Euler buckling load is

$$P_E = \frac{\pi^2 (EI)_{eq}}{L^2} \quad (5.1)$$

where L is the height of the specimen. The equivalent bending rigidity is given by

$$(EI)_{eq} \approx \frac{S_x c^2 w}{2} \quad (5.2)$$

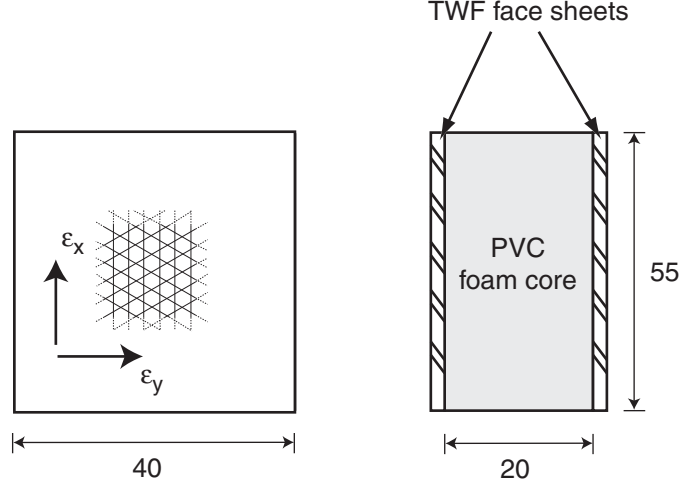


Figure 5.2: Front and side views of coupon for compression test (dimensions in mm).

Here S_x is the extensional stiffness of the TWF face sheet, which can be obtained from the inverse of the ABD matrix, Equation 3.8

$$S_x = \frac{1}{a_{11}} \quad (5.3)$$

also w is the depth of the core, which will be assumed to be 40 mm, and c is the distance between the mid-planes of the two face sheets, which will be assumed to be 20 mm. Substituting Eq. 5.2 into Eq. 5.1 gives

$$P_E = \frac{wS_x}{2} \left(\frac{\pi c}{L} \right)^2 = \frac{40 \times 2114}{2} \left(\frac{\pi \cdot 20}{55} \right)^2 = 55.2 \text{ KN}$$

The core shear buckling load has the expression (Fleck and Sridhar, 2002)

$$P_s = (AG)_{eq} \approx wcG_{core} = 40 \times 20 \times 110 = 88 \text{ KN} \quad (5.4)$$

The combination of these two buckling modes results in a critical load, P_{cr} , given by

$$\frac{1}{P_{cr}} = \frac{1}{P_E} + \frac{1}{P_s} = \frac{1}{55.2} + \frac{1}{88} \quad (5.5)$$

The resulting value is $P_{cr} = 32.8$ kN.

Microbuckling of the fibres occurs when the axial compressive stress reaches the microbuckling strength, σ_{cr} . The resulting load is obtained by multiplying the number of sheets by their cross-sectional area, by one-third (as only one third of the width of the sheet is filled by tows in the direction of the load), by the volume fraction of fibres,

$$P_f = \frac{2}{3} wt \times V_f \sigma_{cr} = \frac{2}{3} \times 40 \times \frac{0.156}{2} \times 0.65 \times 1470 = 1,987 \text{ N} \quad (5.6)$$

where σ_{cr} is the compressive strength of T300 fibers.

The compressive bifurcation stress due to face sheet wrinkling can be estimated from (Fleck and Sridhar, 2002)

$$\sigma_{fw} = 0.5 \left(\frac{S_x E_{core} G_{core}}{t} \right)^{\frac{1}{3}} = 0.5 \times \left(\frac{2114 \times 293 \times 110}{0.156} \right)^{\frac{1}{3}} = 379 \text{ MPa} \quad (5.7)$$

and hence the corresponding failure load is

$$P_{fw} = 2\sigma_{fw} w t = 2 \times 379 \times 40 \times 0.156 = 4,730 \text{ N} \quad (5.8)$$

Selecting the smallest of the above failure loads, it is concluded that the specimen will fail by fibre microbuckling, which is the desired failure mode.

Ten 40 mm wide \times 55 mm long specimens were constructed. Each specimen consisted of two 40 mm \times 55 mm TWF sheets, with the 0-direction tows aligned with the longer direction, and a 20 mm foam sandwich core. The TWF face sheets were bonded to the PVC core using Araldite resin and hardener, mixed at a ratio of 1:1.

5.2.2 Apparatus

The apparatus for this test consisted of an Instron 5578 testing machine with a 2 KN load cell. An Epsilon LE-01 laser extensometer and an Epsilon LE-05 laser extensometer were used to measure the longitudinal strains at the front and back of the sandwich specimen.

5.2.3 Testing Procedure

The specimens were compressed between flat platens at a rate of 1 mm/min while the longitudinal deformation of both face sheets was measured by the two laser extensometers.

An identical test was carried out on a PVC foam specimen with identical dimensions to the core shown in Figure 5.2. At any given value of the strain reading, the value of the force carried by this foam specimen is subtracted from the force measurement on the compression specimen and the resulting force is divided by two, to obtain the force on one TWF sheet.

5.3 Measurement of in-plane Shear Properties

The in-plane shear test aims to determine the in-plane shear properties of the TWF. Figure 5.3 shows the two rails shear test apparatus from ASTM (2001) D4255M. This reference states that the shear test is to be performed on a composite plate clamped, by means of through bolts, between two pairs of loading rails. When loaded in tension, the rails introduce shear forces in the specimen.

A preliminary shear test on a sheet of single-ply TWF, carried out according to the standard specifications, showed that, due to the thinness of the material, the specimen buckles around the top and bottom free edges at the very early stages of the test. Later in the test the wrinkles extend to the whole unclamped region of the specimen. Since any data measured in the buckled state would not be representative of the material shear properties, a new test method had to be devised.

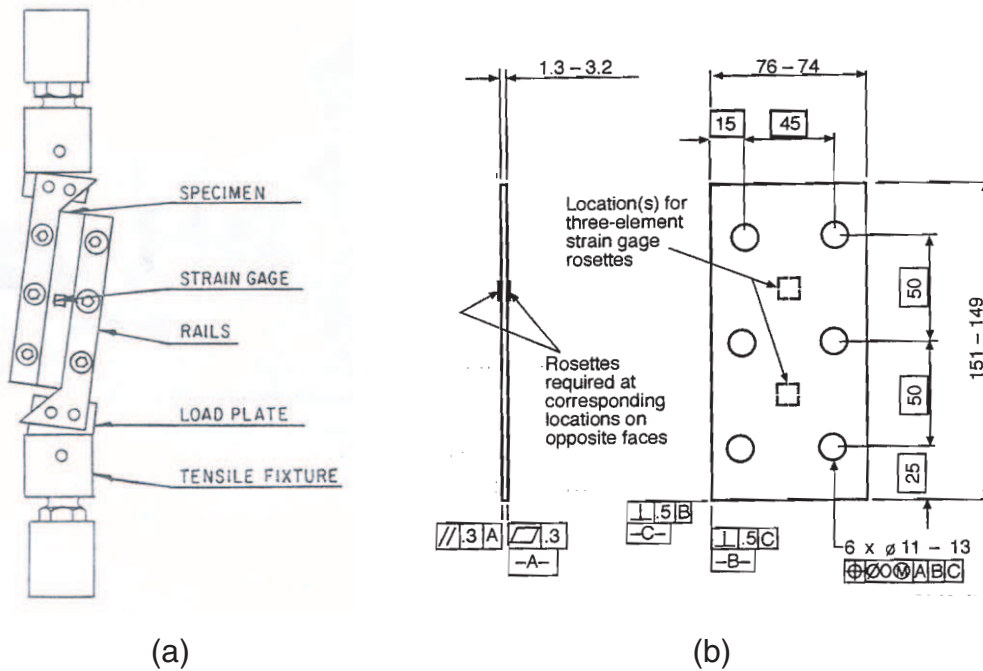


Figure 5.3: Two rails shear test (a) setup (b) specimen (dimensions in mm) (from ASTM D4255).

To prevent buckling of the specimen, it was decided to follow an analogous approach to that of Fleck and Sridhar (2002) for the compression test. Hence a sandwich plate consisting of TWF face sheets and a thin foam core was used, instead of a single sheet. Also, the standard two-rail shear test rig was modified as shown in Figure 5.4. The modification includes increasing the number of bolts from three to six, and using sandpaper between the surface of the specimen and the steel rails. Also, the unconstrained width of the specimen was reduced from 12.7 mm to 10 mm to increase the buckling load.

Measuring the shear strain in the specimen was problematic because the thinness of the material does not allow the use of any contact technique and yet the narrowness of the test region decreases the gauge length over which strain can be measured. An initial attempt to obtain the shear strain from linear strain measurements from two laser extensometers was unsuccessful, as it was discovered that a (small) rigid body rotation of the specimen occurs when the shear strain increases. A minimum of three linear strain measurements would be required to account for this effect, but the test region is too narrow to carry out such measurements.

Two types of strain measuring methods were investigated; photogrammetry and clip gauges.

5.3.1 Photogrammetry Method

The shear strain was measured with the photogrammetry software PhotoModeler Pro 5.2.3. Figure 5.5 shows a shear specimen with six targets attached to its surface. The targets are short, white rubber rods, about 0.5 mm long. The cross-section diameter is about 0.6 mm. The reason for using white targets is to provide a good contrast against the background provided by

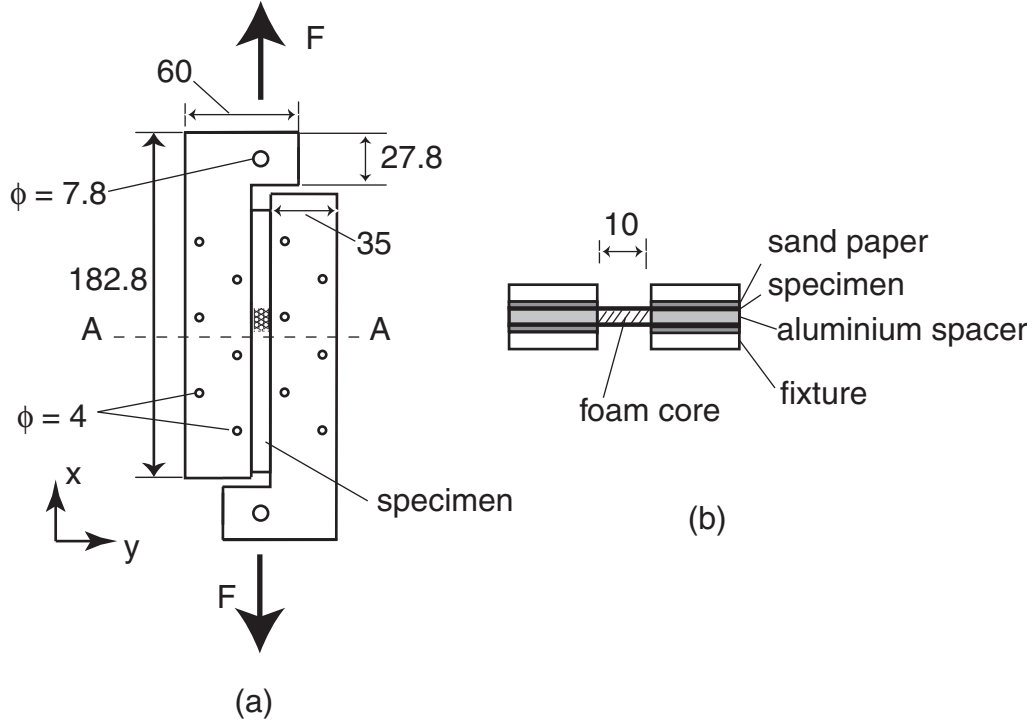


Figure 5.4: (a) Modified shear rig; (b) cross section AA (dimensions in mm).

the specimen and hence improve PhotoModeler's efficiency in detecting the targets. The targets were glued to the tows with polyvinyl acetate (PVA) adhesive which sets within 5 minutes. A Nikon D80 camera with 105 mm F2.8 EX DG macro lens was used to capture pictures of the target region during the test. A timer was used to synchronize the application of the load and the photos.

On each photo, the x and y coordinates of the centroid of each target were measured using the sub-pixel resolution function in PhotoModeler. The origin of the coordinate system and the directions of the x - and y -axes were defined by a number of control points, mounted on the edge of the rig. Out-of-plane displacements were assumed to be negligibly small.

The normal strain between two target points is computed from the distances between the centroids in photo i , $L_{i,\theta}$, and the reference photo with the specimen unloaded, $L_{0,\theta}$

$$\varepsilon_{i,\theta} = \frac{L_{i,\theta} - L_{0,\theta}}{L_{0,\theta}} \quad (5.9)$$

where $\theta = 0^\circ, 45^\circ, 90^\circ$ is the angle between the targets and the x -axis, in the unloaded configuration.

An accuracy of ± 5 microns was obtained on the position of the centroids and, as it will be seen in Section 6.3, this leads to very noisy measurements of the shear strain.

5.3.2 Clip Gauges Method

Figure 5.6 shows the test setup with two clip gauges attached to the rails of the shear rig. The clip gauges were made of a 0.3 mm thick strip of spring steel bent into a circular arc and with

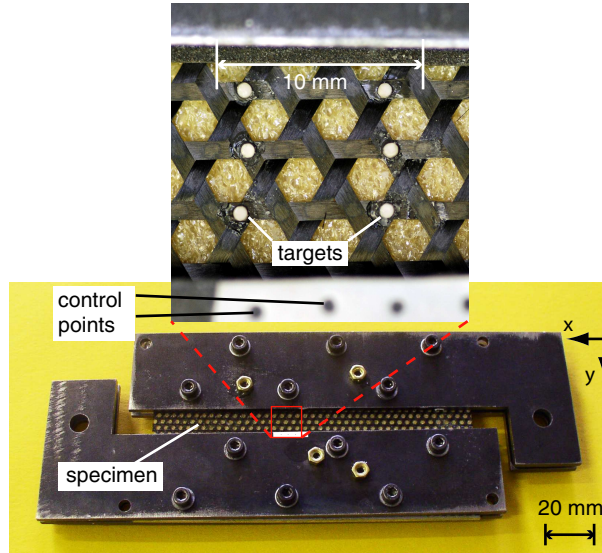


Figure 5.5: Shear specimen with an enlarged view of photogrammetry targets.

sharp tips to clip the gauge into small holes on the rails. The bending strain in each clip gauge is measured by two strain gauges bonded to its surfaces and this reading is correlated with the distance between the tips of the gauge. The strain between the two tip points can be computed from these measurements.

The clip gauges were mounted across the two rails and at 45° to them, in a direction such that the distance between the tip points increases during the test. This arrangement prevents the second clip gauge from falling off during the test.

5.3.3 Coupons for in-plane Shear Tests

Eight 80 mm wide \times 130 mm long specimens with an unsupported width of 10 mm were manufactured. Each specimen consisted of two TWF sheets bonded to a 130 mm long by 10 mm wide, 3 mm thick strip of PVC foam core, between 3 mm thick Aluminium spacers, see Figure 5.4(b). The PVC foam is of the same type used in the compression specimens, Section 5.2.1.

Preliminary tests showed that 3 mm foam thickness was sufficient to prevent the TWF sheets from buckling, but no detailed study of the effects of changing the foam thickness or modulus was carried out.

Of the eight specimens, three were tested with the photogrammetry method and the remaining five with the clip gauges method. All of the specimens had the 0-direction towards parallel to the direction of shearing.

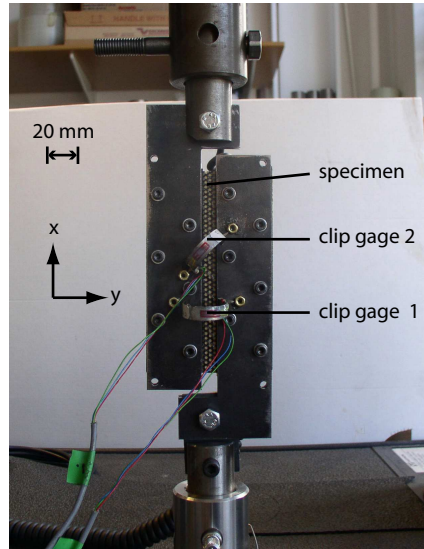


Figure 5.6: Shear test set up with the clip gauges.

5.3.4 Specimen Preparation

Figure 5.7 shows the key steps required to prepare a specimen and install it into the shear rig. The preparation of the shear specimen is as follows:

1. Figure 5.7(i) shows all elements of the test fixture in a disassembled state;
2. Use four bolts to hold the aluminum plates and one of the two TWF sheets in place;
3. Apply Evo-stik impact adhesive on one side of the foam, see Figure 5.7(ii);
4. Attach the 'glued' foam surface to the TWF in the gap between the aluminum plates. The foam acts as the core of the sandwich, see Figure 5.7(iii);
5. Apply Evo-stik impact adhesive on the 'exposed' surface of the foam;
6. Place the second TWF sheet on top of the assembly, using the four bolts as a guide, see Figure 5.7(iv).

The installation steps of the shear specimen into the test rig are as follows:

1. Place the coarse side of one sheet of P1500 sandpaper sheet (average grit size = 15.3 microns) on the inner surface of two of the four L-plates, see Figure 5.7(v);
2. Place the shear specimen on top of the assembly;
3. Put the third and fourth L-plates, with the same grade sandpaper on the inner surface, on top of the assembly;
4. Tighten the assembly with bolts and nuts.

The final assembly of the shear rig can be seen in Figure 5.7(vi). A good bond between the weave and the foam is essential to prevent delamination, especially around the top and bottom edges, during the shear test.

5.3.5 Apparatus

The apparatus for this test consisted of an Instron 5578 testing machine with a 2 KN load cell, and either six targets on each specimen and a Nikon D80 digital camera with 105 mm F2.8 EX DG macro lens (photogrammetry method), or two clip gauges (clip gauges method).

5.3.6 Testing Procedure

The shear rig was pinned to the adaptors and mounted onto the Instron testing machine. The tension rig was pulled at a rate of 0.5 mm/min while the deformation of the specimen was measured using either the photogrammetry method, in which case the strains in 0°-, 90°-, and ±45°-direction, were measured from the photos after the test, or the clip gauges method, in which case the strains in 0°- and 45°-direction, were measured.

5.3.7 Analysis of Measured Data

After each test, the normal strains measured during the test are used to compute the shear strain, assumed to be uniform throughout the specimen. The key relationship is

$$\varepsilon_{xy} = 2\varepsilon_{45} - \varepsilon_0 - \varepsilon_{90} \quad (5.10)$$

In the photogrammetry method all three normal strains, $\varepsilon_0, \varepsilon_{45}, \varepsilon_{90}$ have been determined from the photos of the targets. In the clip gauges method it is assumed that the strain $\varepsilon_0 = 0$ and the remaining two strains are obtained by dividing the clip gauge extensions by the initial gauge lengths.

The shear force per unit length of TWF sheet, N_{xy} , is determined by subtracting from the measured force values the shear force carried by the foam core, and dividing the result by 2 (because the sandwich specimen contains two sheets of TWF). The shear force in the core is obtained from

$$N_{xy}^c = G_{core}\varepsilon_{xy}t \quad (5.11)$$

where $G_{core} = 110$ MPa is the shear modulus and $t = 3$ mm the thickness of the core.

5.4 Measurement of Bending Properties

Two types of bending tests were carried out; a 4-point bending test to measure the bending stiffness of single-ply TWF and a squashing test between two end plates to measure the curvature at failure.

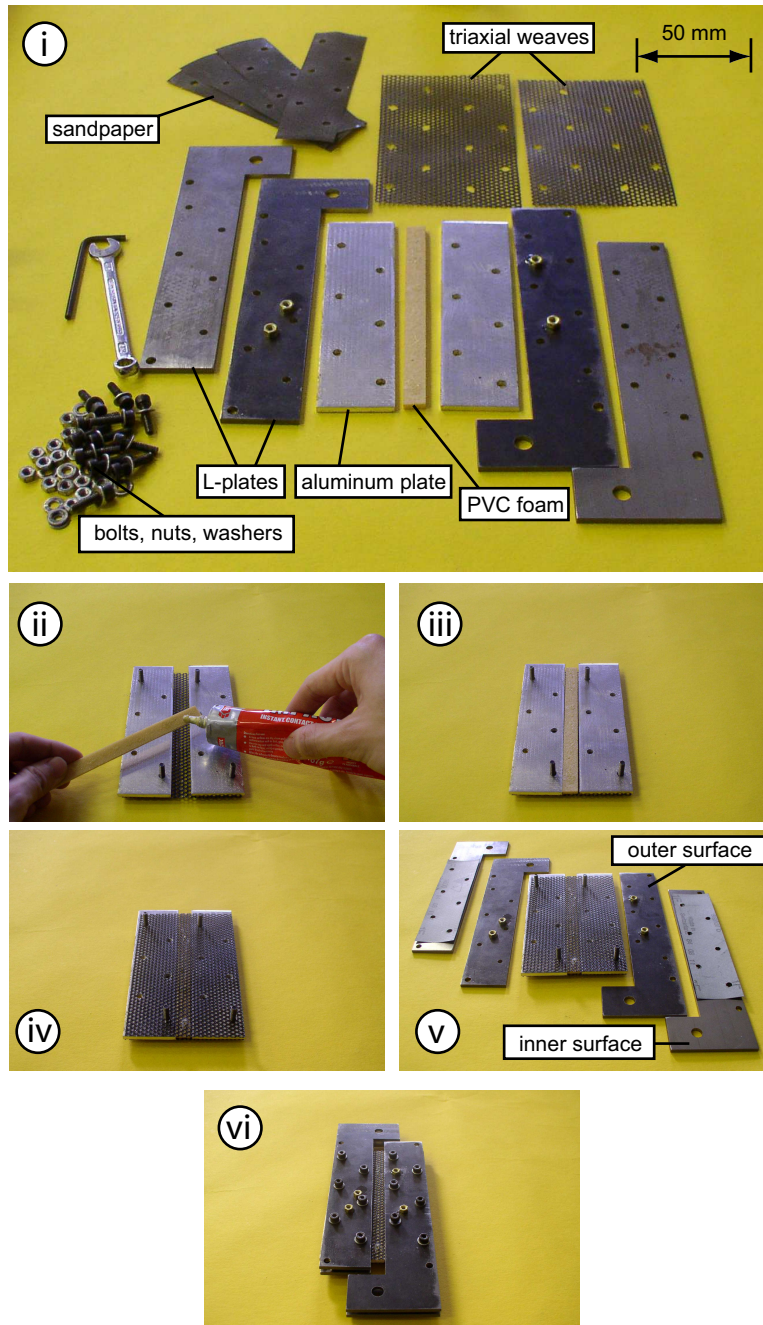


Figure 5.7: Shear specimen preparation and rig installation.

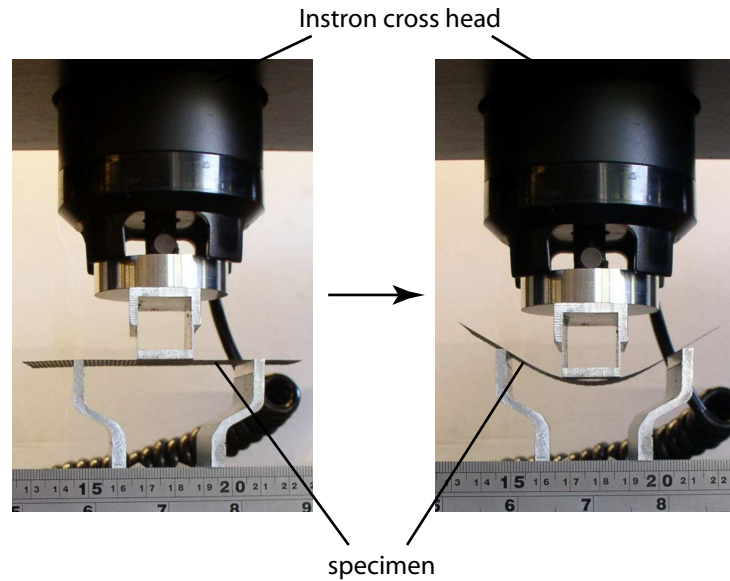


Figure 5.8: 4-point bending test setup showing highly exaggerated deflection, scale in mm.

5.4.1 Bending Modulus Measurement

A 4-point bending configuration was chosen, instead of 3-point bending, as it produces a region subject to a uniform bending moment and so it is more reliable. The test setup, based on ASTM (1986), is shown in Figure 5.8.

The span between the outer supports was 60 mm and the distance between the (inner) two points at which the loading was applied was set at 20 mm, in order to achieve an aspect ratio of 0.5 in the region that is subject to uniform bending moment. The deflections imposed during this test were very small, the maximum value of δ being in the region of 0.6 mm, corresponding to a deflection-to-span ratio in the region of 33; the maximum value of the applied load was in the region of 0.1 N. Friction effects associated with longitudinal deflections at the supports were negligible.

5.4.2 Coupons for Bending Modulus Tests

Five 100 mm long \times 40 mm wide, rectangular coupons with the 0-direction tows aligned with the longer edge were tested. The width of the specimen, $w = 40$ mm, was chosen to match the width of the compression specimens.

5.4.3 Apparatus

Tests were performed using an Instron 5578 machine with a 100 N load cell. An Epsilon LE-05 laser extensometer was used to measure the deflection.

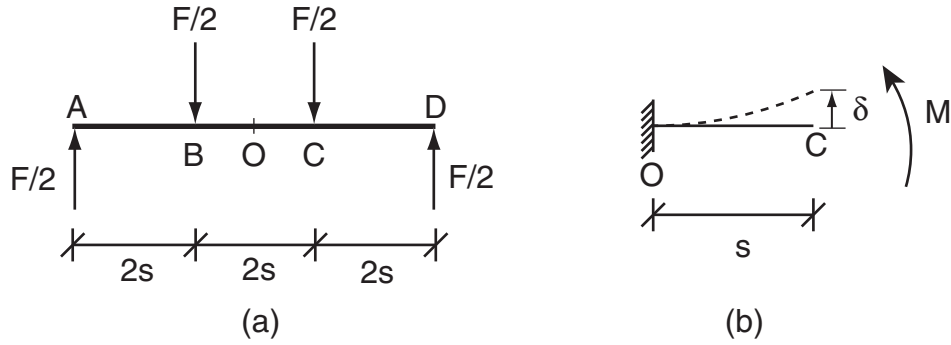


Figure 5.9: (a) Free-body diagram for 4-point bending test and (b) deflection of central span.

5.4.4 Testing Procedure

A displacement rate of 1 mm/min was used to perform the test. A retro-reflective strip was attached to the edge (only a narrow region needs to be exposed to the laser beam to obtain a noise-free signal) of the specimen. Another strip was attached to the loading head. The laser extensometer was used to measure the distance between the two strips.

5.4.5 Analysis of Measured Data

The quantities measured during the test are the overall force, F , and the relative deflection, δ , see Figure 5.9. They can be related to the bending moment in the central part of the specimen, M , and the curvature, κ , as follows.

The required relationship between M and F is found by evaluating the moment in the central span BC

$$M = Fs \quad (5.12)$$

To find the second relationship, write the moment-curvature relationship as

$$\kappa = \frac{M}{EI} = \frac{Fs}{EI} \quad (5.13)$$

Then note that the tip deflection δ of a cantilever of span s and bending stiffness EI , subjected to an end moment Fs is

$$\delta = \frac{Fs^3}{2EI} \quad (5.14)$$

This relationship can be written as

$$\frac{Fs}{EI} = \frac{2\delta}{s^2} \quad (5.15)$$

Substituting Equation 5.15 into Equation 5.13 gives

$$\kappa = \frac{2\delta}{s^2} \quad (5.16)$$

which is the second equation that we require.

Equations 5.12 and 5.16 can be adapted to the bending of a plate of width w , subject to a uniform moment per unit length M_x , into a cylindrical surface by substituting $M_x = M/w$

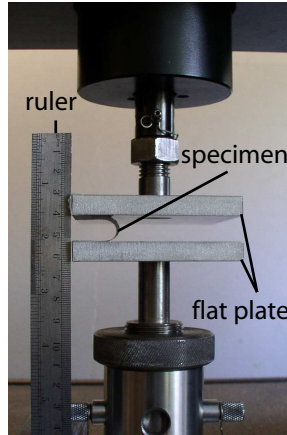


Figure 5.10: Test setup for squashing test.

and $\kappa_x = \kappa$. The assumption of bending into a cylindrical surface is reasonable since the width of the constant-moment region of the plate is twice the length, and it is supported over its full width. Note also that $EI = D_{11}w$ although this relationship is not needed. Hence we obtain

$$M_x = \frac{Fs}{w} \quad (5.17)$$

and

$$\kappa_x = \frac{2\delta}{s^2} \quad (5.18)$$

5.5 Measurement of Failure Curvature

The test setup can be seen in Figure 5.10. The test aims to determine the smallest radius to which single-ply TWF composites can be folded before breaking.

5.5.1 Coupons for Squash-Bend Tests

Ten 40 mm wide by 50 mm long, rectangular specimens were tested. In these coupons the 0-direction tows are aligned with the longer edge of the coupon.

5.5.2 Apparatus

The specimens were squashed using an Instron 5578 machine using a 100 N load cell. The test was recorded with a digital video camera.

5.5.3 Testing Procedure

The specimen is taped to the edges of two flat plates mounted on an Instron testing machine. The two plates are brought closer together, thus squashing the specimen between them. When the plates are sufficiently close, the deformation of the specimen becomes localised in a narrow cylindrical region, which breaks suddenly when the failure curvature of the specimen is reached.

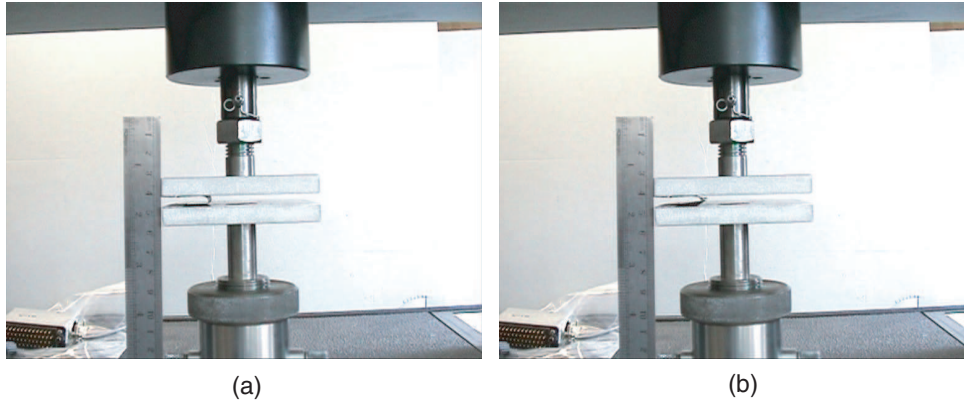


Figure 5.11: Failure curvature test images just before and after failure.

The plates were moved at a rate of 10 mm/min. The images recorded just before the failure of the specimen were analyzed in detail and the minimum radius to which the specimen can be folded without failure is half of the distance between the two plates in the image just before the specimen fails. Two such images are shown in Figure 5.11.

5.6 Measurement of Linear Coefficient of Thermal Expansion

The aim of these tests was to determine the linear coefficient of thermal expansion. It was decided to focus on the 0-direction as previous work (Kueh, Soykasap and Pellegrino, 2005) has shown that the CTE in the 90-direction has a similar value.

5.6.1 Coupons for CTE Tests

TWF is too thin to carry out CTE tests on flat strips, as a flat strip cannot be guaranteed to remain straight under the weight load applied by the dilatometer. Hence, the coupon layout previously adopted by Kueh, Soykasap and Pellegrino (2005) was selected.

The TWF was cured on a 20 mm diameter mandrel. Coupons were made by cutting 50 mm long cylinders and wrapping them with Kevlar fibres down to a diameter just below 8 mm, see Figure 5.12. Compared to previous work (Kueh, Soykasap and Pellegrino, 2005), a smaller mandrel diameter was used, in order to achieve a final diameter of less than 8 mm after wrapping. The aim was to ensure that the quartz disc of the dilatometer, put on top of the specimen, is firmly supported by the specimen.

Six cylindrical specimens with a nominal length of 50 mm (actual lengths between 49.6 and 50.5 mm) were tested. The results from one of the cylinders were not repeatable and were discarded. All specimens were rather dry, and it is likely that the fibre volume fraction — although it was not measured— was higher than in the flat specimens used for all other tests.

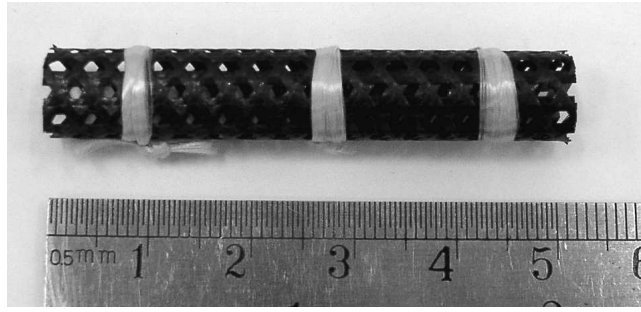


Figure 5.12: Cylindrical sample for CTE measurement.

5.6.2 Apparatus

A WSK TMA 500 dilatometer was used for the CTE measurements. This instrument is able to carry out tests over the temperature range from 200°C to +500°C. It is equipped with a specimen mounting plate, connecting rod and mechanical, optical or electronic length variation measuring instruments (margin of error 0.05 μm) for temperatures over 300°C. It also has a vacuum or inert gas mechanism. The heating furnace of the dilatometer keeps the temperature constant over the length of the specimen (tolerance 0.5%). A thermo-couple is used to determine the temperature in the middle of the specimen.

5.6.3 Testing Procedure

Each coupon was subjected to a minimum of 3 cycles over the full temperature range -150°C to 120°C, at a heating rate of 5°C/min. Throughout the test the extension and temperature of the coupon were recorded.

The measurements taken during the first cycle are disregarded. The extensions measured in the remaining cycles are divided by the initial length of the coupon in order to compute the longitudinal strains. Finally, the strains at corresponding temperatures are averaged in order to obtain a single relationship between thermal strain and temperature for each specimen.

5.7 Measurement of Thermal Twist

The aim of these tests was to measure the relationship between twist and temperature in 0-direction and 90-direction narrow strips of TWF composite that were held fixed at one end. The reason for testing narrow strips of material is to avoid the complex buckle patterns that have been observed in wider specimens by Kueh and Pellegrino (2006). The heating was applied very quickly in order to investigate time-dependent viscoelastic effects; in the end these were found to be rather small and so will not be described in this report.

The torsional stiffness of the strips is small and hence a non-contact measurement technique was adopted. The twist of the end section of the strips was obtained by measuring the deflection of two points close to the edges of the strip, using laser displacement sensors. To further amplify these readings, the ends of the strips were widened by attaching small composite plates.

A photograph of the test setup is shown in Figure 5.13 and a more detailed explanation is provided by the schematic view in Figure 5.14. The strip is clamped vertically down and the deflections of edge 1 and edge 2 are measured. These tests were performed in a low moisture environment to eliminate shape changes associated with changes in moisture content.

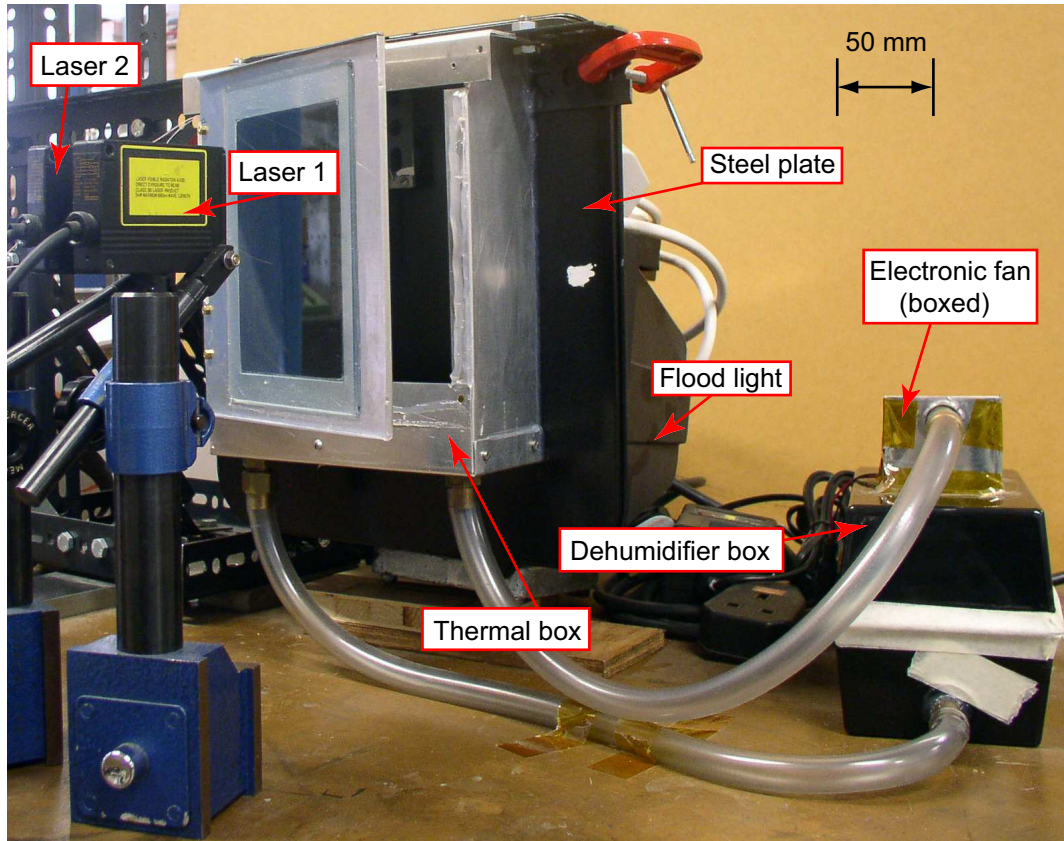


Figure 5.13: Thermal twist test setup.

5.7.1 Coupons for Thermal Twist Tests

Figure 5.15 shows the thermal twist test specimens. Two single-unit-wide coupons, approximately 80 mm long, were prepared. The 0-direction specimen was 5.4 mm wide; the 90-direction specimen was 3.1 mm wide. The coupons were cut from a flat sheet of cured material using a pair of scissors for composite materials, under a magnifying glass. When cutting these strips it is important to avoid cutting through the interweaved regions in order to ensure that they are not damaged.

A 12 mm long, flat plate of single-ply T300/Hexcel 8552 composite material (3 mm wide \times 0.22 mm thick) was attached to the end of each strip using Loctite 3608 adhesive. The adhesive was cured at 130°C, within 1 minute, by the heat applied from a soldering iron. The surface of the plate was painted with a white Tipp-Ex fluid to achieve a good reflective surface for the laser measurement.

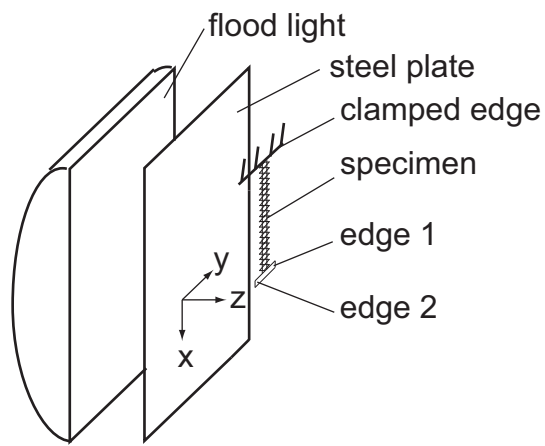


Figure 5.14: Schematic view of thermal twist test layout.

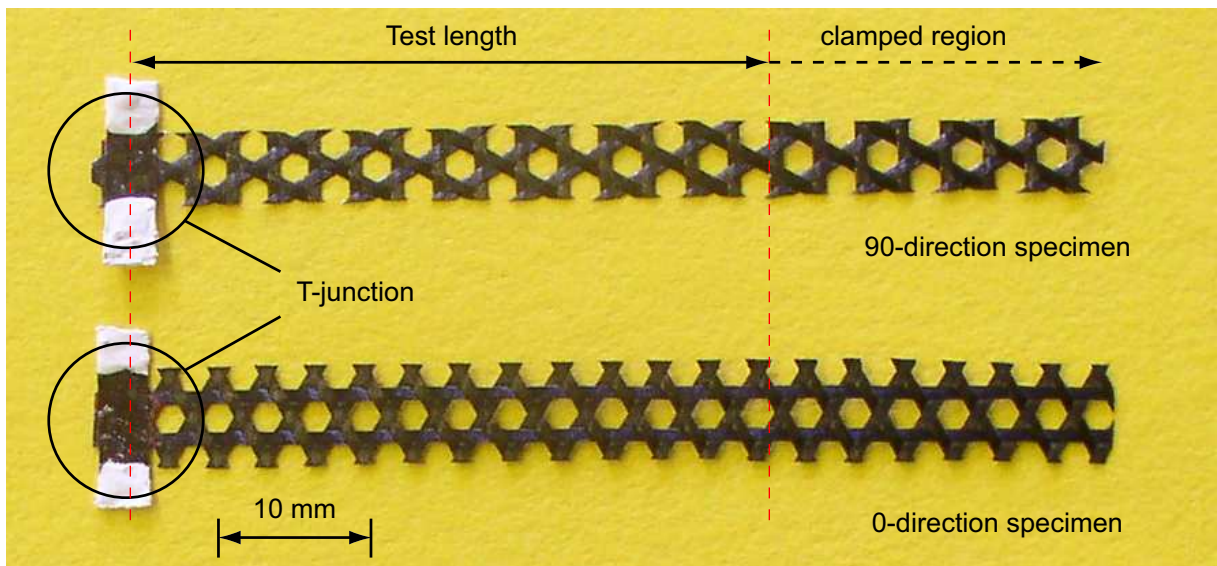


Figure 5.15: Specimens for thermal twist test

5.7.2 Apparatus

1. 1 KW 230V~50 Hz flood light
2. 195 mm wide \times 230 mm long \times 65 mm deep thermal box equipped with a sealed glass door.
3. 300 mm wide \times 300 mm long \times 0.5 mm thick black-painted steel plate
4. 100 mm wide \times 160 mm long \times 120 mm high dehumidifier box, filled with silica gel and equipped with an electric fan
5. Two LAS-8010V laser displacement sensors to measure the tip displacements of the strip; these sensors have a resolution of 50 μm
6. Two thermo-couples, placed on the top and bottom surface of the TWF strip, to measure the thermal gradient across the thickness.
7. Variac

5.7.3 Testing Procedure

All specimens were held in a vacuum for 24 hours to ensure a low moisture content. Three thermal cycles were applied to each specimen.

To achieve a low humidity testing environment, the air inside the thermal box was circulated through a box filled with silica gel for 20 minutes, with an electric fan. This reduces the relative humidity to 15 %. The air circulation was then stopped, allowing for heating. The heat was provided by radiant heating from a flood light against a black painted plate, increasing the temperature in the thermal chamber very quickly. The light intensity was controlled with a variac. The thermo-couples were not attached to the specimen. They were attached to an identical TWF strip with silicon rubber adhesive. The two TWF strips were clamped in a cantilever configuration, side by side and a distance of 10 mm apart. This distance is sufficiently close for the same temperature to be applied to both strips.

One thermal cycle involves a temperature increment from room temperature to 100°C within 2 minutes, natural cooling to room temperature, and followed by regular monitoring of the specimen's deformation for 24 hours. The air was recirculated once the thermal box had reached room temperature. The same procedure was repeated in each cycle. The out-of-plane displacement of the specimens' tip edges were measured with two laser displacement sensors.

Chapter 6

Test Results

6.1 Results of Tension Tests

A typical load-deformation plot from the tension tests shows non-linear effects associated with tow waviness changes (crimp interchange).

Figure 6.1 shows a plot of force/width vs. longitudinal strain for one of the specimens that were tested, specimen T6. Two straight lines have been added to the plot. The strain at the intersection of these lines is defined as the *transition strain*. The slope increases after the transition strain.

A more significant non-linearity is seen in a plot of transverse strain vs. longitudinal strain, from which a strain-dependent Poisson's ratio can be calculated.

Both of these effects are due to the fact that the tows are not straight. Straightening the tows in tension has the effect of increasing the weave extensional stiffness while decreasing the Poisson's ratio. The stiffness will continue to increase, although much less rapidly, up to failure of the material. The opposite is true for the Poisson's ratio.

The extensional stiffness in the 0-direction, S_{tx} , in N/mm, can be computed from the initial slope

$$S_{tx} = \frac{\Delta N_x}{\Delta \varepsilon_x} \quad (6.1)$$

The longitudinal Poisson's ratio, ν_{xy} , can be determined from

$$\nu_{xy} = -\frac{\Delta \varepsilon_y}{\Delta \varepsilon_x} \quad (6.2)$$

where $\Delta \varepsilon_y$ is the change of transverse strain. The force per unit width at failure, $N_{x,t}^u$, and the failure strain, ε_t^u , were also measured during the test.

Ten force/width vs. strain plots from the tension tests are shown in Figure 6.2. From these plots we have calculated both stiffness and Poisson's ratio, before and after the transition strain (denoted by subscripts 1 and 2 respectively); their values are listed in Table 6.1.

Some of the specimens, e.g. T7, gave an anomalous initial response. This is a feature of testing specimens of small thickness, where a small initial curvature in the longitudinal direction would result in zero initial stiffness and a small transverse curvature would result in a very large

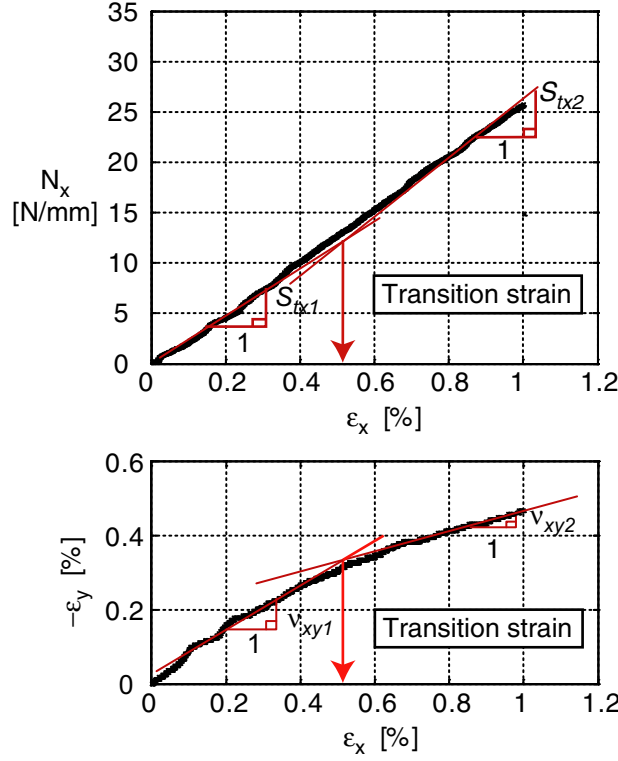


Figure 6.1: Definition of transition strain.

apparent Poisson's ratio. To obtain the Poisson's ratio, we neglect the horizontal part. Since the initial slope of the longitudinal response is constant up to a strain of, in most cases, 0.5%, the initial transverse response is also computed up to this strain. This is done after omitting the horizontal part. The response after the transition strain is stable, thus making the computation of the Poisson's ratio rather straightforward.

6.2 Results of Compression Tests

Ten plots of measured force per unit width vs. strain from the compression tests are shown in Figure 6.3. In general, the axial stiffness in compression, S_{cx} in the fibre direction, can be computed from the initial slope, as follows

$$S_{cx} = \frac{\Delta N_x}{\Delta \varepsilon_x} \quad (6.3)$$

Some specimens, e.g. C06, showed a softer response at the beginning of the test. It is believed that this behaviour occurred when the specimen did not make full contact with the load platens at the beginning of the test. The force per unit width at failure, $N_{x,c}^u$, and the failure strain, ε_c^u , were also measured in each compression test.

The measured compression properties are summarized in Table 6.2. The data for specimen C09 has been omitted from the table, as the initial part of this test was not recorded. Note that there is a larger variation, 13.86%, in the failure strain in compression than in tension, 11.36%.

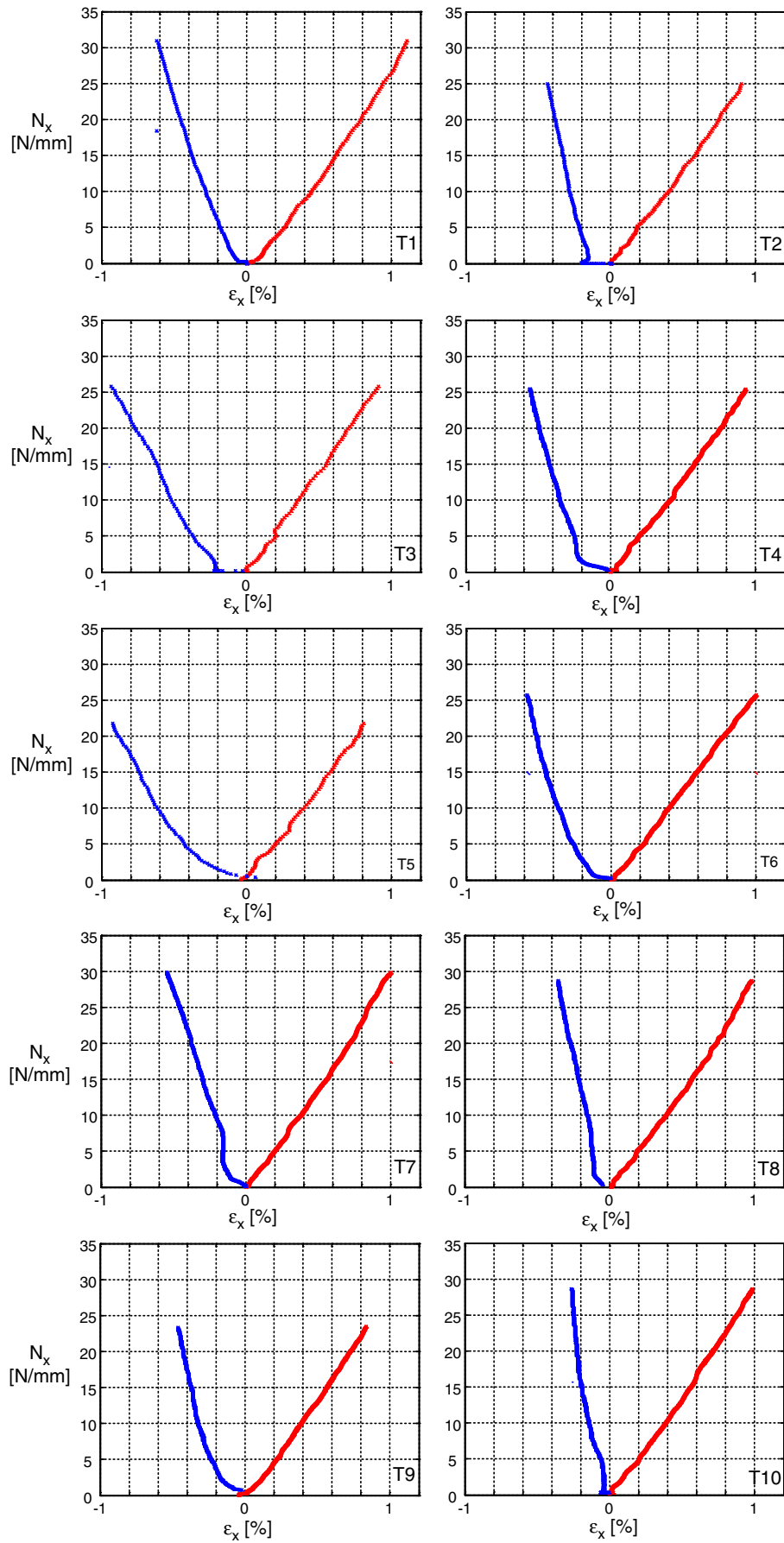


Figure 6.2: Measured force per unit width vs. strain response from tension tests.

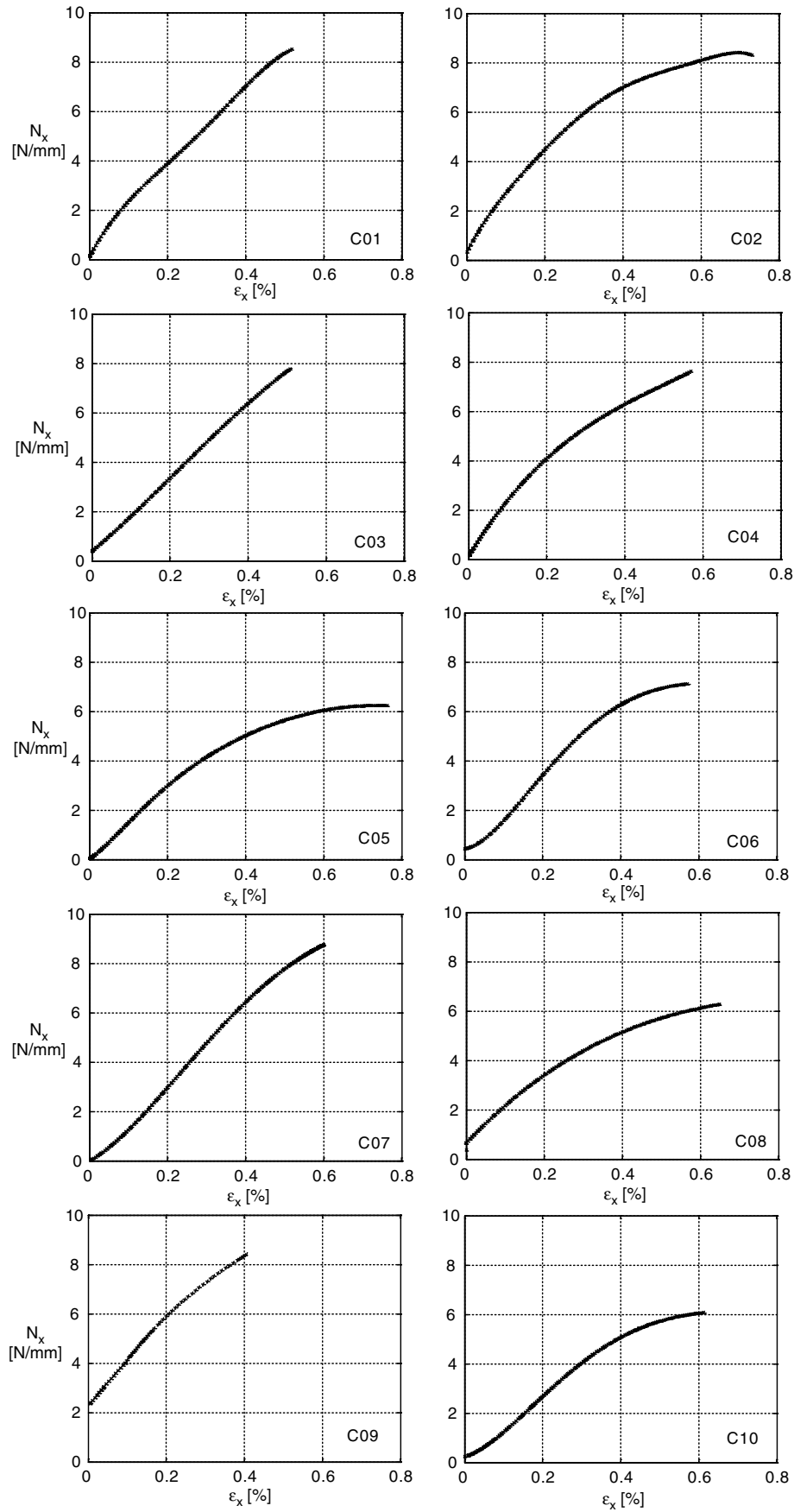


Figure 6.3: Measured force per unit width vs. strain response from compression tests.

Table 6.1: Tension test results

Specimen	S_{tx1} [N/mm]	S_{tx2} [N/mm]	ν_{xy1}	ν_{xy2}	$N_{x,t}^u$ [N/mm]	ε_t^u [%]
T1	2100.3	3278.7	0.564	0.428	30.97	1.11
T2	2062.8	3015.1	0.541	0.360	24.99	0.90
T3	2067.0	3028.0	0.663	0.422	25.83	0.91
T4	2069.5	3129.7	0.561	0.408	25.44	0.93
T5	2245.8	3088.0	0.658	0.466	21.75	0.81
T6	2250.0	3075.6	0.564	0.358	25.73	1.00
T9	2069.5	3066.5	0.558	0.421	23.46	0.84
T10	2024.8	3098.0	0.690	0.388	28.62	1.08
Average	2111.2	3097.5	0.600	0.406	25.85	0.95
Std. dev.	86.80	81.96	0.060	0.036	2.86	0.11
Variation [%]	4.11	2.65	9.92	8.98	11.07	11.36

6.3 Results of Shear Tests

Five plots of measured shear force/length vs. shear strain (measured with the clip gauges) are shown in Figure 6.4. The force per unit width values refer to one sheet of TWF and the force carried by the core has already been subtracted. The behaviour observed in the five tests is broadly similar, and the key parameters obtained from each test are summarized in Table 6.3. Note that the shear failure force per unit width and strain are represented by N_{xy}^u and ε_{xy}^u , respectively.

No premature failures near the clamped region of the specimens were observed, indicating that the sandwich specimen configuration adopted for these tests works well.

The shear stiffness, S_{xy} , can be determined from the initial slope of the shear load vs. shear strain plot, as follows

$$S_{xy} = \frac{\Delta N_{xy}}{\Delta \varepsilon_{xy}} \quad (6.4)$$

Figure 6.5 shows the best results that we were able to obtain with the photogrammetry method. Note that the force plotted on the vertical axis is the total shear force, i.e. including the contribution of the foam core and both sheets of TWF. It can be seen that the strain measurements from this method are rather noisy; for this reason the photogrammetry method was not pursued further.

6.4 Results of Bending Tests

6.4.1 Four-Point Bending Tests

Five plots of bending moment per unit width, M_x , vs. curvature, κ_x , are shown in Figure 6.6. All plots show a gradual decrease in slope.

Table 6.2: Compression test results

Specimen	S_{cx} [N/mm]	$N_{x,c}^u$ [N/mm]	ε_c^u [%]
C01	2178.8	8.59	0.52
C02	2218.7	8.46	0.72
C03	2220.9	7.87	0.52
C04	2290.3	7.48	0.57
C05	2299.4	6.85	0.77
C06	2280.5	7.85	0.57
C07	2346.2	8.63	0.6
C08	2328.7	6.81	0.64
C10	2036.9	6.23	0.62
Average	2244.5	7.64	0.61
Std. dev.	95.18	0.87	0.09
Variation [%]	4.24	11.33	13.86

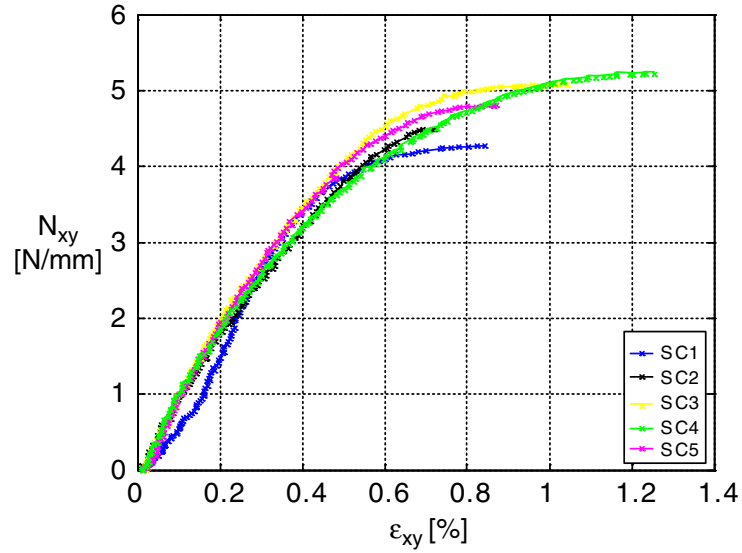


Figure 6.4: Shear force per unit length vs shear strain.

Table 6.3: Shear test results (from clip gages)

Specimen	S_{xy} [N/mm]	N_{xy}^u [N/mm]	ε_{xy}^u [%]
SC1	666.0	4.38	0.84
SC2	737.5	4.79	0.72
SC3	828.6	5.33	1.02
SC4	839.7	5.69	1.21
SC5	813.8	5.02	0.86
Average	777.12	5.04	0.93
Std. dev.	73.874	0.501	0.189
Variation [%]	9.51	9.94	20.37

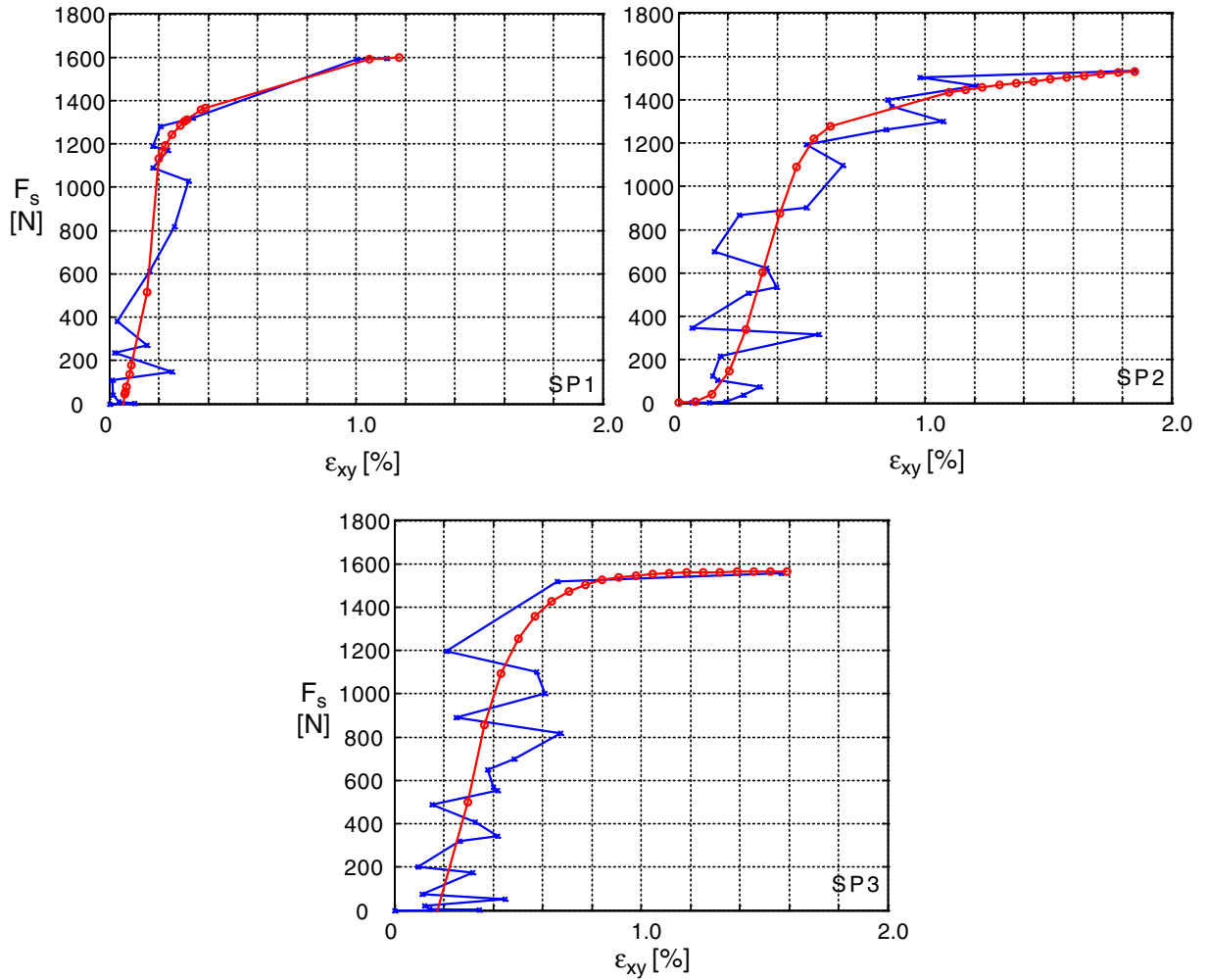


Figure 6.5: Measured shear force vs. shear strain from photogrammetry method.

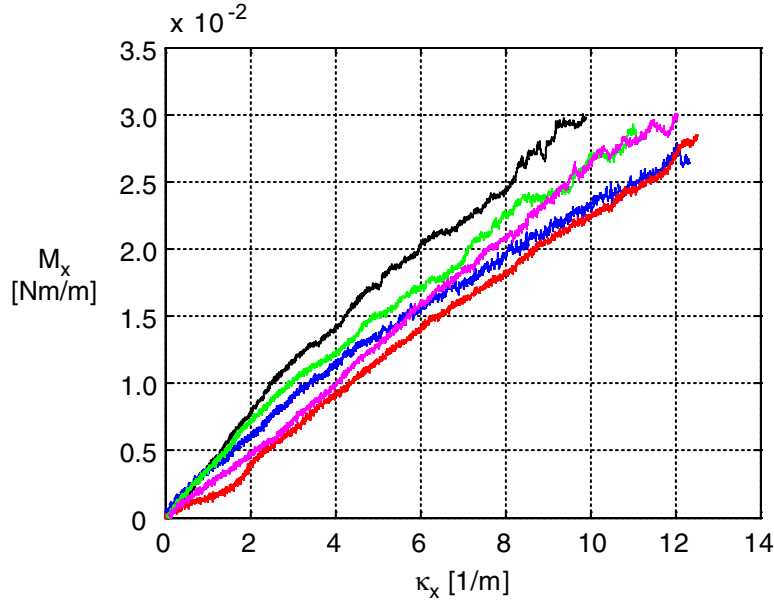


Figure 6.6: Bending moment per unit width vs. curvature from 4-point bending tests.

Table 6.4: Measured bending stiffness

Specimen	bending stiffness, D_{11} [Nmm]
B01	2.008
B02	2.046
B03	2.092
B04	2.108
B05	2.132
Average	2.077
Std. dev.	0.050
Variation [%]	2.40

The bending stiffness in the 0-direction, D_{11} , is given by the initial slope of these plots, after discarding any anomalous response

$$D_{11} = \frac{\Delta M_x}{\Delta \kappa_x} \quad (6.5)$$

The measured bending stiffnesses obtained from this calculation are listed in Table 6.4. It can be seen that there is only a small scatter in the experimental data.

6.4.2 Squashing Tests

The minimum radiuses and failure curvatures, measured from 10 squashing tests on 0-direction specimens, are listed in Table 6.5. The average radius at failure was 2.6 mm, with only a very small variation.

Table 6.5: Failure curvature test results

Specimen	Minimum radius, R_{min} [mm]	Failure curvature, κ^u [1/mm]
1	2.554	0.392
2	2.672	0.374
3	2.716	0.368
4	2.716	0.368
5	2.601	0.385
6	2.503	0.400
7	2.601	0.385
8	2.713	0.369
9	2.692	0.372
10	2.592	0.386
Average	2.636	0.380
Std. dev.	0.076	0.011
Variation [%]	2.88	2.91

6.5 Results of CTE Tests

Plots of the measured relationship between thermal strain and temperature for five cylindrical coupons with the 0-direction aligned with the axis of the cylinder are shown in Figure 6.7. It can be seen that the plot for specimen TE3 shows an anomalous behaviour at colder temperatures. Excluding this specimen, the other plots show a uniform behaviour. Generally, the slope is larger for temperatures higher than room temperature, but become smaller at lower temperatures.

The CTE of a specimen can be determined from

$$\alpha = \frac{\Delta \varepsilon_x}{\Delta T} \quad (6.6)$$

An overall average of the measurements gives a value of $0.957 \times 10^{-6} \text{ degC}^{-1}$.

Table 6.6: CTE test results

Specimen	CTE $\times 10^{-6}$ [$^{\circ}\text{C}$]
TE1	1.067
TE2	0.664
TE3	0.969
TE4	0.969
TE5	1.117
Average	0.957
Std. dev.	0.176
Variation [%]	18.38

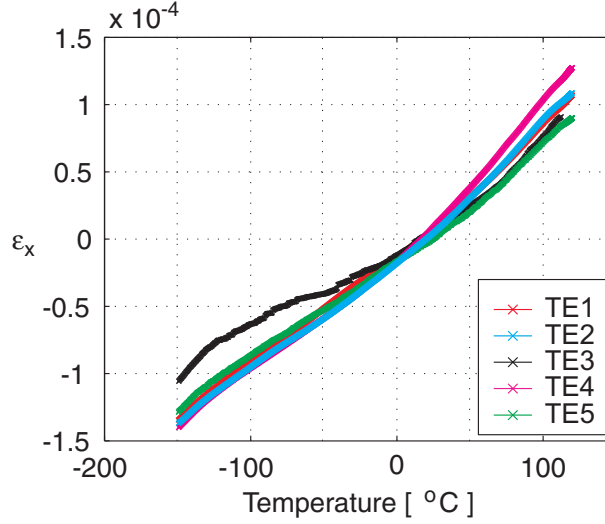


Figure 6.7: Thermal strain vs. temperature measurements.

6.6 Results of CTT Tests

Figures 6.8-6.9 show plots of the displacements of two points at the tip of a 0-direction strip and a 90-direction strip, vs. the average temperature during the third and final thermal cycle. Note that the edge that moves up in Figure 6.8 is edge 1, but in Figure 6.9 is edge 2. This is because corresponding points on two different strips have to go one up and one down, for the whole TWF sheet to twist as a single piece. The sign of the displacement is further discussed in Section 7.3.2.

The experimental data defining the deflection of points on two opposite edges of two nominally identical strips, during the temperature increase part of the cycle, has been fitted with straight lines in both Figure 6.8 and Figure 6.9.

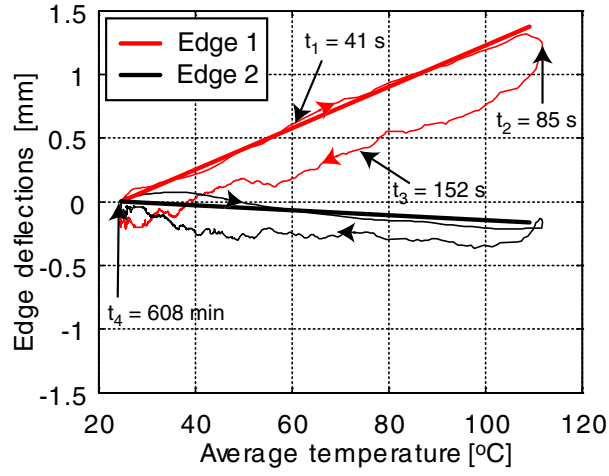
The corresponding twist per unit length of each strip, or Coefficient of Thermal Twist, β , can be determined by dividing Equation 3.6 by the total temperature change, hence

$$\beta = -2 \frac{\Delta w}{dL\Delta T} \quad (6.7)$$

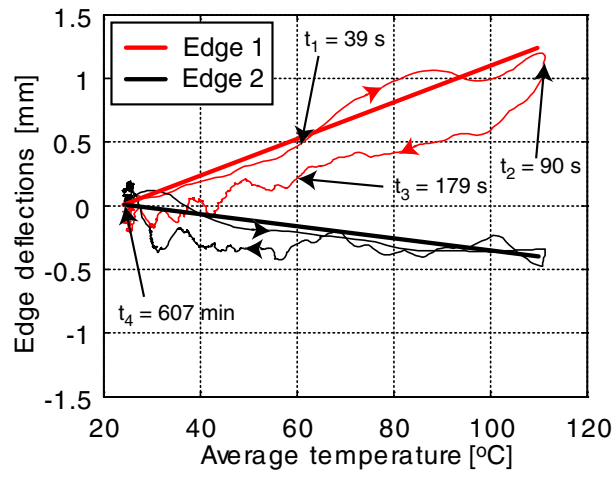
where

- Δw = difference in out-of-plane deflection between two tip edges
- d = distance between edge points measured by two lasers (9.1 mm in both strips)
- L = strip length
- ΔT = change of temperature

Table 6.7 lists the values of the CTT for the 0-direction and 90-direction strips, all measured from the ‘heat up’ part of the test. The table indicates that the 90-direction strip twists more than the 0-direction strip. Note that all values of β are negative, indicating that a negative twisting curvature develops in a TWF composite when it is heated. The average CTT’s are $\beta_0 = -7.082 \times 10^{-5} \text{ mm}^{-1} \text{ }^\circ\text{C}^{-1}$ and $\beta_{90} = -9.010 \times 10^{-5} \text{ mm}^{-1} \text{ }^\circ\text{C}^{-1}$ for the 0-direction and

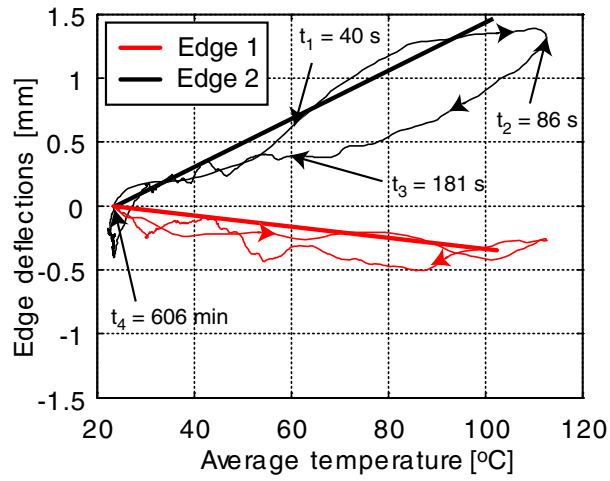


(a)

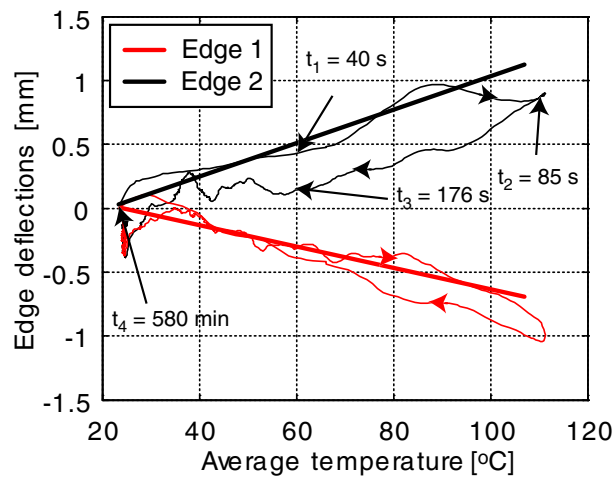


(b)

Figure 6.8: Tip edge deflections vs. average temperature measurements for two nominally identical 0-direction strips.



(a)



(b)

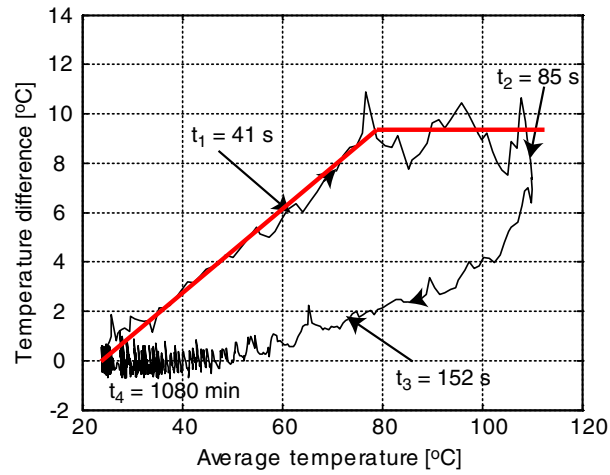
Figure 6.9: Tip edge deflections vs. average temperature measurements for two nominally identical 90-direction strips.

Table 6.7: CTT test results (units $\text{mm}^{-1} \text{ }^\circ\text{C}^{-1}$)

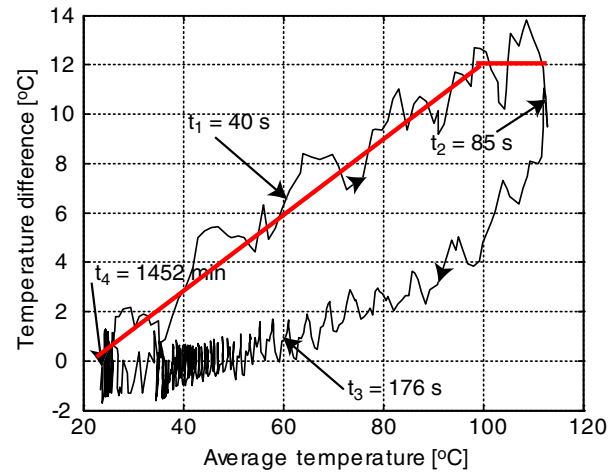
Specimen	Cycle	β_0	β_{90}
1	1	-7.442E-05	-8.334E-05
	2	-6.378E-05	-8.224E-05
	3	-6.910E-05	-9.868E-05
2	1	-8.098E-05	-8.992E-05
	2	-6.578E-05	-8.772E-05
	3	-7.086E-05	-9.868E-05
Average		-7.082E-05	-9.010E-05
Std. dev.		3.113E-06	3.610E-06
Variation [%]		8.79	8.02

90-direction strips, respectively.

Figure 6.10 shows the variation between the two surfaces of each specimen, as a function of the average temperature of the specimen. Note that the thermal gradient increased approximately linearly in both tests, and then remained approximately constant.



(a)



(b)

Figure 6.10: Measurements of temperature difference between two surfaces of (a) 0-direction strip and (b) 90-direction strip.

Chapter 7

Comparison of Experiments and Predictions

7.1 Stiffness Properties

Table 7.1 presents a comparison between the predicted stiffness coefficients, in Equations 3.38 and 3.41, and the values obtained from the tests. The rest of the section explains how the entries in the column of theoretical predictions have been computed, and discusses how they compare with the measurements.

Table 7.1: Predicted and measured stiffnesses

Property	Prediction	Measurement (average)
Extensional stiffness, S_x [N/mm]	2114	2178
Poisson's ratio, ν_{xy}	0.601	0.600
Shear stiffness, S_{xy} [N/mm]	660	777
Bending stiffness, D_x [Nmm]	1.945	2.077

7.1.1 Axial Stiffness

The predicted extensional stiffness, S_x , can be computed from

$$S_x = \frac{N_x}{\varepsilon_x} = \frac{1}{a_{11}} = \frac{1}{473 \times 10^{-6}} = 2114 \text{ N/mm} \quad (7.1)$$

The predicted Poisson's ratio can be derived from

$$\nu_{xy} = -\frac{a_{21}}{a_{11}} = \frac{284}{473} = 0.60 \quad (7.2)$$

In Table 7.1 note that the extensional stiffness and Poisson's ratio predictions practically coincide with the measured values. A graphical comparison of predicted and measured stiffnesses, where the measured values are plotted as average \pm standard deviation using the results in Table 6.1, is shown in Figure 7.1. The predicted stiffness falls within the lower and upper bound of the measured curve.

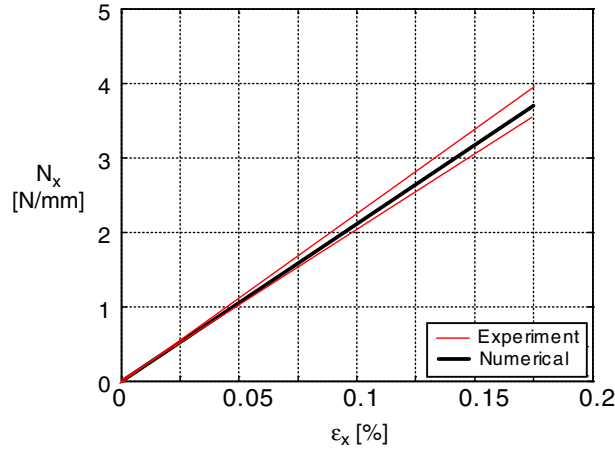


Figure 7.1: Comparison of tensile results.

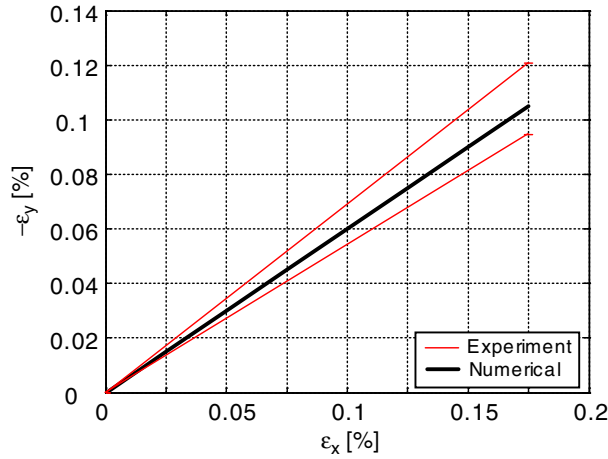


Figure 7.2: Comparison of Poisson's ratio results.

Figure 7.2 shows a similar comparisons for the Poisson's ratio, based on a plot from the initial force/width vs strain relation before the transition strain. Again, the predicted response falls within the range of the experimental results.

Finally, a comparison for the compression results is plotted in Figure 7.3. It shows again an excellent correlation.

7.1.2 Shear Stiffness

The predicted shear stiffness, S_{xy} , can be computed from

$$S_{xy} = \frac{N_{xy}}{\varepsilon_{xy}} = \frac{1}{a_{66}} = \frac{1}{1515 \times 10^{-6}} = 660 \text{ N/mm} \quad (7.3)$$

A graphical comparison of predicted and measured response in shear can be seen in Figure 7.4. The prediction appears to be an underestimation of the measured value. The most likely reason for the underestimate in the shear stiffness is that the beam model neglects the

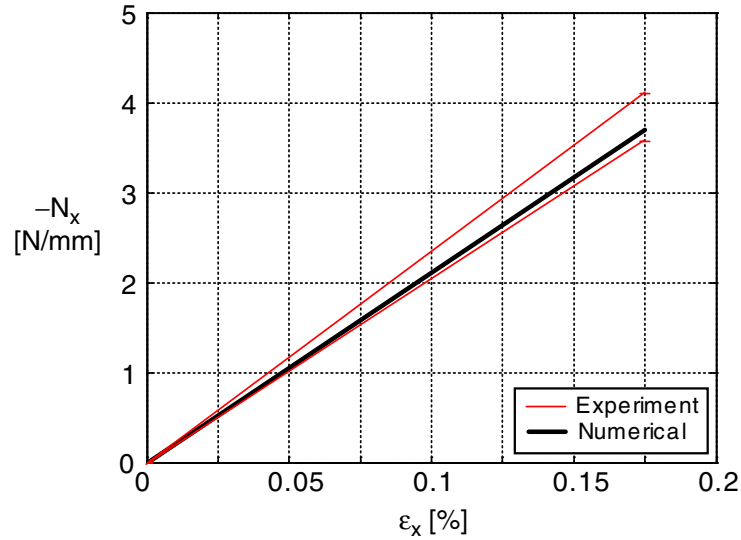


Figure 7.3: Comparison of compression results.

stiffness increase due to the relatively large size of the tow overlap regions, which are modelled as a single point in the beam model.

7.1.3 Bending Stiffness

The predicted bending stiffness, D_x , can be computed from

$$D_x = \frac{1}{d_{11}} = \frac{1}{514086 \times 10^{-6}} = 1.945 \text{ Nmm} \quad (7.4)$$

Figure 7.5 shows a graphical comparison of measured and predicted results. The prediction based on the periodic boundary conditions is a small underestimate of the measured value, as the mean bending stiffness is 7% smaller than the prediction.

The most likely reason for this underestimate is, again, that the stiffening provided by the tow overlap regions has not been captured in the model.

7.1.4 Alternative Estimates of ABD Matrix

Because of the uncertainties involved in estimating the cross-sectional properties of the tows forming the TWF composite, it is interesting to consider how the ABD matrix changes if different cross-sectional properties are assumed.

If we assume that the tows have a smaller cross-sectional area, based on Equation 2.13, we obtain $A_t = 0.0588 \text{ mm}^2$, $V_f = 0.65$. Hence, assuming the dimensions $0.754 \text{ mm} \times 0.078 \text{ mm}$

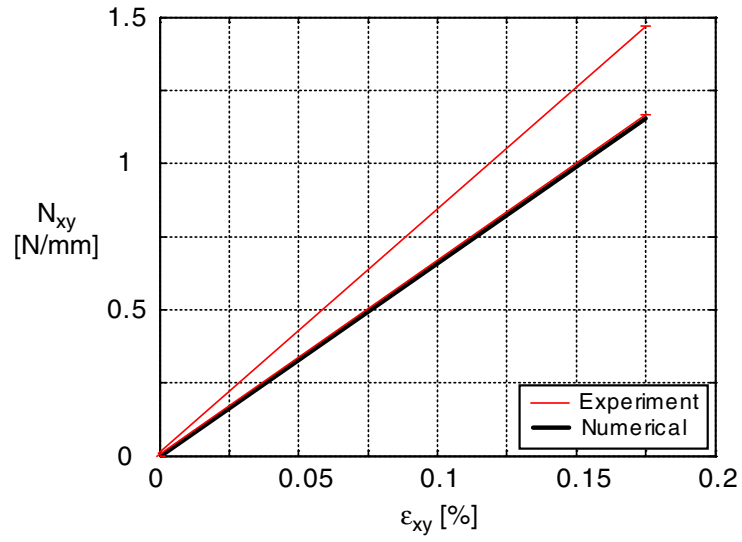


Figure 7.4: Comparison of shear results.

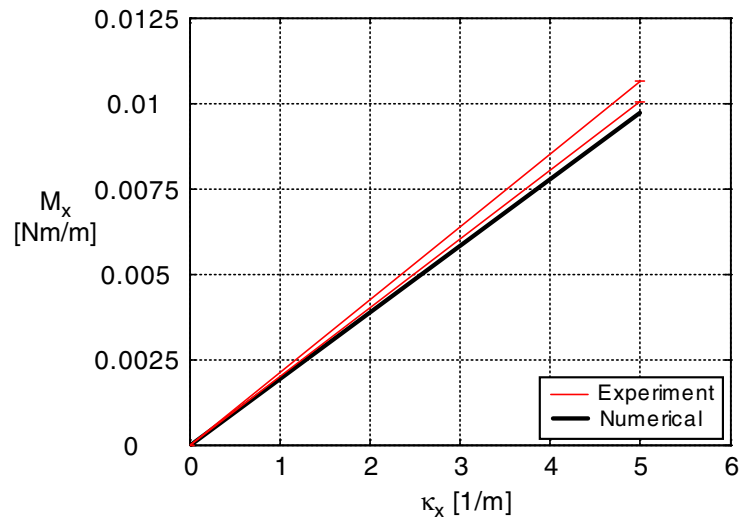


Figure 7.5: Comparison of bending results.

for the rectangular cross section of the tow, we find

$$\left\{ \begin{array}{c} N_x \\ N_y \\ N_{xy} \\ M_x \\ M_y \\ M_{xy} \end{array} \right\} = \left[\begin{array}{ccc|ccc} 3109 & 1870 & 0 & 0.00 & 0.00 & -0.57 \\ 1870 & 3110 & 0 & 0.00 & 0.00 & 0.57 \\ 0 & 0 & 620 & 0.57 & -0.57 & 0.00 \\ \hline 0.00 & 0.00 & 0.57 & 1.98 & 0.55 & 0.00 \\ 0.00 & 0.00 & -0.57 & 0.55 & 1.98 & 0.00 \\ -0.57 & 0.57 & 0.00 & 0.00 & 0.00 & 0.71 \end{array} \right] \left\{ \begin{array}{c} \varepsilon_x \\ \varepsilon_y \\ \varepsilon_{xy} \\ \kappa_x \\ \kappa_y \\ \kappa_{xy} \end{array} \right\} \quad (7.5)$$

The comparison of predictions and experimental results is then made in Table 7.2.

Table 7.2: Predicted (Equation 7.5) and measured results

Property	Prediction	Measurement (average)
Extensional stiffness, S_x [N/mm]	1983	2178
Poisson's ratio, ν_{xy}	0.602	0.600
Shear stiffness, S_{xy} [N/mm]	619	777
Bending stiffness, D_x [Nmm]	1.826	2.077

If, instead, we consider only the weight measurement set 2, the cross-sectional area of the tows is $A_t = 0.0539 \text{ mm}^2$ and hence the fibre volume fraction is $V_f = 0.71$. Hence, assuming that the cross section of the tows is rectangular, with dimensions $0.691 \text{ mm} \times 0.078 \text{ mm}$, the ABD matrix becomes

$$\left\{ \begin{array}{c} N_x \\ N_y \\ N_{xy} \\ M_x \\ M_y \\ M_{xy} \end{array} \right\} = \left[\begin{array}{ccc|ccc} 3105 & 1867 & 0 & 0.00 & 0.00 & -0.56 \\ 1867 & 3105 & 0 & 0.00 & 0.00 & 0.56 \\ 0 & 0 & 619 & 0.56 & -0.56 & 0.00 \\ \hline 0.00 & 0.00 & 0.56 & 1.98 & 0.55 & 0.00 \\ 0.00 & 0.00 & -0.56 & 0.55 & 1.98 & 0.00 \\ -0.56 & 0.56 & 0.00 & 0.00 & 0.00 & 0.71 \end{array} \right] \left\{ \begin{array}{c} \varepsilon_x \\ \varepsilon_y \\ \varepsilon_{xy} \\ \kappa_x \\ \kappa_y \\ \kappa_{xy} \end{array} \right\} \quad (7.6)$$

The comparison of predictions and experimental results of this case is shown in Table 7.3.

Comparing Equations 7.5 and 7.6, or Tables 7.2 and 7.3 it becomes clear that the ABD matrix is practically unchanged.

Table 7.3: Predicted (Equation 7.6) and measured results

Property	Prediction	Measurement (average)
Extensional stiffness, S_x [N/mm]	1981	2178
Poisson's ratio, ν_{xy}	0.602	0.600
Shear stiffness, S_{xy} [N/mm]	618	777
Bending stiffness, D_x [Nmm]	1.826	2.077

7.2 Strength Properties

7.2.1 Tensile Strength

A simple estimate of the tensile strength of TWF can be obtained by multiplying the tensile stiffness by the failure strain of the fibres, given in Table 2.1. Hence,

$$S_x \times \varepsilon_x = 2114 \times 0.015 = 31.7 \text{ N/mm} \quad (7.7)$$

This value is a 20% overestimate of the average measured value of 25.85 N/m, in Table 6.1.

7.2.2 Compressive Strength

The measured compressive strength of one-ply TWF can be predicted from the measured shear modulus. According to Budiansky and Fleck (1993), the dominant mechanism of compressive failure in polymer-matrix composites is plastic microbuckling. Hence, the compressive strength is controlled by fibre misalignment together with plastic shear deformation of the matrix. Their compressive strength can be estimated from

$$\sigma_C = \frac{\tau_y}{\gamma_y + \bar{\phi}} = \frac{G}{1 + \bar{\phi}/\gamma_y} \quad (7.8)$$

where τ_y is the yield strength of the composite in shear, γ_y is the corresponding yield strain ($\gamma_y = \tau_y/G$), and $\bar{\phi}$ is the maximum initial misalignment angle of the fibres. This approach was followed for single-ply plain-weave composites by Yee and Pellegrino (2007).

Equation 7.8 can be used to estimate the compressive strength of a cured tow, as follows. Figure 2.6 shows a micrograph of a one-ply specimen from which an initial fibre misalignment angle of 0.122 rad was measured. We substitute this value into Equation 7.8, together with the shear modulus $G_{12} = 4403 \text{ N/mm}^2$, from Table 2.6. The shear strength has not been measured in the present study. We will use the value $\tau_y = 70 \text{ N/mm}^2$ measured by Yee and Pellegrino (2007); hence $\gamma_y = \tau_y/G = 0.016$ and the compressive strength is $\sigma_C = 509 \text{ MN/mm}^2$.

The corresponding value for the strength of TWF is obtained by multiplying σ_C by the thickness of the tow and by 1/3, because about one third of the TWF consists of tows in one of the three weave directions. This calculation gives a compressive strength of 13.2 N/mm. This value is 70% higher than the average of the measured values, $N_{x,c}^u = 7.64 \text{ N/mm}$.

7.2.3 Shear Strength

No detailed attempt at predicting the shear strength will be made, as this is more difficult to predict than the compressive strength. Our prediction for the compressive strength in Section 7.2.2 is already of limited accuracy.

We will only note that a simple stress transformation argument would lead to the conclusion that failure in shear occurs by micro-buckling of the tow in compression, which would be expected to occur at a shear stress of $2N_{x,c}^u/\sqrt{3} = 8.8$ N/mm. This value is 76% higher than the average of the measurements.

7.2.4 Minimum Bend Radius

R_{min} can be estimated by considering the kinematic relationship between curvature and strain in a tow, based on standard beam theory. Hence

$$R_{min} = \frac{t}{2\varepsilon_{max}} \quad (7.9)$$

Substituting the tow thickness for t and the fibre failure strain for ε_{max} , from Table 2.1 gives,

$$R_{min} = \frac{0.078}{2 \times 0.015} = 2.60 \text{ mm} \quad (7.10)$$

which practically coincides with the average measured value, in Table 6.5.

7.3 Thermo-Mechanical properties

7.3.1 CTE

The solid-element finite element model described in Section 4.4 was used to predict the CTE for the 0-direction strip. The strip, shown in Figure 4.6, was fully constrained at a single node and was subjected to a uniform temperature increment of 100°C. The CTE in the 0-direction was then computed from the mid-plane strains in the tow direction obtained from this analysis. The resulting value is $2.44 \times 10^{-6} \text{ }^\circ\text{C}^{-1}$.

Two simple analytical estimates of the CTE were obtained earlier, one from Equation 2.25 and the other from Equation 4.7, which gave $\alpha_1 = 0.16 \times 10^{-6}/^\circ\text{C}$ and $\bar{\alpha}_c = 2.20 \times 10^{-6}/^\circ\text{C}$. The smaller prediction was obtained by considering a single tow, by itself; the larger prediction was obtained by considering the increase in CTE resulting from the transverse thermal expansion of the cross tows. Note that $\bar{\alpha}_c$ is about 10% smaller than the prediction from the solid-element finite element model.

The average measured CTE, see Table 6.6, was $0.957 \times 10^{-6} \text{ }^\circ\text{C}^{-1}$. This is about 2.3 times smaller than $\bar{\alpha}_c$ or the prediction from the solid-element finite element model, which one would expect to have fully captured the deformation of the tow cross-over regions, and almost six times bigger than the single tow prediction. A possible explanation for the actual value being intermediate between the two sets of predictions is that the stiffness of the cross tows has been overestimated, due to the bond area being smaller than assumed and/or the variation of the cross-sectional stiffness. However, it is believed that the main reason for the actual CTE being

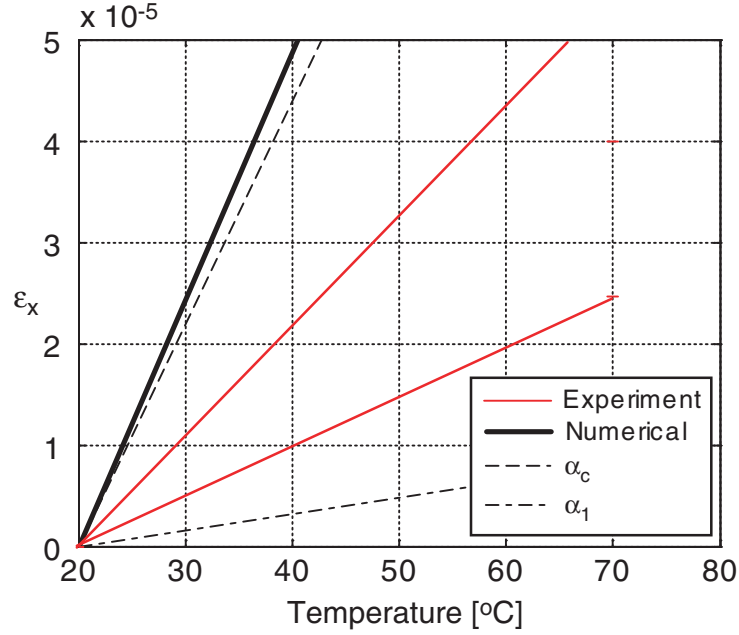


Figure 7.6: Comparison of CTE experimental and numerical result

lower than $\bar{\alpha}_c$ is that the resin content in the specimen was actually lower than assumed in the analysis, and so the value of the transverse CTE of the tows is smaller.

Figure 7.6 shows a comparison of the measured CTE's, including the observed variation in the measured values, with the two sets of analytical predictions and also the finite-element prediction.

7.3.2 CTT

The solid-element finite element model considered here is a strip consisting of multiple unit cells, arranged either in the 0-direction or the 90-direction. The two 0- and 90-direction models are shown in Figure 7.7. There are 16 hexagon units and 10 unit cells in the models, respectively. The details of the model are the same as in Section 4.3. Note that, due to the geometry of the weave, the length of two models is slightly different, but in each case the length matches that of the experimental samples in Section 6.6. Also note that at the end of each strip there are two virtual nodes defined, by defining a straight line that passes through two mid-plane nodes on the edge of the model. These nodes are at a distance of 9.1 mm, to match the distance between the points whose deflections were measured in the CTT test, Section 5.7.

Figure 7.8 defines the coordinate systems used for the analysis of the two strips, and the direction in which the tip points of edges 1 and 2 of each strip have to move in the case of a positive twisting curvature.

The mechanical boundary conditions are the same for the two strips; all nodes at one end of the strip are fixed against translation in all three directions.

A uniform temperature increment from 20°C to 90°C is applied, together with a through-thickness temperature gradient of up to 10°C. These temperature changes are imposed by di-

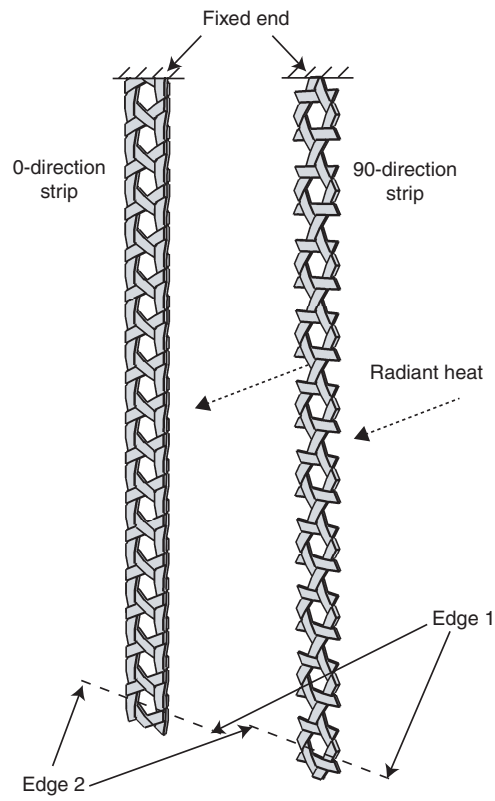


Figure 7.7: 0- and 90-direction strip models.

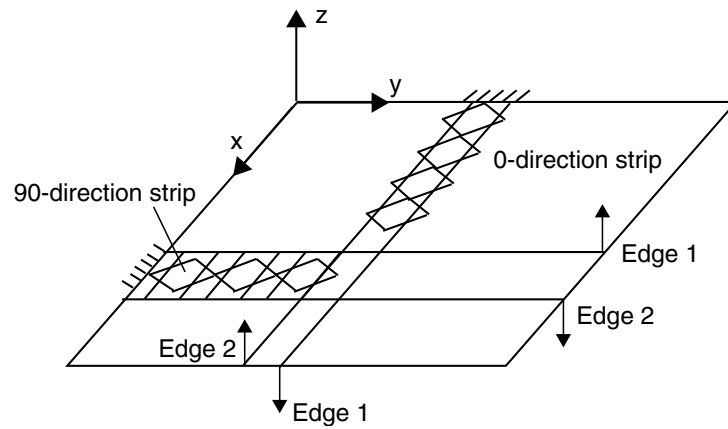


Figure 7.8: Displacements of end points of 0-direction and 90-direction strips, due to a positive twisting curvature.

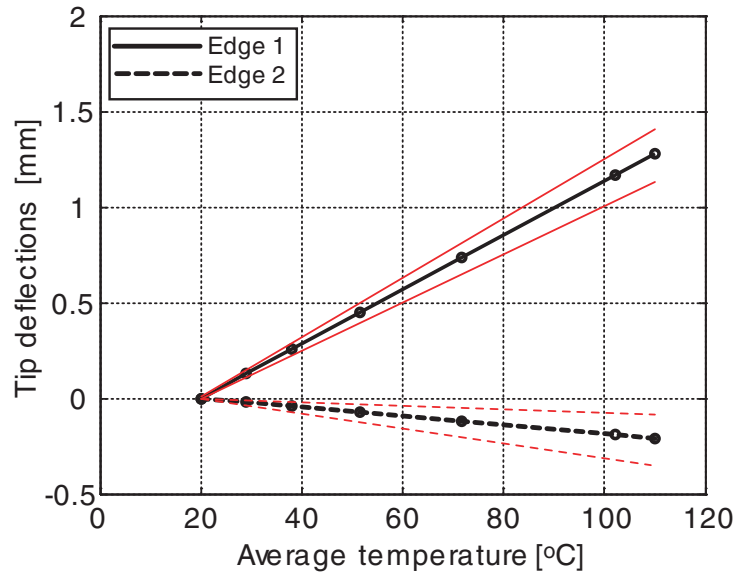


Figure 7.9: Comparison between prediction and experimental range (plotted in red) of edge deflections of 0-direction strip.

viding the thickness of the strip into three regions of equal thickness; the temperature of the centre region varies from 20°C to 90°C, that of the bottom region from 20°C to 85°C and that of the top region from 20°C to 95°C. The analysis is linear elastic in all cases.

The coefficient of thermal twist, β , can be determined from Equation 6.7. The values for the 0- and 90-direction strips are $-7.168 \times 10^{-5}/\text{mm}^\circ\text{C}$ and $-8.128 \times 10^{-5} /\text{mm}^\circ\text{C}$, respectively.

A comparison between the range of experimental measurements and the predictions, for each type of strip, is presented in Figures 7.9-7.10. In the first case, the finite-element results fall well within the experimental range; in the second case it appears that the effects of the thermal gradient have been exaggerated, and hence too much bending has been predicted, however the amount of twist predicted is predicted accurately.

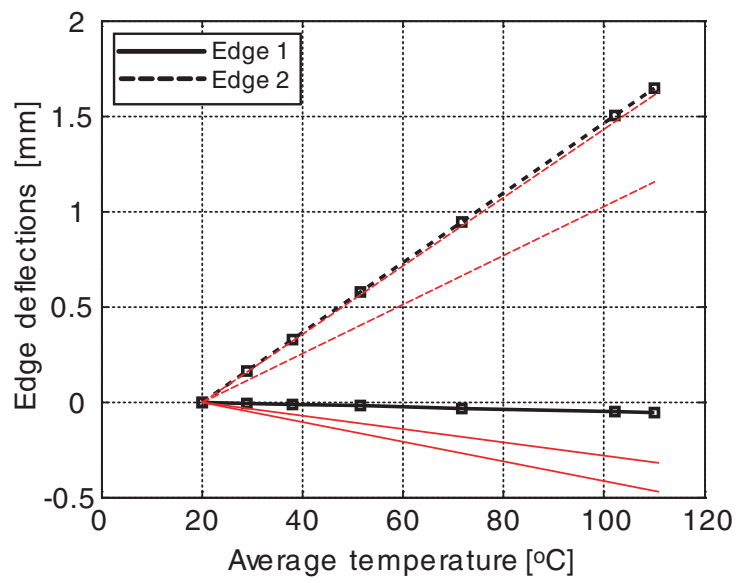


Figure 7.10: Comparison between prediction and experimental range (plotted in red) of edge deflections of 90-direction strip.

Chapter 8

Conclusion

It has been shown in this report that single-ply TWF composites should be modelled in terms of a grillage of wavy beams with uniform, rectangular cross-section, representing the cured tows of the composite. Two key geometrical properties of the tows are needed; first, their cross-sectional area, which can be estimated from the dry weight of the fabric, the resin film weight, and the density of the fibres and resin; second, their thickness, which is most accurately measured from a series of micrographs of the tows. These are the only two parameters that are needed, in addition to standard material properties for the fibres and the resin, which are provided on standard data sheets.

The stiffness of single-ply TWF composites is best described by the ABD matrix for a homogenized plate. This matrix has been derived from a unit cell consisting of “wavy 3-dimensional beams” using periodic boundary conditions.

The thermal deformation of single-ply TWF composites is described by two parameters, the linear coefficient of thermal expansion and the coefficient of thermal twist. The former can be readily estimated analytically; the latter has been estimated very accurately using a solid finite-element model. It seems possible that periodic boundary conditions and/or beam models might be used to simplify this calculation.

Detailed tests have been carried out to verify the accuracy of all the models presented in this report.

Acknowledgments

We thank John Ellis (Hexcel Composites, UK) and Ryoji Sakai (Sakase Adtech, Japan) for providing materials and material data. The CTE tests presented in Section 5.6 and Section 6.5 were conducted by Dr Leri Datashvili in the Institute for Lightweight Structures at TU Munich; we are grateful to the Head of the Institute, Professor Horst Baier for allowing us to use his facility. Helpful comments from Professor C.R. Calladine and Dr Vikram Deshpande at key stages of this research are gratefully acknowledged.

Bibliography

ABAQUS (2001), Inc. *ABAQUS Theory and Standard User's Manual Version 6.4*, Pawtucket, RI, USA.

Adobe Systems (2001) Adobe Illustrator 10. San Jose, California, USA.

Aoki, T. and K. Yoshida (2006), Mechanical and thermal behaviors of triaxially-woven carbon/epoxy fabric composite. 47th AIAA/ASME/ASCE/AHS/ASC Structures, Structural Dynamics and Materials Conference, 1-4 May 2006, Newport, RI, AIAA.

Autodesk, Inc. (2002), Autocad R15.6. San Rafael, California, USA.

ASTM (1986), *Standard Test Method for Flexural Properties of Unreinforced and Reinforced Plastics and Electrical Insulating Materials*, D790M-86, United States.

ASTM (2001), *Standard Test Method for In-Plane Shear Properties of Polymer Matrix Composite Materials by the Rail Shear Method*, D4255/D4255M-01, United States.

ASTM (2000), *Standard Test Method for Tensile Properties of Polymer Matrix Composite Materials*, D 3039/D 3039M-00, United States.

Bowles, D.E. (1990), Micromechanics analysis of space simulated thermal deformations and stresses in continuous fiber reinforced composites. NASA Technical Memorandum 102633.

Budiansky, B., and Fleck, N.A. (1993), Compressive failure of fibre composites. *Journal of Mechanics and Physics of Solids*, **41**, 183-221.

Daniel, I.M., and Ishai, O. (2006), *Engineering Mechanics of Composite Materials*, second edition, Oxford University Press.

Fleck, N.A. and Sridhar, I. (2002), End compression of sandwich columns. *Composites: Part A* **33** 353-359.

Hexcel Composites. Cambridge, United Kingdom.

Karkainen, R. L. and B. Sankar (2006), A direct micromechanics methods for analysis of failure initiation of plain weave textile composites, *Composites Science and Technology*, **66**, 137-150.

Kueh, A.B.H. and Pellegrino, S. (2006), Thermo-elastic behaviour of single ply triaxial woven fabric composites. 47th AIAA/ASME/ASCE/AHS/ASC Structures, Structural Dynamics and Materials Conference, 1-4 May 2006, Newport, RI, AIAA-2006-1899.

- Kueh, A.B.H., Soykasap, O., and Pellegrino, S. (2005), Thermo-mechanical behaviour of single-ply triaxial weave carbon fibre reinforced plastic. European Conference on Spacecraft Structures, Materials and Testing, 9-13 May 2005, ESA Estec.
- Matlab. The MathWorks Ltd.
- Quek, S.C., Waas, A.M., Shahwan, K., and Agaram, V. (2003), Analysis of 2D triaxial flat braided textile composites, *International Journal of Mechanical Sciences*, **45** 1077-1096.
- Sakase-Adtech Co. Ltd. Fukui, Japan.
- Soykasap, O., (2006), Micromechanical models for bending behaviour of woven composites, *Journal of Spacecraft and Rockets*, **43**, 1093-1100.
- Tang, X. and J. D. Whitcomb (2003), General techniques for exploiting periodicity and symmetries in micromechanics analysis of textile composites." *Journal of Composite Materials*, **37**, 1167-1189.
- Toray Industries, Inc. Tokyo, Japan.
- Tsai, S.W. and Hahn, H.T. (1980), *Introduction to composite materials*, Technomic.
- Torayca. Technical Data Sheet No. CFA-001, T300 Data Sheet.
- Yee, J.C.H., and Pellegrino, S. (2005), Folding of woven composite structures. *Composites: Part A*, **36**, 273-278.
- Zhao, Q. and Hoa, S.V. (2003), Thermal deformation behavior of triaxial woven fabric (TWF) composites with open holes, *Journal of Composite Materials*, **37**(18), 1629-1649.

ABAQUS PBC command file

```
*****  
*  
* Equation definition  
*  
*****  
*Equation  
3  
Q1, 1, 1, S1, 1, -1, TranQS1, 1, -3.12  
*Equation  
3  
Q1, 2, 1, S1, 2, -1, TranQS1, 2, -3.12  
*Equation  
3  
Q1, 3, 1, S1, 3, -1, TranQS1, 3, 4.21512  
*Equation  
3  
Q1, 4, 1, S1, 4, -1, RotQS1, 1, 3.12  
*Equation  
3  
Q1, 5, 1, S1, 5, -1, RotQS1, 2, -3.12  
*Equation  
3  
Q1, 6, 1, S1, 6, -1, RotQS1, 3, 0  
*****  
*Equation  
3  
Q2, 1, 1, S2, 1, -1, TranQS2, 1, -3.12  
*Equation  
3  
Q2, 2, 1, S2, 2, -1, TranQS2, 2, -3.12  
*Equation  
3  
Q2, 3, 1, S2, 3, -1, TranQS2, 3, 8.43024
```

*Equation

3

Q2, 4, 1, S2, 4, -1, RotQS2, 1, 3.12

*Equation

3

Q2, 5, 1, S2, 5, -1, RotQS2, 2, -3.12

*Equation

3

Q2, 6, 1, S2, 6, -1, RotQS2, 3, 0

*Equation

3

Q3, 1, 1, S3, 1, -1, TranQS3, 1, -3.12

*Equation

3

Q3, 2, 1, S3, 2, -1, TranQS3, 2, -3.12

*Equation

3

Q3, 3, 1, S3, 3, -1, TranQS3, 3, 12.64536

*Equation

3

Q3, 4, 1, S3, 4, -1, RotQS3, 1, 3.12

*Equation

3

Q3, 5, 1, S3, 5, -1, RotQS3, 2, -3.12

*Equation

3

Q3, 6, 1, S3, 6, -1, RotQS3, 3, 0

*Equation

3

R, 1, 1, P, 1, -1, TranRP, 1, -5.404

*Equation

3

R, 2, 1, P, 2, -1, TranRP, 2, -5.404

*Equation

3

R, 3, 1, P, 3, -1, TranRP, 3, 8.43024

*Equation

3

R, 4, 1, P, 4, -1, RotRP, 1, 5.404

*Equation

3

R, 5, 1, P, 5, -1, RotRP, 2, -5.404

*Equation

3

R, 6, 1, P, 6, -1, RotRP, 3, 0

***** *Case A* *****

*BOUNDARY

TranQS1, 1, 1, 1

TranQS1, 2, 3, 0

TranQS2, 1, 1, 1

TranQS2, 2, 3, 0

TranQS3, 1, 1, 1

TranQS3, 2, 3, 0

RotQS1, 1, 3, 0

RotQS2, 1, 3, 0

RotQS3, 1, 3, 0

TranRP, 1, 3, 0

RotRP, 1, 3, 0

***** *Case B* *****

*BOUNDARY

TranQS1, 1, 3, 0

TranQS2, 1, 3, 0

TranQS3, 1, 3, 0

RotQS1, 1, 3, 0

RotQS2, 1, 3, 0

RotQS3, 1, 3, 0

TranRP, 1, 1, 0

TranRP, 2, 2, 1

TranRP, 3, 3, 0

RotRP, 1, 3, 0

***** *Case C* *****

*BOUNDARY

TranQS1, 1, 1, 0

TranQS1, 2, 2, 0.5

TranQS1, 3, 3, 0

TranQS2, 1, 1, 0

TranQS2, 2, 2, 0.5

TranQS2, 3, 3, 0

TranQS3, 1, 1, 0

TranQS3, 2, 2, 0.5

TranQS3, 3, 3, 0
RotQS1, 1, 3, 0
RotQS2, 1, 3, 0
RotQS3, 1, 3, 0
TranRP, 1, 1, 0.5
TranRP, 2, 3, 0
RotRP, 1, 3, 0

***** *Case D* *****

*BOUNDARY

TranQS1, 1, 3, 0
TranQS2, 1, 3, 0
TranQS3, 1, 3, 0
RotQS1, 1, 1, 0
RotQS1, 2, 2, 1
RotQS1, 3, 3, 0
RotQS2, 1, 1, 0
RotQS2, 2, 2, 1
RotQS2, 3, 3, 0
RotQS3, 1, 1, 0
RotQS3, 2, 2, 1
RotQS3, 3, 3, 0
TranRP, 1, 3, 0
RotRP, 1, 3, 0

***** *Case E* *****

*BOUNDARY

TranQS1, 1, 3, 0
TranQS2, 1, 3, 0
TranQS3, 1, 3, 0
RotQS1, 1, 3, 0
RotQS2, 1, 3, 0
RotQS3, 1, 3, 0
TranRP, 1, 3, 0
RotRP, 1, 1, 1
RotRP, 2, 3, 0

***** *Case F* *****

*BOUNDARY

TranQS1, 1, 2, 0
TranQS1, 3, 3, 0.5
TranQS2, 1, 2, 0
TranQS2, 3, 3, 0.5
TranQS3, 1, 2, 0
TranQS3, 3, 3, 0.5

RotQS1, 1, 1, 0.5
RotQS1, 2, 3, 0
RotQS2, 1, 1, 0.5
RotQS2, 2, 3, 0
RotQS3, 1, 1, 0.5
RotQS3, 2, 3, 0
TranRP, 1, 2, 0
TranRP, 3, 3, 0.5
RotRP, 1, 1, 0
RotRP, 2, 2, 0.5
RotRP, 3, 3, 0

Matrices U and F

$$\mathbf{U} = \begin{bmatrix}
 -1.11 & 0.00 & -1.62 & -0.01 & 0.01 & 0.02 \\
 -0.97 & -3.00 & 0.00 & -0.01 & 0.01 & -0.03 \\
 -2.13 & 1.46 & -4.19 & 0.49 & -2.69 & 2.61 \\
 0.00 & 0.00 & 0.00 & 0.00 & 2.70 & -0.78 \\
 0.00 & 0.00 & 0.00 & 0.00 & 0.00 & 0.00 \\
 0.00 & 0.00 & -0.08 & 0.02 & -0.02 & 0.00 \\
 0.45 & 0.00 & -0.94 & -0.02 & 0.01 & 0.02 \\
 -1.00 & -1.62 & 0.78 & -0.01 & 0.01 & -0.04 \\
 -2.13 & 1.46 & 2.88 & -0.72 & 0.05 & 0.51 \\
 0.00 & 0.00 & 0.00 & 0.00 & 1.35 & -1.56 \\
 -7.18 & 7.11 & 0.00 & 1.56 & 0.00 & 0.68 \\
 0.00 & 0.00 & 0.10 & -0.01 & 0.01 & 0.00 \\
 0.45 & 0.00 & -0.27 & -0.01 & 0.01 & 0.02 \\
 -0.97 & -0.29 & 0.78 & -0.01 & 0.01 & -0.03 \\
 -2.13 & 1.46 & -4.19 & -0.72 & 0.97 & -1.60 \\
 0.00 & 0.00 & 0.00 & 0.00 & 0.00 & -1.56 \\
 0.00 & 0.00 & 0.00 & 1.56 & 0.00 & 1.35 \\
 0.00 & 0.00 & -0.08 & 0.02 & -0.02 & 0.00 \\
 0.45 & 0.00 & 0.41 & 0.01 & 0.01 & 0.02 \\
 -0.95 & 1.03 & 0.78 & -0.01 & 0.01 & -0.01 \\
 -2.13 & 1.46 & 2.88 & -0.72 & 0.05 & -3.71 \\
 0.00 & 0.00 & 0.00 & 0.00 & -1.35 & -1.56 \\
 7.18 & -7.11 & 0.00 & 1.56 & 0.00 & 2.03 \\
 0.00 & 0.00 & 0.10 & -0.01 & 0.01 & 0.00 \\
 -1.11 & 0.00 & 1.08 & -0.01 & 0.01 & 0.02 \\
 -0.97 & 2.41 & 0.00 & -0.01 & 0.01 & -0.03 \\
 -2.13 & 1.46 & -4.19 & 0.49 & -2.69 & -1.60 \\
 0.00 & 0.00 & 0.00 & 0.00 & -2.70 & -0.78 \\
 0.00 & 0.00 & 0.00 & 0.00 & 0.00 & 2.70 \\
 0.00 & 0.00 & -0.08 & 0.02 & -0.02 & 0.00 \\
 -2.67 & 0.00 & -0.94 & -0.02 & 0.01 & 0.02 \\
 -1.00 & -1.62 & -0.78 & -0.01 & 0.01 & -0.04 \\
 -2.13 & 1.46 & 2.88 & -0.72 & 0.05 & 2.61 \\
 0.00 & 0.00 & 0.00 & 0.00 & 1.35 & 0.00 \\
 -7.18 & 7.11 & 0.00 & -1.56 & 0.00 & 0.68 \\
 0.00 & 0.00 & 0.10 & -0.01 & 0.01 & 0.00 \\
 -2.67 & 0.00 & -0.27 & -0.01 & 0.01 & 0.02 \\
 -0.97 & -0.29 & -0.78 & -0.01 & 0.01 & -0.03 \\
 -2.13 & 1.46 & -4.19 & -0.72 & 0.97 & 2.61 \\
 0.00 & 0.00 & 0.00 & 0.00 & 0.00 & 0.00 \\
 0.00 & 0.00 & 0.00 & -1.56 & 0.00 & 1.35 \\
 0.00 & 0.00 & -0.08 & 0.02 & -0.02 & 0.00 \\
 -2.67 & 0.00 & 0.41 & 0.01 & 0.01 & 0.02 \\
 -0.95 & 1.03 & -0.78 & -0.01 & 0.01 & -0.01 \\
 -2.13 & 1.46 & 2.88 & -0.72 & 0.05 & 2.61 \\
 0.00 & 0.00 & 0.00 & 0.00 & -1.35 & 0.00 \\
 7.18 & -7.11 & 0.00 & -1.56 & 0.00 & 2.03 \\
 0.00 & 0.00 & 0.10 & -0.01 & 0.01 & 0.00
 \end{bmatrix}$$

$$\mathbf{F} = \begin{bmatrix}
 0.00 & 0.00 & -2060.88 & -1.93 & 1.93 & 0.00 \\
 -6211.88 & -10333.64 & 0.00 & 0.00 & 0.00 & -1.93 \\
 0.00 & 0.00 & 0.00 & 0.00 & 0.00 & 0.00 \\
 0.00 & 0.00 & -1.93 & 1.83 & 6.58 & 0.00 \\
 -183.92 & -187.82 & 0.00 & 0.00 & 0.00 & -2.38 \\
 0.00 & 0.00 & 0.00 & 0.00 & 0.00 & 0.00 \\
 7057.05 & 2495.51 & 0.00 & 0.00 & 0.00 & 0.00 \\
 0.00 & 0.00 & 98.88 & 2.22 & -2.22 & 0.00 \\
 -238.19 & -238.19 & 0.00 & 0.00 & 0.00 & 0.00 \\
 2.22 & -2.22 & 0.00 & 0.00 & 0.00 & -0.32 \\
 0.00 & 0.00 & 0.00 & 4.86 & 0.00 & 0.00 \\
 0.00 & 0.00 & 0.00 & 0.00 & 0.00 & 0.00 \\
 3784.29 & 5768.27 & 0.00 & 0.00 & 0.00 & -3.34 \\
 0.00 & 0.01 & 3371.79 & -1.11 & 1.11 & 0.00 \\
 0.00 & 0.00 & 0.00 & 0.00 & 0.00 & 0.00 \\
 -323.08 & -320.83 & 0.00 & 0.00 & 0.00 & -3.48 \\
 0.00 & 0.00 & 3.34 & 1.69 & 3.17 & 0.00 \\
 0.00 & 0.00 & 0.00 & 0.00 & 0.00 & 0.00 \\
 7057.05 & 2495.51 & 0.00 & 0.00 & 0.00 & 0.00 \\
 0.00 & 0.00 & 98.88 & 2.22 & -2.22 & 0.00 \\
 238.27 & 238.27 & 0.00 & 0.00 & 0.00 & 0.00 \\
 2.22 & -2.22 & 0.00 & 0.00 & 0.00 & -0.32 \\
 0.00 & 0.00 & 0.00 & 4.86 & 0.00 & 0.00 \\
 0.00 & 0.00 & 0.00 & 0.00 & 0.00 & 0.00 \\
 0.00 & 0.00 & 2060.88 & 1.93 & -1.93 & 0.00 \\
 6211.88 & 10333.64 & 0.00 & 0.00 & 0.00 & 1.93 \\
 0.00 & 0.00 & 0.00 & 0.00 & 0.00 & 0.00 \\
 0.00 & 0.00 & 1.93 & -1.83 & -6.58 & 0.00 \\
 183.92 & 187.82 & 0.00 & 0.00 & 0.00 & 2.38 \\
 0.00 & 0.00 & 0.00 & 0.00 & 0.00 & 0.00 \\
 -7057.05 & -2495.51 & 0.00 & 0.00 & 0.00 & 0.00 \\
 0.00 & 0.00 & -98.88 & -2.22 & 2.22 & 0.00 \\
 238.19 & 238.19 & 0.00 & 0.00 & 0.00 & 0.00 \\
 -2.22 & 2.22 & 0.00 & 0.00 & 0.00 & 0.32 \\
 0.00 & 0.00 & 0.00 & -4.86 & 0.00 & 0.00 \\
 0.00 & 0.00 & 0.00 & 0.00 & 0.00 & 0.00 \\
 -3784.29 & -5768.27 & 0.00 & 0.00 & 0.00 & 3.34 \\
 0.00 & -0.01 & -3371.79 & 1.11 & -1.11 & 0.00 \\
 0.00 & 0.00 & 0.00 & 0.00 & 0.00 & 0.00 \\
 323.08 & 320.83 & 0.00 & 0.00 & 0.00 & 3.48 \\
 0.00 & 0.00 & -3.34 & -1.69 & -3.17 & 0.00 \\
 0.00 & 0.00 & 0.00 & 0.00 & 0.00 & 0.00 \\
 -7057.05 & -2495.51 & 0.00 & 0.00 & 0.00 & 0.00 \\
 0.00 & 0.00 & -98.88 & -2.22 & 2.22 & 0.00 \\
 -238.27 & -238.27 & 0.00 & 0.00 & 0.00 & 0.00 \\
 -2.22 & 2.22 & 0.00 & 0.00 & 0.00 & 0.32 \\
 0.00 & 0.00 & 0.00 & -4.86 & 0.00 & 0.00 \\
 0.00 & 0.00 & 0.00 & 0.00 & 0.00 & 0.00
 \end{bmatrix}$$